

**THE UNIVERSITY OF CALGARY**

**Submillimetre Observations of Circumstellar Dust**

**BY**

**Carolyne R. Marshall**

**A THESIS**

**SUBMITTED TO THE FACULTY OF GRADUATE STUDIES  
IN PARTIAL FULFILLMENT OF THE REQUIREMENTS FOR THE  
DEGREE OF MASTER OF SCIENCE**

**DEPARTMENT OF PHYSICS**

**CALGARY, ALBERTA**

**May, 1989**

**© Carolyne R. Marshall 1989**



National Library  
of Canada

Bibliothèque nationale  
du Canada

Canadian Theses Service    Service des thèses canadiennes

Ottawa, Canada  
K1A 0N4

The author has granted an irrevocable non-exclusive licence allowing the National Library of Canada to reproduce, loan, distribute or sell copies of his/her thesis by any means and in any form or format, making this thesis available to interested persons.

L'auteur a accordé une licence irrévocable et non exclusive permettant à la Bibliothèque nationale du Canada de reproduire, prêter, distribuer ou vendre des copies de sa thèse de quelque manière et sous quelque forme que ce soit pour mettre des exemplaires de cette thèse à la disposition des personnes intéressées.

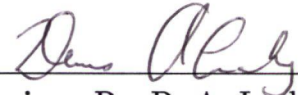
The author retains ownership of the copyright in his/her thesis. Neither the thesis nor substantial extracts from it may be printed or otherwise reproduced without his/her permission.

L'auteur conserve la propriété du droit d'auteur qui protège sa thèse. Ni la thèse ni des extraits substantiels de celle-ci ne doivent être imprimés ou autrement reproduits sans son autorisation.

ISBN 0-315-54285-3

**THE UNIVERSITY OF CALGARY**  
**FACULTY OF GRADUATE STUDIES**

The undersigned certify that they have read, and recommend to the Faculty of Graduate Studies for acceptance, a thesis entitled, "Submillimetre Observations of Circumstellar Dust" submitted by Carolyn R. Marshall in partial fulfillment of the requirements for the degree of Master of Science.



---

Supervisor, Dr. D. A. Leahy  
Department of Physics  
University of Calgary



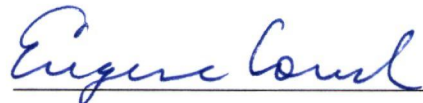
---

Dr. S. Kwok  
Department of Physics  
University of Calgary



---

Dr. R. Chatterjee  
Department of Physics  
University of Calgary



---

Dr. W. E. Couch  
Department of Mathematics and  
Statistics  
University of Calgary

Date May 19/89

## Abstract

This thesis concerns itself with furthering our knowledge of circumstellar shells around late-type stars. The *circumstellar dust shell or envelope* defines the region around the star which is outside the star's atmosphere, but where the matter is still identified with the star. Dust shells appear around stars of all spectral types that have high enough mass-loss rates. This thesis considers the circumstellar envelopes of late-type oxygen-rich stars and carbon stars. A carbon star is defined as a late-type star in which the abundance of carbon in the photosphere is greater than the abundance of oxygen.

Observations made with the James Clerk Maxwell Telescope (JCMT) in Hawaii provided data for IK Tau, TX Cam,  $\alpha$  Ori, VY CMa, CW Leo, RW LMi, and W Hya in the 450, 800, and 1100 $\mu$ m wavebands. These observations represent first submillimetre observations of stars from a ground-based telescope which made possible a better determination of the energy distribution of late-type stars in this previously unexplored part of the electromagnetic spectrum. The *IRAS* Point Source Catalogue (PSC) and Low-Resolution Spectra Catalogue (LRSC) are used to supplement the JCMT submillimetre observations. Observations were made of the objects M82 and Hb 12, but only upper limits were determined. Spectral plots of previous observations and the JCMT submillimetre observations of these objects are presented.

A computer modeling code provided by C.M. Leung (1976) and later modified by Volk (1986) is used along with Volk's silicate dust opacity function, and the silicon carbide dust opacity function provided by Chan (1988), to fit the observa-

tions. Physical parameters on the dust properties and the mass loss rates of the stars are derived. Results of the models compared to the data seem to indicate an opacity wavelength dependence of approximately  $\lambda^{-1.5}$  for some M-type stars, though this wavelength dependence is not followed by all M-type stars. The results for the carbon star CW Leo indicates an opacity function wavelength dependence of  $\lambda^{-1}$ ; no conclusion can be drawn for the carbon star RW LMi.

## Acknowledgements

I would like to thank my supervisors, Dr. S. Kwok and Dr. D.A. Leahy, for their support and guidance throughout this project. I would also like to thank Dr. Leahy for the financial support I received during part of the time this thesis was being done.

I would like to acknowledge the help of Goeran Sandell of the James Clerk Maxwell Telescope (JCMT) for his help in making the submillimetre observations, as well as the rest of the staff of the JCMT for helping make my brief stay there as productive as possible.

Thanks are due to Josephine Chan and Dr. Kevin Volk for helping me to make some sense of the dust modeling code. I would also like to express my thanks to Dr. Tony Lui of the Johns Hopkins University Applied Physics Laboratory for helping me to realize my dreams through his kindness and generous advice. Thanks also should be extended to Steve Griffiths for his time in generating a schematic diagram of the JCMT for me.

Finally, I am deeply grateful to my family for their continued emotional support. I am also grateful to my fiancé Jim Murtha for his help in using  $\text{\LaTeX}$ .

# Dedication

To my father,  
who knows what it means to face a challenge.

# Contents

<b>Abstract</b>	<b>iii</b>
<b>Acknowledgements</b>	<b>v</b>
<b>Dedication</b>	<b>vi</b>
<b>1 Introduction</b>	<b>1</b>
1.1 Review of Asymptotic Giant Branch Evolution . . . . .	1
1.2 Spectral and Luminosity Classifications . . . . .	6
1.3 Variable Stars . . . . .	8
1.3.1 Pulsating Intrinsic Variables . . . . .	10
<b>2 Circumstellar Dust Envelopes</b>	<b>13</b>
2.1 Dust Grains . . . . .	13
2.1.1 Extinction - Dust Opacity and Mie Theory . . . . .	13
2.1.2 Two Types of Grains in Consideration . . . . .	15
2.2 The Circumstellar Dust Shell . . . . .	24
2.3 Radiative Transfer Model . . . . .	26
2.3.1 General Description of Modeling Code . . . . .	26
2.3.2 Review of the Method of Solution of the Radiative Transfer Equations . . . . .	27
2.3.3 Overview of the Modified Code . . . . .	31
<b>3 Submillimetre and IRAS Observations</b>	<b>33</b>
3.1 IRAS . . . . .	33
3.1.1 Point Source Catalogue Overview . . . . .	34
3.1.2 Low Resolution Spectra Catalogue Overview . . . . .	34
3.2 JCMT . . . . .	36
3.2.1 Technical Specifications . . . . .	36
3.2.2 Observing Procedures . . . . .	40
3.2.3 Data Reduction . . . . .	42
3.3 Criteria for Source Selection . . . . .	57
<b>4 Data Analysis and Modeling</b>	<b>59</b>
4.1 Star Descriptions . . . . .	59
4.1.1 M-Type Stars . . . . .	62
4.1.2 Carbon Stars . . . . .	64



4.1.3	Other Objects . . . . .	66
4.2	Spectral Data . . . . .	67
4.2.1	<i>IRAS</i> Observations . . . . .	67
4.2.2	Submillimeter Observations . . . . .	69
4.2.3	Cross-Referenced Observations . . . . .	73
4.3	Expectations for the Circumstellar Dust Envelope in the Submil- limetre Range . . . . .	80
4.4	Fitting Procedures - Model Parameters and Results . . . . .	86
4.5	Observational Spectra Plots of Other Objects . . . . .	100
<b>5</b>	<b>Discussion and Conclusions</b>	<b>103</b>
5.1	M-Type Stars . . . . .	104
5.2	Carbon Stars . . . . .	106
5.3	Suggestions for Future Work . . . . .	111
5.3.1	Modifications to the Opacity Functions . . . . .	111
	<b>Bibliography</b>	<b>113</b>

## List of Tables

1.1	Characteristics of Spectral Classes. . . . .	7
1.2	Luminosity Classes. . . . .	7
1.3	Special Features or Additional Details of the Spectra. . . . .	9
2.1	The Derived Relative Silicate Opacity Function . . . . .	18
2.1	The Derived Relative Silicate Opacity Function (cont'd) . . . . .	19
2.2	The Derived Silicon Carbide Relative Opacity Function . . . . .	22
2.2	The Derived Silicon Carbide Relative Opacity Function (cont'd) . . . . .	23
3.1	Beamwidths for Filters. . . . .	40
3.2	Flux Conversion Factors. . . . .	51
3.3	Individual Scan Results for IK Tau. . . . .	52
3.4	Individual Scan Results for TX Cam. . . . .	52
3.5	Individual Scan Results for $\alpha$ Ori. . . . .	53
3.6	Individual Scan Results for VY CMa. . . . .	53
3.7	Individual Scan Results for CW Leo. . . . .	54
3.8	Individual Scan Results for RW LMi. . . . .	55
3.9	Individual Scan Results for W Hya. . . . .	55
3.10	Individual Scan Results for M82. . . . .	57
3.11	Individual Scan Results for Hb 12. . . . .	57
4.1	Characteristics of Observed Objects. . . . .	60
4.2	Object Associations. . . . .	61
4.3	IRAS Flux Densities and LRS Classification . . . . .	68
4.4	Calibrated Submillimetre Flux Densities. . . . .	70
4.5	The Statistical and Systematic Errors. . . . .	72
4.6	Magnitude Observations. . . . .	74
4.7	Magnitude Observations . . . . .	75
4.8	UBVRI Observations for $\alpha$ Ori. . . . .	76
4.9	GCVS Observations. . . . .	76
4.10	CW Leo Observations. . . . .	77
4.11	TX Cam Observations. . . . .	77
4.12	$\alpha$ Ori Observations. . . . .	78
4.13	VY CMa Observations. . . . .	78
4.14	Hb 12 Observations. . . . .	78
4.15	M82 Observations. . . . .	79
4.16	Expected Versus Observed Submillimetre Fluxes. . . . .	85
4.17	Model Results for the Oxygen-Rich Stars. . . . .	91

4.18 Model Results for the Carbon Stars. . . . . 97

## List of Figures

1.1	The Hertzsprung-Russel Diagram . . . . .	2
1.2	The Evolutionary Track of a Low Mass Star . . . . .	3
1.3	The Positions of Variables in the HR Diagram . . . . .	11
2.1	The Silicate Opacity Function . . . . .	17
2.2	The Silicon Carbide Relative Opacity Function . . . . .	21
3.1	The JCMT Cassegrain Reflector (Schematic) . . . . .	38
3.2	Chart Recorder Traces for 3C84 at 450, 800 and 1100 $\mu m$ . . . . .	45
3.3	Chart Recorder Traces for Jupiter at 450, 800, and 1100 $\mu m$ . . . . .	46
3.4	Chart Recorder Traces for CW Leo at 450, 800 and 1100 $\mu m$ . . . . .	47
3.5	Chart Recorder Traces for VY CMa at 450,800, and 1100 $\mu m$ . . . . .	48
3.6	Chart Recorder Traces for RW LMi at 800 and 1100 $\mu m$ . . . . .	49
3.7	Chart Recorder Traces for $\alpha$ Ori at 800 and 1100 $\mu m$ . . . . .	50
4.1	Dust Temperature Dependence on Shell Radius for Silicate Dust . . . . .	88
4.2	Dust Temperature Dependence on Shell Radius for SiC Dust . . . . .	89
4.3	The Model Fit for $\alpha$ Ori . . . . .	92
4.4	The Model Fit for VY CMa . . . . .	93
4.5	The Model Fit for IK Tau . . . . .	94
4.6	The Model Fit for TX Cam . . . . .	95
4.7	The Model Fit for W Hya . . . . .	96
4.8	The Model Fit for CW Leo . . . . .	98
4.9	The Model Fit for RW LMi . . . . .	99
4.10	The Plot of M82 Observational Data . . . . .	101
4.11	The Plot of Hb 12 Observational Data . . . . .	102
5.1	Model Spectrum and Black Body Spectrum . . . . .	105
5.2	Effects of Scattering Versus No Scattering . . . . .	108
5.3	Fit to RW LMi with a Higher $\tau$ . . . . .	110

# Chapter 1

## Introduction

The most fundamental properties of the stars obtained by observations are luminosity (or absolute magnitude) and the effective temperature (or spectral type), (Kitchin, 1987). The Hertzsprung-Russel (HR) diagram (figure 1.1) plots objects with luminosity or absolute magnitude on the ordinate ( $y$ -axis) and effective temperature or spectral class on the abscissa ( $x$ -axis). The HR diagram is one of the most useful ways of summarizing many of the properties of stellar objects. The evolutionary track of a low mass star from main sequence to white dwarf in the HR diagram is shown in figure 1.2, (Shu, 1982). Most of the objects of interest in this thesis are giants or supergiants and fall along the asymptotic giant branch (AGB) or the late asymptotic giant branch (LAGB).

### 1.1 Review of Asymptotic Giant Branch Evolution

As stars evolve up the asymptotic giant branch (AGB), they undergo increasing mass loss (Kwok and Volk, 1988). As a star ascends the AGB, its luminosity and radius increase, and a steady decrease in photospheric (effective) temperature results, (Kwok, 1988). As the star evolves past spectral types of about M3, mass loss rates from its surface greatly increase, and dust begins to form around the star, (Kwok, 1988). This dust ejected in the mass loss process surrounds the star and begins to obscure its photosphere. In the early M-type stars this surrounding of dust

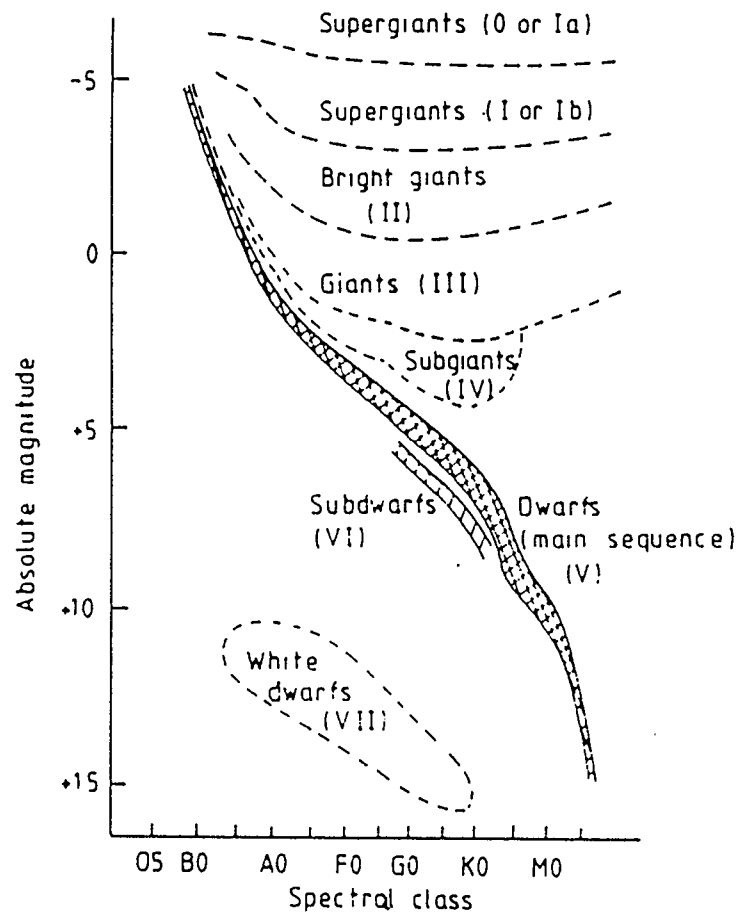


Figure 1.1: The Hertzsprung-Russel (HR) diagram, (Kitchin, 1987).

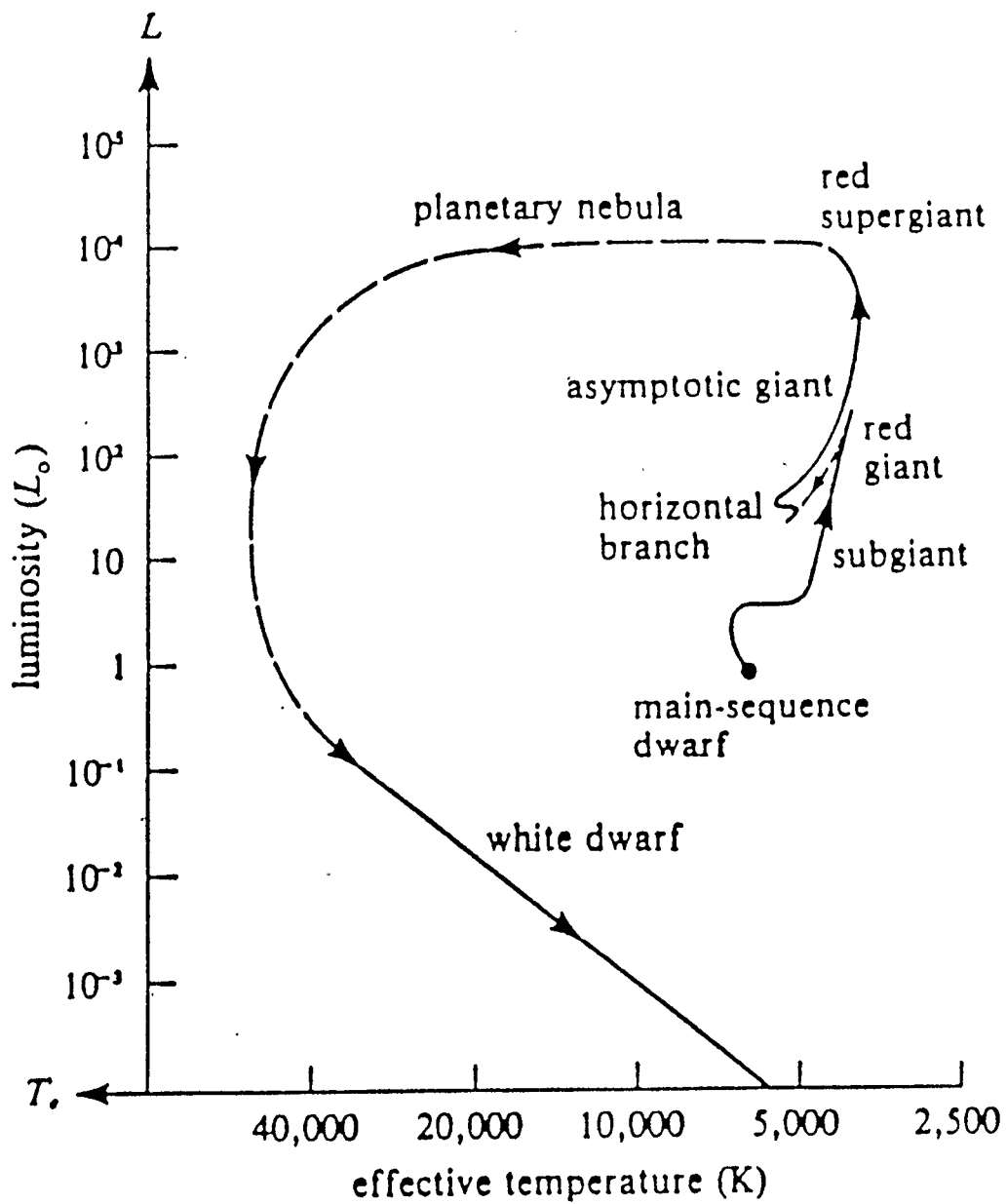


Figure 1.2: The evolutionary track of a low mass star from main sequence to white dwarf in the HR diagram, (Shu, 1982).

(the circumstellar envelope (CSE) or circumstellar dust shell (CDS)) is generally optically thin; by the time the star reaches the later spectral types (approximately M10) the circumstellar envelope is generally optically thick, (Kwok, 1988). Thus, the circumstellar envelope tends to increase in optical thickness with evolution along the asymptotic giant branch. The circumstellar dust absorbs the radiation from the photosphere and re-radiates it in the infrared (IR) and submillimetre (submm) wavebands.

Stellar evolution past the spectral type of approximately M10 is generally called the late asymptotic giant branch (LAGB) phase, (Kwok, 1987). Precise locations of the LAGB stars on the Hertzsprung-Russel diagram are difficult to determine due to uncertainties in both luminosity and effective temperature. These uncertainties are caused by the obscuring of the photosphere by the circumstellar envelope, (Kwok, 1987). At this point, features in the circumstellar envelope must be used to determine the state of evolution of the underlying star.

The dust in the circumstellar envelope is assumed to be heated by the central star, and the dust opacity ( $Q_{abs,\nu}$ ) is assumed to have a frequency dependence of  $\nu^\gamma$  (a wavelength dependence of  $\lambda^{-\gamma}$ ) in the longer wavelengths. The dust temperature distribution is expected to be  $T_D \propto r^{-\frac{2}{4+\gamma}}$ . The dust envelope is expected to be optically thin in the submillimetre wavelength range. For cool oxygen-rich stars, the circumstellar envelope shows an emission or absorption feature at approximately  $10\mu m$ . This feature is common to most oxygen-rich giants with spectral types later than approximately M3 (Kwok, 1987) and is considered a defining characteristic of such stars. The emission and absorption features due to silicate grains were discovered in 1969 by N. Woolf and E. Ney; subsequently silicate grains were considered to



be the cause of the feature found in the oxygen-rich giants. As such, it is assumed that silicate particles should be the first particle to condense around oxygen-rich stars, (Gilman, 1969). Observations of Mira variables and infrared stars in the IRC and AFGL sky surveys indicate that the common silicate feature ranges from emission to deep absorption (Kwok, 1987). For carbon-rich stars, there is a common infrared signature at  $11.3\mu m$ . This was identified by Treffers and Cohen (1974) as being due to silicon carbide (SiC) grains, as seen by the  $11.3\mu m$  SiC feature. The first particles to condense around carbon stars should be silicon carbide and carbon, (Gilman, 1969). Mass loss rates for late-type stars are generally of the order of  $10^{-4}$  to  $10^{-8}M_{\odot} yr^{-1}$ , (Werner, 1985; Jura, 1988; Zuckerman, 1980) with outflow velocities of the order of  $\sim 10km s^{-1}$ , though there is a wide range from 5 to  $50km s^{-1}$  (Jura, 1988).

The purpose of this thesis is to extend the wavelength coverage of existing measurements of circumstellar envelopes in order to hopefully obtain a better understanding of the circumstellar dust and the structure of the dust envelopes. We want to better define the energy distribution of the circumstellar envelope emission between  $100\mu m$  and  $1mm$ . There has been little exploration into this area of the spectrum to this date. The submillimetre waveband is one of the few regions of the electromagnetic spectrum yet to be readily available to astronomers, due mainly to the attenuating nature of the Earth's atmosphere. Recently, observations have become possible from telescopes on high, dry mountain sites, or on board a high altitude airplane, such as the NASA Kuiper Airborne Observatory (KAO). The results presented in this thesis are among the first photometry results for the ground-based James Clerk Maxwell Telescope (JCMT), located on the 4200m summit of

Mauna Kea in Hawaii. The JCMT consists of a mounted Cassegrain reflector. It is one of the largest telescopes in the world capable of operating in the millimetre and submillimetre wavebands. There is currently an on-going investigation into the performance of the JCMT and its equipment; presented in this thesis is what is generally known to date.

For a circumstellar envelope assumed to be optically thin in the submillimetre range of the spectrum, a density profile of the form  $n_d(r) \propto r^{-n}$  is assumed, with  $n = 2$  for constant mass loss, and the predicted spectral shape is  $\lambda F_\lambda = \nu F_\nu \propto \nu^{\frac{2+\gamma}{2}+1+\frac{(n-2)(4+\gamma)}{2}}$ , where  $\gamma$  is the frequency dependence of the opacity function such that  $Q_\nu \propto \nu^\gamma$ . For a circumstellar envelope formed by constant mass loss,  $n = 2$  and the predicted spectral shape is  $\lambda F_\lambda \propto \lambda^{-\left(\frac{2+\gamma}{2}+1\right)}$ .

## 1.2 Spectral and Luminosity Classifications

The MKK spectral classification system was developed by Morgan, Keenan and Kelman. There are thirteen groups of spectra, labelled by the letters:

$$O B A F G K M - R N S W P Q.$$

The first seven of these form the major classes of stellar spectra, with O-type stars being the hottest and youngest, M-type stars being the coolest and oldest. Each of these seven is subdivided into ten subdivisions, and grouped according to the major characteristics of the spectrum, (table 1.1).

Apart from the spectral class, a luminosity parameter is added, separating the stars into various luminosity classes, (table 1.2). Classes O to M are sometimes subdivided by the use of lowercase letters, to further describe the star, (table 1.3).

Table 1.1: Characteristics of Spectral Classes.  
The characteristics of the spectral classes as noted by C.R. Kitchin (1987).

Spectral Class	Major Characteristics of the Spectrum
O4-B0	Few lines, most of those actually visible being from highly ionised Si, N, etc. H Balmer and ionised He lines visible.
B0-B5	Balmer lines strengthening, neutral He and lower stages of ionisation of Si, N, etc. now producing lines.
B5-A0	Neutral He lines disappear, H Balmer lines peak in intensity at A0, Ca II <i>K</i> line appears.
A0-F0	Balmer lines weakening, numerous lines due to singly-ionised metals appear.
F0-G0	Spectra becoming more complex, Balmer and ionised metal lines weakening, neutral metal lines strengthening.
G0-K0	Ca II <i>H</i> and <i>K</i> lines peak in their intensities, Balmer lines continue to weaken, neutral metal lines continue to increase in intensity.
K0-M0	Balmer lines still just visible, many lines due to neutral metals, a few TiO bands appear.
M0-M8	TiO bands dominate the spectrum.

Table 1.2: Luminosity Classes.  
(After C.R. Kitchin, 1987.)

Luminosity Class	Star Type
I	supergiants
II	bright giants
III	giants
IV	subgiants
V	main sequence
VI	subdwarfs
VII	white dwarfs

The spectra classes R and N are often combined into a single class C, designating carbon stars. This class is subdivided as well in order to represent major characteristics of the spectra, (C0 to C9). Often, there will be a second number, which designates the abundance parameter, (for example, RW LMi is classified as C4,3). The C spectra is characterized by strong bands of cyanogen (CN), molecular carbon, and other carbon compounds. Generally, the carbon to oxygen abundance ratio  $\frac{C}{O} > 1$  designates a carbon star. Many C-stars are variable - quite a few have the characteristics of Mira variables.

S-type stars are generally long period variables; spectral characteristics are most similar to those of N-type stars, though of lower temperatures. Their defining characteristics are the presence of strong ZrO bands in the spectra, and the absence or weak presence of TiO bands, (Kitchin, 1987). Class P are nebular spectra with spectra consisting almost entirely of emission lines. Class Q classify novae during their outbursts.

### 1.3 Variable Stars

Variable stars, or variables, change their luminosities by amounts from 0.01 to 20 stellar magnitudes, with time scales from seconds to decades. The most wide spread system of labelling variables is an extension of the Bayer system. The Bayer system labels brighter stars in each constellation with capital letters from A to Q. The extension to the Bayer system labels the variable stars in each constellation with capital letters starting at R for the brightest. As more and more variables are discovered in a constellation, the system extends to include double capital letters,

Table 1.3: Special Features or Additional Details of the Spectra.  
(Taken from C.R. Kitchin, 1987.)

<i>Prefix</i>	
c or sg	Very narrow spectrum lines; a supergiant; luminosity classes 0, I, Ia, Ib, etc.
g	Giant; luminosity class III.
d	Dwarf; main sequence; luminosity class V.
sd	Subdwarf; luminosity class VI.
w, wd or D	White dwarf; Luminosity class VII.
<i>Suffix</i>	
e	Emission lines present in the spectrum.
n	Very broad or nebulous lines.
s	Sharp lines (but less so than supergiants).
v	Variable spectrum.
p, pec	Peculiar spectrum. Some non-standard features to the main spectral class.
m	Metallic lines present when not expected or stronger than expected.
k	Interstellar absorption lines in the spectrum.
a, ab, b	Suffix to <i>luminosity</i> class: a, the brightest; b, the faintest subdivision.

(from RR to RZ, SS to SZ, TT to TZ, and so on up to ZZ, then AA to AZ, BB to BZ, etc). When all the available letter designations have been exhausted for the particular constellation (334 possible in all), the system resorts to the designation by the letter V (for variable) followed by a number starting from 335. Figure 1.3 shows the approximate positions of variable types in the Hertzsprung-Russel diagram.

Variables can be divided into two major groups: intrinsic and extrinsic variables. In extrinsic variables, the star's emission is constant, but the radiation received on Earth is altered by some external factor, as in eclipsing binaries. In intrinsic variables, the luminosity and emission of the star itself is changing. This thesis concerns itself mainly with intrinsic variables as classified by the IAU classes of variables, (Kitchin, 1987). Intrinsic variables are further divided into two major groups: pulsating and eruptive. We are concerned only with the pulsating variables.

### 1.3.1 Pulsating Intrinsic Variables

The three types of pulsating intrinsic variables of concern here are the Mira variables, the semi-regular variables, and the irregular variables. Mira variables are typically late-type giants with long periods of 100 to 1000 days. Usually denoted by the variable classification M, they typically have amplitudes of 2.5 stellar magnitudes or greater. Miras include both oxygen-rich and carbon-rich stars. Spectra are usually of type M, or C. Oxygen-rich M-type Miras have fairly regular periods, with their energy distribution peaking in the infrared, (Feast and Whitelock, 1987). Miras seem to have typical mass loss rates of approximately  $10^{-5} - 10^{-7} M_{\odot} yr^{-1}$ ,

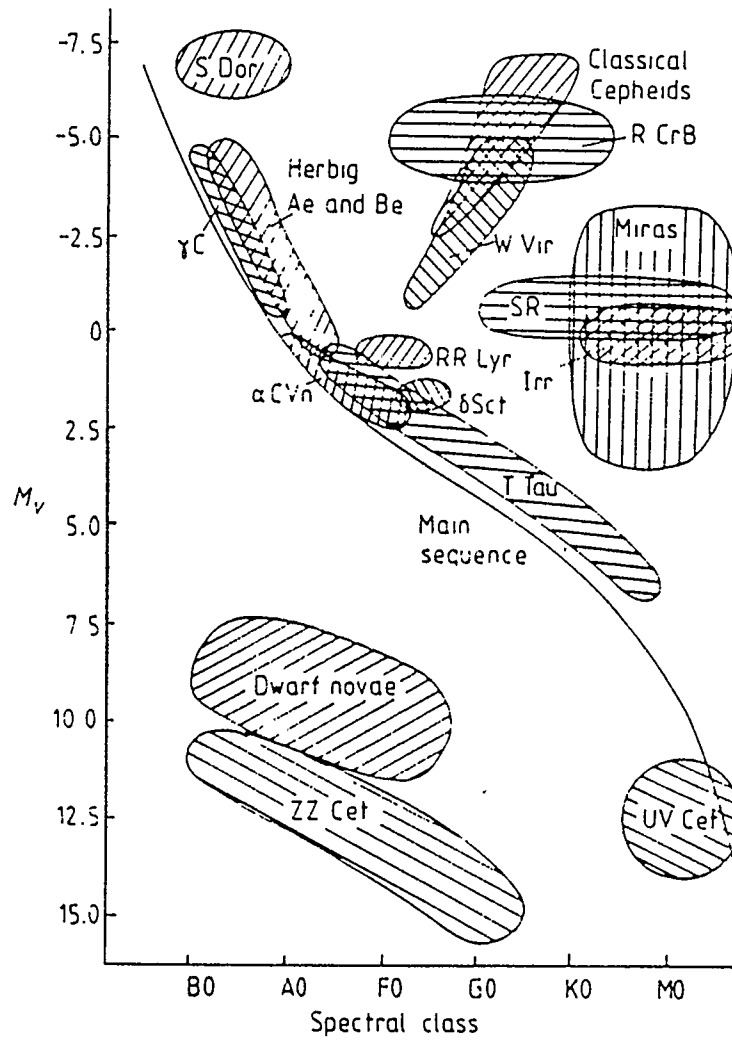


Figure 1.3: The positions of various variable types in the HR diagram, (Kitchin, 1987).

and outflow velocities of the order of approximately  $10 \text{ km s}^{-1}$ . All Mira stars have circumstellar envelopes, (de Jager, 1980).

Semi-regular variables are typically giants and supergiants. Usually they are of late-type spectral class and have unstable periods of approximately 20 to 2000 days. They are denoted by the variable classifications SR, SRa, SRb, SRc, SRd. Amplitudes for the semi-regulars are typically less than 2.0 stellar magnitudes.

Irregular variables are typically late-type giants with long characteristic time scales for their emission variations. They are denoted by the variable classifications L, Lb, Lc. They are characterized by slow wavelike variations in emission without well-pronounced periodicity.

In this thesis, we study a number of oxygen and carbon rich variable stars on the asymptotic giant branch which fall into the category of pulsating intrinsic variables. The thesis is divided into five chapters, where chapter 2 details the types of dust grains assumed, as well as discussing the dust shell theory and the envelope modeling code. Chapter 3 discusses the *IRAS* data base and the JCMT specifications as well as source criteria. Chapter 4 details the analysis of the data and gives results of the models. Chapter 5 discusses the results of the models, summarizing and concluding the thesis.



## Chapter 2

### Circumstellar Dust Envelopes

#### 2.1 Dust Grains

Dust grains present in a medium scatter and absorb radiation. The grains also will emit radiation at various wavelengths. Basic properties of dust grains which must be discussed are the *extinction* and *opacity*.

##### 2.1.1 Extinction - Dust Opacity and Mie Theory

Scattering and absorption remove energy from a beam of radiation travelling through the medium. This removal of energy from the beam of radiation *attenuates* the beam: the source of the radiation is effectively obscured. This attenuation, or obscuration, is called the *extinction*. Extinction is defined as the sum of absorption and scattering of radiation.

The scattering cross-section  $C_{sca}$  defines the energy of the incident beam falling on the area  $C_{sca}$ ; this energy is equal to the total energy removed from the beam by scattering in all directions, (Van de Hulst, 1957). The absorption cross-section  $C_{abs}$  similarly defines the energy removed from the incident beam by being absorbed inside the area  $C_{abs}$ . Following this reasoning, the total energy removed from the incident beam is then equal to the energy falling on the area  $C_{ext}$ , which is the total extinction cross-section. Since the cross-section is proportional to the energy, we then have, by the law of conservation of energy,  $C_{ext} = C_{sca} + C_{abs}$ . These

cross-sections are functions of the orientation of the particle and the polarization of the incident radiation. We are concerned here only with spherical particles, so that the orientation of the particle does not matter, nor does the polarization of the radiation - thus the cross-sections are independent of both for our purposes.

A spherical dust particle of radius  $a$  has a geometrical cross-section of  $\pi a^2$ . The efficiency factors for extinction, scattering, and absorption are defined as

$$\begin{aligned} Q_{ext} &= \frac{C_{ext}}{\pi a^2} \\ Q_{abs} &= \frac{C_{abs}}{\pi a^2} \\ Q_{sca} &= \frac{C_{sca}}{\pi a^2}. \end{aligned}$$

The efficiency factors are dimensionless quantities for which the relation  $Q_{ext} = Q_{abs} + Q_{sca}$  holds. The opacity  $\kappa$  is a function of the absorption efficiency factor  $Q_{abs}$ .

Mie formulae for the scattering properties of a sphere of radius  $a$  are determined in terms of the parameters  $x = \frac{2\pi a}{\lambda}$ , which is a dimensionless parameter, and  $m = n - in' = \sqrt{\Upsilon - \frac{2i\sigma\lambda}{c}}$ , (Wickramasinghe,1973), where  $\lambda \equiv$  wavelength,  $m \equiv$  complex refractive index,  $n \equiv$  refractive index of the medium,  $n' \equiv$  absorptive index of the medium,  $\Upsilon \equiv$  dielectric constant of the medium,  $\sigma \equiv$  conductivity of the medium. (Of course, the term medium refers to the grain material itself.) From Mie theory, one can determine the following quantities:  $C_{sca}, C_{abs}, \langle g \rangle, \Gamma$ . The asymmetry parameter  $\langle g \rangle$  is used in Leung's radiative transfer modeling code, (discussed in following sections of this chapter). The asymmetry parameter is defined as the forward directivity of the scattering by grains. Mathematically, it

is defined as

$$g \equiv \langle \cos \theta \rangle = \frac{\int_0^\pi S(\theta) \cos \theta \sin \theta d\theta}{\int_0^\pi S(\theta) \sin \theta d\theta}$$

so that

$$g = \begin{cases} 1 & \text{forward scattering} \\ 0 & \text{isotropic scattering} \\ -1 & \text{backward scattering, (Leung,1975)} \end{cases}$$

and  $S(\theta)$  is the fraction of radiation incident on a grain which is scattered into the unit solid angle in a direction which makes an angle  $\theta$  with the incident beam. Leung (1975) goes on further to define the effective asymmetry parameter  $\langle g \rangle_\nu$  as an integral function of the scattering cross-section for spherical grains  $\langle Q_{sca} \pi a^2 \rangle_\nu$ . The albedo  $\Gamma$  is defined as the ratio of the scattering efficiency to the extinction efficiency,  $\Gamma = \frac{Q_{sca}}{Q_{ext}}$ . Van de Hulst (1957) and Wickramasinghe (1972) go into detail about the Mie theory of scattering and absorption, and the reader is referred to these references for more information.

### 2.1.2 Two Types of Grains in Consideration

In modeling the spectra of the stars, only two types of dust grains were considered: (i) silicate ( $(\text{Mg, Fe})_2\text{SiO}_4$ ) for the oxygen-rich, M-type stars; and (ii) silicon carbide (SiC) for the carbon stars. Both these types of grains have condensation temperatures of approximately 1500K.

#### Silicate

The opacity function for silicate used in modelling the M-type stars was obtained from Volk (1986). This silicate opacity function was derived from the Low-Resolution Spectra (LRS) of oxygen stars. The well-known  $9.7\mu\text{m}$  silicate

feature can be seen in figure 2.1. This feature is seen in the circumstellar shells of oxygen-rich giants and supergiants. It has not been seen in the spectra of carbon stars. The parameters for this silicate dust, as obtained by Volk, are the molecular weight  $A \sim 140$  AMU, grain radius  $a = 0.1\mu m$ , cosmic abundance  $y \sim 4 \times 10^{-5}$  (which is the cosmic abundance of silicon), grain density  $\rho_d \sim 3.0g\ cm^{-3}$ . The parameter  $\frac{Q_{\lambda_0}}{a}$ , being the opacity at reference wavelength  $\lambda_0$  over grain radius  $a$ , has a value of  $\sim 1.3\mu m^{-1}$  at  $9.7\mu m$ . The relative opacity function is shown in table 2.1. The opacity is normalized to the peak of the  $10\mu m$  silicate feature at  $9.7\mu m$ . The original opacity function was arbitrarily set by Volk to have a  $\lambda^{-1}$  distribution out to  $84\mu m$ , and a  $\lambda^{-2}$  distribution thereafter. In subsequent modeling of our stars, we found that an opacity function with  $\lambda^{-1.5}$  distribution better represented the emergent spectrum, thus the necessary modifications were made to Volk's opacity function longward of  $84\mu m$ . Gilman (1969) found the condensation temperature of silicate grains to be approximately  $1500K$ .

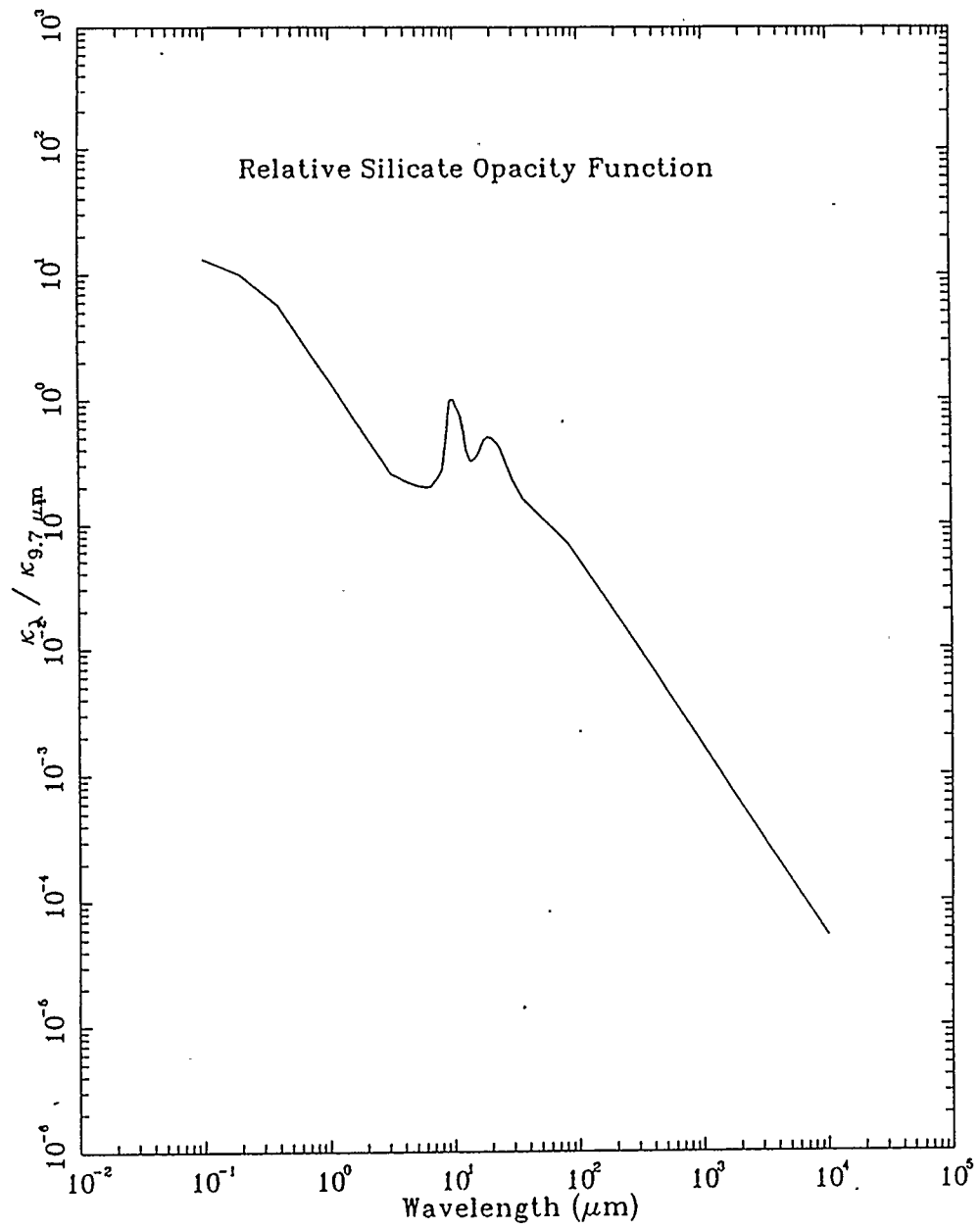


Figure 2.1: The silicate dust opacity function as derived from fits to LRSC data, (Volk,1986).

Table 2.1: The Derived Relative Silicate Opacity Function  
 The derived silicate opacity, normalized to  $9.7\mu m$ , (Volk, 1986). The opacity longward of  $84\mu m$  has a dependence of  $\lambda^{-1.5}$ .

Wavelength ( $\mu m$ )	Relative Opacity	Wavelength ( $\mu m$ )	Relative Opacity
10000	$5.2643 \times 10^{-5}$	21.5	$4.6688 \times 10^{-1}$
8500	$6.7164 \times 10^{-5}$	21.0	$4.7871 \times 10^{-1}$
7000	$8.9878 \times 10^{-5}$	20.5	$4.8746 \times 10^{-1}$
5500	$1.2900 \times 10^{-4}$	20.0	$4.9441 \times 10^{-1}$
4200	$1.9344 \times 10^{-4}$	19.5	$4.9698 \times 10^{-1}$
3100	$3.0495 \times 10^{-4}$	19.0	$4.9955 \times 10^{-1}$
2400	$4.4772 \times 10^{-4}$	18.5	$4.8952 \times 10^{-1}$
1800	$6.8926 \times 10^{-4}$	18.0	$4.7395 \times 10^{-1}$
1300	$1.1231 \times 10^{-3}$	17.5	$4.5402 \times 10^{-1}$
1000	$1.6643 \times 10^{-3}$	17.0	$4.2495 \times 10^{-1}$
850	$2.1235 \times 10^{-3}$	16.5	$3.8997 \times 10^{-1}$
700	$2.8424 \times 10^{-3}$	16.0	$3.6566 \times 10^{-1}$
550	$4.0810 \times 10^{-3}$	15.5	$3.4662 \times 10^{-1}$
420	$6.1158 \times 10^{-3}$	15.0	$3.3312 \times 10^{-1}$
310	$9.6437 \times 10^{-3}$	14.5	$3.2489 \times 10^{-1}$
240	$1.4161 \times 10^{-2}$	14.0	$3.2219 \times 10^{-1}$
180	$2.1801 \times 10^{-2}$	13.8	$3.2450 \times 10^{-1}$
130	$3.5511 \times 10^{-2}$	13.6	$3.3106 \times 10^{-1}$
100	$5.2643 \times 10^{-2}$	13.4	$3.4225 \times 10^{-1}$
84	$6.8373 \times 10^{-2}$	13.2	$3.5781 \times 10^{-1}$
68	$8.5466 \times 10^{-2}$	13.0	$3.7556 \times 10^{-1}$
52	$1.1176 \times 10^{-1}$	12.8	$4.0283 \times 10^{-1}$
36	$1.6257 \times 10^{-1}$	12.6	$4.4296 \times 10^{-1}$
30	$2.2585 \times 10^{-1}$	12.4	$4.9222 \times 10^{-1}$
27	$2.8913 \times 10^{-1}$	12.2	$5.5215 \times 10^{-1}$
24	$4.0141 \times 10^{-1}$	12.0	$5.9871 \times 10^{-1}$
23.5	$4.1312 \times 10^{-1}$	11.9	$6.2457 \times 10^{-1}$
23.0	$4.3357 \times 10^{-1}$	11.8	$6.5222 \times 10^{-1}$
22.5	$4.4373 \times 10^{-1}$	11.7	$6.8154 \times 10^{-1}$
22.0	$4.5543 \times 10^{-1}$	11.6	$7.0920 \times 10^{-1}$

Table 2.1: The Derived Relative Silicate Opacity Function (cont'd)  
 The derived silicate opacity, normalized to  $9.7\mu\text{m}$ , (Volk, 1986). The opacity longward of  $84\mu\text{m}$  has a dependence of  $\lambda^{-1.5}$ .

Wavelength ( $\mu\text{m}$ )	Relative Opacity	Wavelength ( $\mu\text{m}$ )	Relative Opacity
11.5	$7.3865 \times 10^{-1}$	8.5	$3.5215 \times 10^{-1}$
11.4	$7.5010 \times 10^{-1}$	8.4	$3.1923 \times 10^{-1}$
11.3	$7.6154 \times 10^{-1}$	8.3	$2.8913 \times 10^{-1}$
11.2	$7.9987 \times 10^{-1}$	8.2	$2.7048 \times 10^{-1}$
11.1	$8.0939 \times 10^{-1}$	8.1	$2.6765 \times 10^{-1}$
11.0	$8.1994 \times 10^{-1}$	8.0	$2.6135 \times 10^{-1}$
10.9	$8.3151 \times 10^{-1}$	7.6	$2.3923 \times 10^{-1}$
10.8	$8.4412 \times 10^{-1}$	7.2	$2.2212 \times 10^{-1}$
10.7	$8.5788 \times 10^{-1}$	6.8	$2.0489 \times 10^{-1}$
10.6	$8.7614 \times 10^{-1}$	6.4	$2.0090 \times 10^{-1}$
10.5	$8.9916 \times 10^{-1}$	6.0	$2.0000 \times 10^{-1}$
10.4	$9.2424 \times 10^{-1}$	5.6	$2.0116 \times 10^{-1}$
10.3	$9.5125 \times 10^{-1}$	5.2	$2.0437 \times 10^{-1}$
10.2	$9.8058 \times 10^{-1}$	4.8	$2.0990 \times 10^{-1}$
10.1	$9.8675 \times 10^{-1}$	4.4	$2.1762 \times 10^{-1}$
10.0	$9.9293 \times 10^{-1}$	4.0	$2.2752 \times 10^{-1}$
9.9	$9.9486 \times 10^{-1}$	3.6	$2.3974 \times 10^{-1}$
9.8	$9.9743 \times 10^{-1}$	3.2	$2.5402 \times 10^{-1}$
9.7	$1.0000 \times 10^0$	2.8	$3.1048 \times 10^{-1}$
9.6	$9.8495 \times 10^{-1}$	2.4	$3.9113 \times 10^{-1}$
9.5	$9.7003 \times 10^{-1}$	2.0	$5.1421 \times 10^{-1}$
9.4	$9.2000 \times 10^{-1}$	1.8	$6.0206 \times 10^{-1}$
9.3	$8.4000 \times 10^{-1}$	1.6	$7.1846 \times 10^{-1}$
9.2	$7.4006 \times 10^{-1}$	1.4	$8.7781 \times 10^{-1}$
9.1	$6.6006 \times 10^{-1}$	1.2	$1.1061 \times 10^0$
9.0	$5.8006 \times 10^{-1}$	1.0	$1.4534 \times 10^0$
8.9	$5.1537 \times 10^{-1}$	0.8	$2.0257 \times 10^0$
8.8	$4.6932 \times 10^{-1}$	0.6	$3.1280 \times 10^0$
8.7	$4.2701 \times 10^{-1}$	0.4	$5.7492 \times 10^0$
8.6	$3.8791 \times 10^{-1}$	0.2	$1.0000 \times 10^1$
		0.1	$1.3183 \times 10^1$

### Silicon Carbide

The opacity function for silicon carbide (SiC) used in modelling the carbon stars was obtained from Chan (1988). This SiC opacity function was derived from the Low-Resolution Spectra (LRS) of class 40 objects. The  $11.3\mu m$  feature can be seen in figure 2.2. This broad feature is seen in emission in circumstellar shells around carbon stars. The parameters for the silicon carbide dust, as taken from Chan, are the molecular weight  $A \sim 40$  AMU, the silicon cosmic abundance  $y \sim 4 \times 10^{-5}$ , the grain radius  $a = 0.1\mu m$ , the grain density  $\rho \sim 3 g cm^{-3}$ . The parameter  $\frac{Q_{\lambda_0}}{a}$  at the reference wavelength of  $11.3\mu m$  was chosen to be  $\sim 3.32\mu m^{-1}$  according to Chan,(1988), which she based on laboratory measurements of silicon carbide made by Borghesi *at al.* (1985). The calculated opacity function is shown in table 2.2. The opacity function has a wavelength dependence of roughly  $\lambda^{-1}$  out from  $10\mu m$ . The opacity function is normalized to the peak of the  $11\mu m$  feature. Silicon carbide grains can condense around  $1500K$ , (McCabe, 1982).



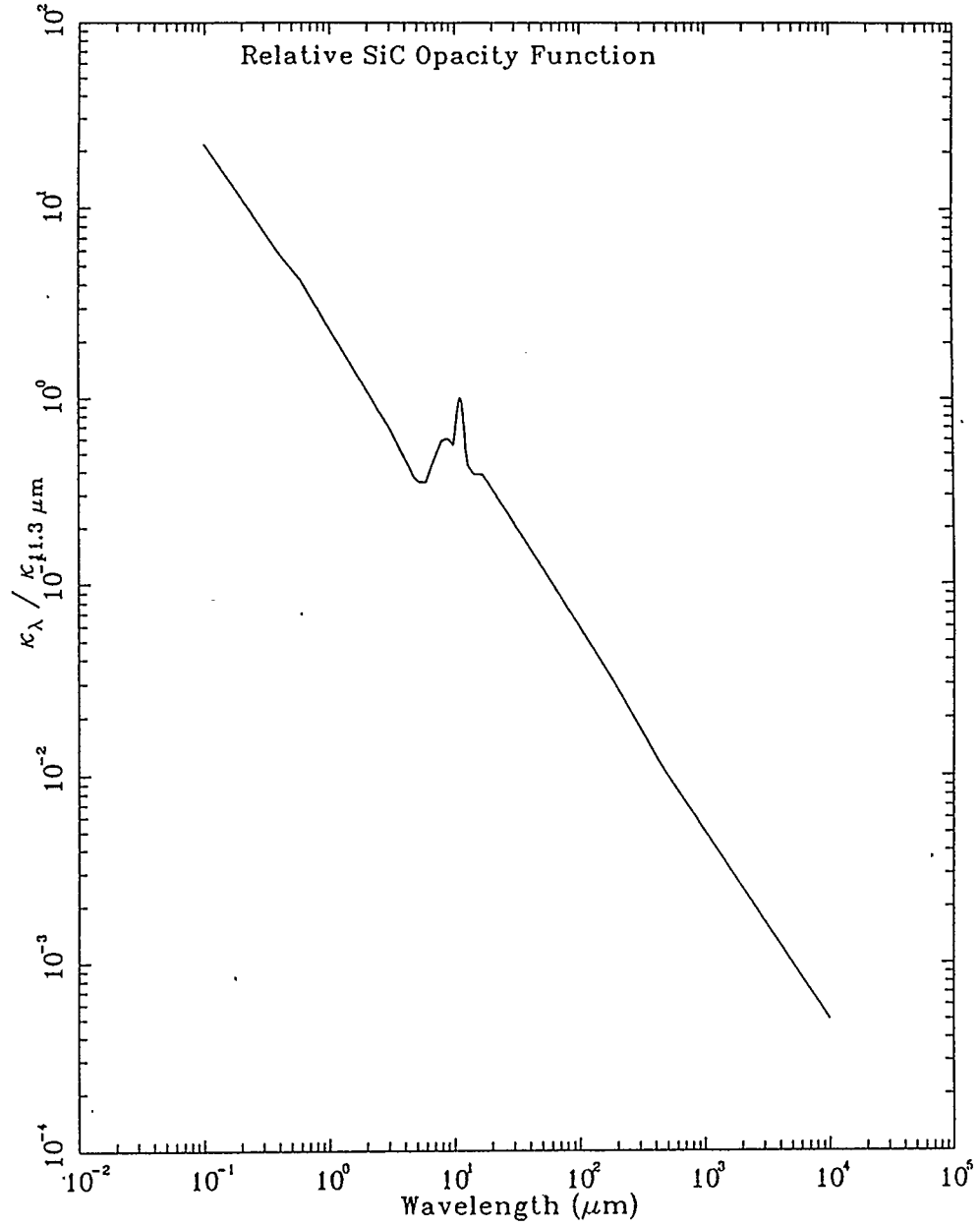


Figure 2.2: The silicon carbide relative opacity function as derived from fits to LRSC data, (Chan,1988).

Table 2.2: The Derived Silicon Carbide Relative Opacity Function  
 The SiC opacity for Sic dust, normalized to  $11.3\mu m$ , (Chan, 1988).

Wavelength ( $\mu m$ )	Relative Opacity	Wavelength ( $\mu m$ )	Relative Opacity
10000	$5.0032 \times 10^{-4}$	21.5	$2.9862 \times 10^{-1}$
8500	$5.8861 \times 10^{-4}$	21.0	$3.0614 \times 10^{-1}$
7000	$7.1481 \times 10^{-4}$	20.5	$3.1414 \times 10^{-1}$
5500	$9.0979 \times 10^{-4}$	20.0	$3.2230 \times 10^{-1}$
4200	$1.1913 \times 10^{-3}$	19.5	$3.3109 \times 10^{-1}$
3100	$1.6139 \times 10^{-3}$	19.0	$3.4037 \times 10^{-1}$
2400	$2.0841 \times 10^{-3}$	18.5	$3.4997 \times 10^{-1}$
1800	$2.7799 \times 10^{-3}$	18.0	$3.6037 \times 10^{-1}$
1300	$3.8484 \times 10^{-3}$	17.5	$3.7124 \times 10^{-1}$
1000	$5.0032 \times 10^{-3}$	17.0	$3.8276 \times 10^{-1}$
850	$5.8861 \times 10^{-3}$	16.5	$3.8292 \times 10^{-1}$
700	$7.1481 \times 10^{-3}$	16.0	$3.8292 \times 10^{-1}$
550	$9.0979 \times 10^{-3}$	15.5	$3.8308 \times 10^{-1}$
420	$1.1811 \times 10^{-2}$	15.0	$3.8308 \times 10^{-1}$
310	$1.6811 \times 10^{-2}$	14.5	$3.8356 \times 10^{-1}$
240	$2.2649 \times 10^{-2}$	14.0	$3.9747 \times 10^{-1}$
180	$3.1638 \times 10^{-2}$	13.8	$4.0291 \times 10^{-1}$
130	$4.4626 \times 10^{-2}$	13.6	$4.0867 \times 10^{-1}$
100	$5.8877 \times 10^{-2}$	13.4	$4.1443 \times 10^{-1}$
84	$7.0777 \times 10^{-2}$	13.2	$4.2067 \times 10^{-1}$
68	$8.8484 \times 10^{-2}$	13.0	$4.2786 \times 10^{-1}$
52	$1.1747 \times 10^{-1}$	12.8	$4.6049 \times 10^{-1}$
36	$1.7322 \times 10^{-1}$	12.6	$5.0224 \times 10^{-1}$
30	$2.1001 \times 10^{-1}$	12.4	$5.5806 \times 10^{-1}$
27	$2.3480 \times 10^{-1}$	12.2	$6.5499 \times 10^{-1}$
24	$2.6583 \times 10^{-1}$	12.0	$7.5192 \times 10^{-1}$
23.5	$2.7191 \times 10^{-1}$	11.9	$8.0038 \times 10^{-1}$
23.0	$2.7815 \times 10^{-1}$	11.8	$8.4885 \times 10^{-1}$
22.5	$2.8471 \times 10^{-1}$	11.7	$8.9732 \times 10^{-1}$
22.0	$2.9143 \times 10^{-1}$	11.6	$9.4594 \times 10^{-1}$

Table 2.2: The Derived Silicon Carbide Relative Opacity Function (cont'd)  
 The SiC opacity for SiC dust, normalized to  $11.3\mu\text{m}$ , (Chan, 1988).

Wavelength ( $\mu\text{m}$ )	Relative Opacity	Wavelength ( $\mu\text{m}$ )	Relative Opacity
11.5	$9.6801 \times 10^{-1}$	8.5	$5.9533 \times 10^{-1}$
11.4	$9.8401 \times 10^{-1}$	8.4	$5.9437 \times 10^{-1}$
11.3	$1.0000 \times 10^0$	8.3	$5.9341 \times 10^{-1}$
11.2	$9.8401 \times 10^{-1}$	8.2	$5.9245 \times 10^{-1}$
11.1	$9.6801 \times 10^{-1}$	8.1	$5.9149 \times 10^{-1}$
11.0	$9.5441 \times 10^{-1}$	8.0	$5.9053 \times 10^{-1}$
10.9	$9.2019 \times 10^{-1}$	7.6	$5.4239 \times 10^{-1}$
10.8	$8.8612 \times 10^{-1}$	7.2	$4.9440 \times 10^{-1}$
10.7	$8.5189 \times 10^{-1}$	6.8	$4.4642 \times 10^{-1}$
10.6	$8.0406 \times 10^{-1}$	6.4	$3.9827 \times 10^{-1}$
10.5	$7.6280 \times 10^{-1}$	6.0	$3.5029 \times 10^{-1}$
10.4	$7.2329 \times 10^{-1}$	5.6	$3.4997 \times 10^{-1}$
10.3	$6.8554 \times 10^{-1}$	5.2	$3.4965 \times 10^{-1}$
10.2	$6.4939 \times 10^{-1}$	4.8	$3.6980 \times 10^{-1}$
10.1	$6.1468 \times 10^{-1}$	4.4	$4.1651 \times 10^{-1}$
10.0	$5.8173 \times 10^{-1}$	4.0	$4.7457 \times 10^{-1}$
9.9	$5.5006 \times 10^{-1}$	3.6	$5.4814 \times 10^{-1}$
9.8	$5.5582 \times 10^{-1}$	3.2	$6.4411 \times 10^{-1}$
9.7	$5.6174 \times 10^{-1}$	2.8	$7.5960 \times 10^{-1}$
9.6	$5.6782 \times 10^{-1}$	2.4	$9.0115 \times 10^{-1}$
9.5	$5.7390 \times 10^{-1}$	2.0	$1.0320 \times 10^0$
9.4	$5.8029 \times 10^{-1}$	1.8	$1.2339 \times 10^0$
9.3	$5.8669 \times 10^{-1}$	1.6	$1.4130 \times 10^0$
9.2	$5.9325 \times 10^{-1}$	1.4	$1.6379 \times 10^0$
9.1	$5.9997 \times 10^{-1}$	1.2	$1.9434 \times 10^0$
9.0	$5.9997 \times 10^{-1}$	1.0	$2.3800 \times 10^0$
8.9	$5.9901 \times 10^{-1}$	0.8	$3.0486 \times 10^0$
8.8	$6.4715 \times 10^{-1}$	0.6	$4.1939 \times 10^0$
8.7	$6.4012 \times 10^{-1}$	0.4	$5.7997 \times 10^0$
8.6	$6.3324 \times 10^{-1}$	0.2	$1.1200 \times 10^1$
		0.1	$2.1625 \times 10^1$

## 2.2 The Circumstellar Dust Shell

The terms *circumstellar dust shell (CDS)* or *circumstellar envelope (CSE)* define the region around a star, which is outside the star's atmosphere, but where the matter is identified with the star, (Wehrse, 1987). Evidence to this date does not determine whether there is a definite separation between the outer layer of the stellar atmosphere and the circumstellar envelope. The circumstellar dust shells come from the stellar wind of the central stars. Dust shells appear around stars of all spectral types with strong enough mass-loss rates ( $\sim 10^{-4}$  to  $10^{-8} M_{\odot} \text{ yr}^{-1}$ ), (de Jager, 1980). The dust grains absorb the radiation of the star and re-emit it as infrared radiation.

At this point, scattering of radiation becomes important. Scattering is an emission process which depends on the amount of radiation from the incident radiation field falling on an element of material; it is a process in which a particle effectively deflects a photon from its course, but does not alter the wavelength. The radiative transfer equation in the observer's frame of reference is

$$\begin{aligned} \frac{dI_{\nu}}{ds} &= -\kappa_{\nu} I_{\nu} + j_{\nu} \\ &= -\kappa_{\nu} (I_{\nu} - S_{\nu}). \end{aligned}$$

The absorption coefficient  $\kappa_{\nu}$  [ $\text{cm}^{-1}$ ] is often written as  $\kappa_{\nu} = \kappa'_{\nu} \rho$  where  $\rho$  is the mass density of the medium and  $\kappa'_{\nu}$  [ $\text{cm}^2 \text{ g}^{-1}$ ] is the mass absorption coefficient. The original source term  $S_{\nu}$  is often assumed to be the blackbody term  $B_{\nu}(T)$ . This changes when scattering and absorption are taken into account. (Often the transfer equation is written as a function of the emissivity  $\epsilon_{\nu}$ . The relationship between the emission coefficient  $j_{\nu}$  and the emissivity  $\epsilon_{\nu}$  [ $\text{erg g}^{-1} \text{ s}^{-1} \text{ Hz}^{-1}$ ], for isotropic emission, is

$j_\nu = \frac{\epsilon_\nu \rho}{4\pi}$ .) The emission coefficient  $j_\nu$ , which has units of  $\text{erg cm}^{-3} \text{s}^{-1} \text{ster}^{-1} \text{Hz}^{-1}$ , contains the scattering information such that  $j_\nu$  is a function of the absorption coefficient of the scattering process, called the *scattering* coefficient. For pure scattering, the equation of transfer has the form:

$$\frac{dI_\nu}{ds} = -\sigma_\nu^s(I_\nu - S_\nu^s)$$

where  $\sigma_\nu^s$  is the scattering coefficient, and  $S_\nu^s$  is the source function due to scattering processes.

For *combined* scattering and absorption processes, the transfer equation has the form:

$$\frac{dI_\nu}{ds} = -\sigma_\nu^a(I_\nu - S_\nu^a) - \sigma_\nu^s(I_\nu - S_\nu^s) \quad (2.1)$$

where  $\kappa_\nu \equiv \sigma_\nu^a + \sigma_\nu^s$  is the *net* absorption coefficient, or *extinction* coefficient. The true absorption coefficient is denoted by the term  $\sigma_\nu^a$ , while the term  $\sigma_\nu^s$  denotes the scattering coefficient. Scattering and absorption are due to different processes, thus the source function  $S_\nu$  has been split into an absorption source function and a scattering source function, (Volk, 1986).

Dust condenses in low density regions well outside the photosphere of the stars. Silicates condense at approximately  $T_c \approx 1500\text{K}$ , (Gilman, 1969), and since cool oxygen-rich giant and supergiants have photospheric (or effective) temperatures between 2000 and 3800K, most of the dust is expected to form at least a few stellar radii away from the center of these stars, (Zuckerman, 1980). Silicon carbide can condense at  $T_c \approx 1500\text{-}1700\text{K}$  (Zuckerman, 1980; McCabe, 1982), so for cool late-type carbon stars whose photospheric temperatures are in the low to mid 2000K range, dust *may* form closer to the star. For many stars that are observed to have

dust envelopes, it is surmised that dust can only condense a few stellar radii above the surface of the star, (Woolf, 1973).

## 2.3 Radiative Transfer Model

### 2.3.1 General Description of Modeling Code

The radiative transfer modelling code which was used to produce the model spectra was originally developed by C. M. Leung for the modeling of dust in molecular clouds and star formation regions. The original code (DUSTCD) and its method of use are described in Leung (1975, 1976) and Spagna and Leung(1983); (these references are recommended for details concerning the program and its numerical methods of solution to the radiative transfer equations). DUSTCD was further adapted and modified by K. Volk for his Ph.d. thesis, (1986). This will be discussed briefly later in this chapter.

In the modeling of the dust temperature profile and radiation field, the dust shell or cloud is allowed to be composed of up to five different types of dust, each separate type having a distinct density profile and a distinct opacity as a function of wavelength. Scattering and absorption of radiation is treated, and allowance is made for anisotropic scattering if desired. The possible sources of energy to heat the dust cloud are a star or a power-law spectrum source, (for example, an H II region). Conversely, the dust cloud may be isolated from any energy source except the 2.7K cosmic blackbody background radiation.

The density profile of the dust is assumed to be of the form  $n_d \propto r^q$ , where  $q$  is some number which can be either positive or negative. The radiative transfer

equations are solved by an iteration method to determine the source function at each part of the dust shell. From this source function, a steady-state temperature profile and total emergent flux for the dust shell are determined. It is assumed that the gas in the cloud or shell does not significantly affect the radiation field, (for example, by producing line emission).

### 2.3.2 Review of the Method of Solution of the Radiative Transfer Equations

The DUSTCD code developed by Leung (1975,1976) presents a numerical method for efficiently solving the radiative transfer equations, which he terms the *quasi-diffusion method* (QDM). The basic assumption made is that the radiation field is isotropic. The equation of transfer is as described in previous sections. The transfer equation can be written as, considering the effects of scattering and absorption,

$$\frac{dI_\nu}{ds} = -\sigma_\nu^a(I_\nu - S_\nu^a) - \sigma_\nu^s(I_\nu - S_\nu^s) \quad (2.2)$$

where the net absorption is  $\kappa_\nu \equiv \sigma_\nu^a + \sigma_\nu^s$ , ( $\sigma_\nu^a$  is the pure absorption coefficient,  $\sigma_\nu^s$  is the scattering coefficient). The intensity is affected by both absorption and scattering, thus there are two terms proportional to  $I_\nu$ . But emission and absorption of radiation may be governed by more than one process, different processes being responsible for absorption and scattering, thus there are two separate source terms. The absorption source term  $S_\nu^a$  is simply the blackbody source term  $B_\nu(T)$ . The scattering source term  $S_\nu^s$  is due to radiation from other directions scattered into the direction  $\mu$  where  $dr = \cos \theta ds = \mu ds$  in which  $\mu$  is the cosine of the angle between the outward normal and the direction of radiation propagation. This

term is expressed as a function of the scattering efficiency phase function  $p_\nu(\mu, \mu')$  which determines the probability of scattering from direction  $\mu'$  into direction  $\mu$ , for photons of frequency  $\nu$ :

$$S_\nu^s(\mu) = \frac{1}{2} \int_{-1}^1 I_\nu(r, \mu') p_\nu(\mu, \mu') d\mu',$$

(Leung, 1975). The term  $r$  is simply the standard coordinate of radial distance from changing to the position coordinates  $(r, \mu)$ . The equation of radiation transport for an isotropic source with spherical symmetry becomes (Leung, 1975),

$$\begin{aligned} \mu \frac{\partial I_\nu(r, \mu)}{\partial r} + \left[ \frac{1 - \mu^2}{r} \frac{\partial I_\nu(r, \mu)}{\partial \mu} \right] = & -\sigma_\nu^a(r) [I_\nu(r, \mu) - B_\nu(r, T)] \\ & - \sigma_\nu^s(r) \left[ I_\nu(r, \mu) - \frac{1}{2} \int_{-1}^1 I_\nu(r, \mu') p_\nu(\mu, \mu') d\mu' \right]. \end{aligned} \quad (2.3)$$

Leung assumes in the above equation that the cloud is independent of azimuthal angles. Leung expands the phase function  $p_\nu(\mu, \mu')$  as a series in Legendre polynomials

$$p_\nu(\mu, \mu') \approx \sum_{l=0}^L a_l P_l(\mu) P_l(\mu'),$$

where  $a_l$  are constants.

In order to solve equation 2.3, Leung defines the  $n$ th moment over the radiation field as,

$$M_\nu^n(r) \equiv \frac{1}{2} \int_{-1}^1 I_\nu(r, \mu) \mu^n d\mu.$$

The first three moments of the intensity  $I_\nu$  are the mean intensity  $J_\nu \equiv M_\nu^0$ , the Eddington flux  $H_\nu \equiv M_\nu^1$ , and the K-integral  $K_\nu \equiv M_\nu^2$ , which is related to the radiation pressure.

$$M_\nu^0 \equiv J_\nu = \frac{1}{2} \int_{-1}^1 I_\nu d\mu \quad (2.4)$$



$$M_\nu^1 \equiv H_\nu = \frac{1}{2} \int_{-1}^1 \mu I_\nu d\mu \quad (2.5)$$

$$M_\nu^2 \equiv K_\nu = \frac{1}{2} \int_{-1}^1 \mu^2 I_\nu d\mu \quad (2.6)$$

Taking the first and second moments against  $\mu$  of equation 2.3, Leung obtains coupled non-linear moment equations for radiative transfer, which he then solves by introducing and defining two auxiliary functions. The first dimensionless variable is the anisotropy factor, also known as the *Eddington factor*,  $f_\nu \equiv \frac{K_\nu(r)}{J_\nu(r)}$ , which describes the angular distribution of the radiation field. The second dimensionless variable is the configuration function, which, for spherical geometry, has been defined as

$$\zeta_\nu(r) = \exp \left[ \int_0^r \left( 3 - \frac{1}{f_\nu(x)} \right) \frac{dx}{x} \right].$$

The configuration function depends on the geometry of the system and on the anisotropy factor. For an isotropic radiation field, the anisotropy factor is  $f_\nu = \frac{1}{3}$  (which comes from the first Eddington approximation which gives  $K_\nu = \frac{1}{3}J_\nu$ ), and the configuration function is  $\zeta_\nu = 1$ , (Leung, 1975).

The final form of the combined moment equation for spherical geometry is (Leung, 1975),

$$\frac{\partial}{\partial r} \left[ \frac{r^2}{\kappa_\nu \zeta_\nu} \frac{\partial}{\partial r} (f_\nu \zeta_\nu J_\nu) \right] = r^2 (\kappa_\nu^* J_\nu - \epsilon_\nu^*), \quad (2.7)$$

where

$$\kappa_\nu^* \equiv \sigma_\nu^a(r) = n_d(r) \langle Q_{abs} \pi a^2 \rangle_\nu \quad (2.8)$$

$$\epsilon_\nu^* \equiv \sigma_\nu^a(r) B_\nu(r, T) = n_d(r) \langle Q_{abs} \pi a^2 \rangle_\nu B_\nu(r, T) \quad (2.9)$$

$$\kappa_\nu \equiv n_d [ \langle Q_{abs} \pi a^2 \rangle_\nu + (1 - \langle g \rangle_\nu) \langle Q_{sca} \pi a^2 \rangle_\nu ]. \quad (2.10)$$

The term  $n_d(r)$  is the number density of dust grains;  $B_\nu(r, T)$  is the Planck function corresponding to grain temperature  $T_D(r)$ ;  $\langle Q_{abs}\pi a^2 \rangle_\nu$  and  $\langle Q_{sca}\pi a^2 \rangle_\nu$  are the effective absorption and scattering cross-sections for spherical grains, for which the absorption and scattering efficiency factors  $Q_{abs}$  and  $Q_{sca}$  can be determined through Mie theory. The term  $\langle g \rangle_\nu$  is the effective asymmetry parameter; for isotropic scattering  $\langle g \rangle_\nu = 0$ . The effective cross-sections and effective asymmetry parameter are weighted parameters, integrated over a distribution of grain sizes.

At steady-state there is no net energy loss or gain at any point in the shell or cloud. The condition for radiative equilibrium is (Leung, 1975),

$$\int_0^\infty (\epsilon_\nu^* - \kappa_\nu^* J_\nu) d\nu = 0$$

$$\int_0^\infty \sigma_\nu^a B_\nu(r, T) d\nu = \int_0^\infty \sigma_\nu^a J_\nu(r) d\nu$$

$$\int_0^\infty B_\nu(r, T) \langle Q_{abs}\pi a^2 \rangle_\nu d\nu = \int_0^\infty J_\nu(r) \langle Q_{abs}\pi a^2 \rangle_\nu d\nu. \quad (2.11)$$

This condition of radiative equilibrium determines the grain temperature  $T_D(r)$  at each point in the cloud, and subsequently the source function at each point. The DUSTCD code solves the equations by iterations, assuming the radiation field is isotropic. From the source function, a new temperature profile is calculated, and the process iterates until a steady-state temperature profile is found, up to a maximum of twenty iterations, (as modified by Volk). The reader is referred to Leung (1975, 1976) for more information behind the method of solution of the radiative transfer equation.

### 2.3.3 Overview of the Modified Code

The numerical integration of the equations used is the method of finite differences, (a description of this method may be found in advanced mathematics texts such as Wylie (1960), chapter 5). For each frequency considered, which is input by the use of a frequency grid which defines the spectrum, the dust cloud is split into a number of shells using a radial grid. The original DUSTCD code employed a radial grid of 55 points and a frequency grid of 60 points. Volk modified the code to allow for a radial grid of 161 points and a frequency grid of 121 points in order to obtain more detailed models of the spectrum. Leung originally had a linear radial grid, but this was changed by Volk to a radial grid in logarithmic form between the dust condensation radius and the outer radius, which is 250 times the condensation radius. There are 27 grid points for the first order of magnitude change in radius, and 67 grid points per order of magnitude change for the subsequent change in radius. For a star embedded in a dust shell, a model is calculated which assumes the radiation is scattered isotropically, with no external radiative source save the 2.7K cosmic background. Originally the maximum number of iterations was twelve, but this was changed to twenty by Volk.

For our models, only one grain type was assumed per model. For the carbon stars, the grain type chosen was silicon carbide (SiC), whose  $11.3\mu\text{m}$  feature served as the reference frequency. For the oxygen-rich M-type stars, silicate was assumed to be the grain type, where the  $9.7\mu\text{m}$  absorption feature served as the reference frequency. The grain absorption efficiency for a particle of radius  $0.1\mu\text{m}$  is (i) for silicate, at the reference frequency of  $9.7\mu\text{m}$ ,  $Q_{9.7} \approx 0.13$ , (Chan, 1988); (ii) for

silicon carbide, at the reference frequency of  $11.3\mu m$ ,  $Q_{11.3} \approx 0.33$ , (Chan, 1988). The density profile of the dust for our models, assuming constant mass loss and outflow velocity, was assumed to be of the form  $n_d \propto r^{-2}$ . Dust condensation temperatures of  $\sim 1500K$  were assumed for both silicate dust and silicon carbide dust.

## Chapter 3

### Submillimetre and IRAS Observations

#### 3.1 IRAS

The Infrared Astronomical Satellite (*IRAS*) is a joint project of the United States National Aeronautics and Space Administration (NASA), the Netherlands Agency for Aerospace Programs (NIVR), and the United Kingdom Science and Engineering Research Council (SERC). The objective of this project, which began in 1975 with the satellite itself being launched in January of 1983, was the surveying of the sky from space in the middle to far infrared spectral region. By November of 1983, 10 months after launch, it had successfully surveyed more than 96% of the sky in four different wavebands centered at 12, 25, 60, and  $100\mu\text{m}$ , (*IRAS Explanatory Supplement*, 1985). More than 245 000 point sources were detected; these are listed in the *IRAS Point Source Catalogue (PSC)*. An atlas of sky brightness images, which is a survey of the sky with a resolution of  $4'$  (four arcminutes), was produced. A catalogue of extended sources smaller than  $8'$ , which contains approximately 20 000 objects, is listed as the *IRAS Small Structure Catalogue (SSC)*. Infrared spectra from  $7.7\mu\text{m}$  to  $22.6\mu\text{m}$  of 5425 bright point sources were listed in the *IRAS Low Resolution Spectra Catalogue (LRSC)*. The data in this thesis are found in the PSC with their low resolution spectra data found in the LRSC.

### 3.1.1 Point Source Catalogue Overview

The *IRAS* Point Source Catalogue (PSC) contains 245 839 point sources, and is one of the largest collections of astronomical sources with positional data and measured fluxes. The uniform coverage of the surveyed sky consisted of approximately 72% of the sky being scanned separately three or more times, with about 24% of the sky receiving two separate coverages. The maximum angular sizes of the point sources detected are 0.5', 0.5', 1.0', and 2.0' in the 12, 25, 60, and 100 $\mu$ m wavebands, respectively. Approximately 55% of these point sources are stars. Of this 55%, approximately 7% are stellar sources with naked photospheres or with a surrounding of a small amount of circumstellar dust, with blackbody temperatures above 1500 K; approximately 23% have circumstellar dust shells; approximately 24% are faint stars which fall into either of the aforementioned 7% and 23%, (Chan, 1988). Further details of the point source data reduction are readily found in the *IRAS* Explanatory Supplement (1985).

### 3.1.2 Low Resolution Spectra Catalogue Overview

The Low Resolution Spectra Catalogue (LRSC) contains spectra of 5425 bright point sources for the wavelengths from 7.7 $\mu$ m to 22.6 $\mu$ m. The spectral resolution ( $\lambda/\Delta\lambda$ ) varies from 20 to 60 over the waveband. The low resolution spectrometre made observations of point sources brighter than 2Jy at 12 $\mu$ m or 25 $\mu$ m, in two wavelength ranges of 7.7 to 13.4 $\mu$ m and 11.0 to 22.6 $\mu$ m. Most ( $\sim 96\%$ ) of the LRSC sources are stars with oxygen-rich or carbon-rich circumstellar dust shells, (Chan, 1988).

The classification system used in the *IRAS* LRSC is defined by the presence of

dust features in the spectrum. Dust features such as the  $10\mu m$  silicate emission and absorption features are found in 2113 of the 5425 spectra, with 538 showing the  $11\mu m$  silicon carbide (SiC) emission feature, (Chan, 1988). The Classification system for LRSC classes involving late-type stars goes as follows (*IRAS Explanatory Supplement*):

**LRSC Class 10-19:** 2246 objects with spectral types M5 or earlier; no features in the spectrum. Spectrum has a *blue* continuum.

**LRSC Class 20-29:** 1738 objects which show the  $10\mu m$  silicate emission feature; M stars with stellar winds and a dust envelope. Spectrum has a *blue* continuum.

**LRSC Class 30-39:** 230 objects which show the  $10\mu m$  silicate absorption feature; M stars with thicker dust envelopes. Spectrum has a *blue* continuum.

**LRSC Class 40-49:** 538 objects which show the  $11.3\mu m$  SiC emission feature; carbon stars with dust shells. Spectrum has a *blue* continuum.

**LRSC Class 50-59:** 63 objects with no features in the spectrum. Spectrum has a *red* continuum.

**LRSC Class 60-69:** 78 objects which show the  $10\mu m$  emission feature; M stars with an even thicker envelope. Spectrum has a *red* continuum.

**LRSC Class 70-79:** 67 objects which show the  $10\mu m$  absorption feature; M star with thickest dust envelopes of all stars which have the  $10\mu m$  absorption feature in their spectrum. Spectrum has a *red* continuum.

**LRSC Class 00-05:** 363 objects; they have low signal-to-noise ratios or are miscellaneous such that they do not fit into other classes.

The *blue* and *red* continuum spectral groups are grouped in relation to the spectral index between 14 and  $22\mu m$ . The spectral index  $\beta$  is defined by  $F_\lambda \propto \lambda^\beta$ . The continuum is *blue* if the  $\lambda F_\lambda$  value rises between 22 and  $14\mu m$ ; if  $\lambda F_\lambda$  does not rise between 22 and  $14\mu m$ , the spectrum is defined as having a *red* continuum.

## 3.2 JCMT

Submillimetre observations were obtained on February 7th and February 8th, 1988, at the James Clerk Maxwell Telescope (JCMT) on the 4200m summit of Mauna Kea in Hawaii using the UKT 14 photometre. The JCMT is one of the largest telescopes in the world capable of operating in the millimetre and submillimetre wavebands, (Matthews, 1988). The telescope is managed by the Royal Observatory Edinburgh, with support from the United Kingdom Science and Engineering Council (SERC), the Canadian National Research Council (NRC), and the Netherlands' Nederladse Organisatie Voor Wetenschappelijk Onderzoek. There is currently an on-going investigation into the performance of the JCMT and its equipment; presented in this thesis is what is generally known to date.

### 3.2.1 Technical Specifications

#### The Telescope

The alt-azimuth telescope consists of a mounted Cassegrain reflector. (A reflecting Cassegrain system consists of a small convex reflector (the secondary reflector)



suspended above the main (primary) reflecting reflector. The convex reflector intercepts the radiation before it reaches the prime focus and reflects it back down into a hole in the centre of the main objective reflector, (Abell, 1982). The secondary focus is *behind* the primary reflector.) The JCMT main parabolic reflector is 15m in diameter, consisting of 276 aluminum panels arranged in seven rings about the central hole. The central hole in the reflector is one metre in diameter, (Wolstencroft and Burton,1988). The secondary reflector is a 75cm hyperboloid, supported by an eight-legged, four-footed structure, (figure 3.1). This secondary reflector can be moved in the  $x$  and  $y$ , and the  $z$  directions. It can also be vibrated about any axis in the  $x$ - $y$  plane, up to a maximum chopping frequency of 15 Hz. The maximum chop amplitude (throw) is 8 arcminutes ( $8'$ ). The default chopping frequency is 7.8125 Hz for good chop throws of up to 150 arcseconds ( $150''$ ). If a larger chop throw is wanted, the chop frequency is reduced according to the relation:

$$\text{Chop frequency(Hz)} < [125 / (\text{Chop throw in arcmin})]^{\frac{1}{2}}$$

(Matthews, 1988). For our stellar objects, we used a  $60''$  chop throw. The presence of a third reflector located below the prime reflector in the area of the secondary focus directs the incoming radiation to the receivers.

The telescope is housed in a carousel which rotates with the antenna (ie. the telescope). Normally, a membrane of woven PTFE (teflon), transparent to millimetre and submillimetre wavelengths, protects the telescope from exposure to the sun, wind, and dust, (Matthews, 1988). The cylindrical carousel has a height of 22 metres, a width of 28 metres, and a weight of 450 tonnes (Wolstencroft and Burton, 1988).

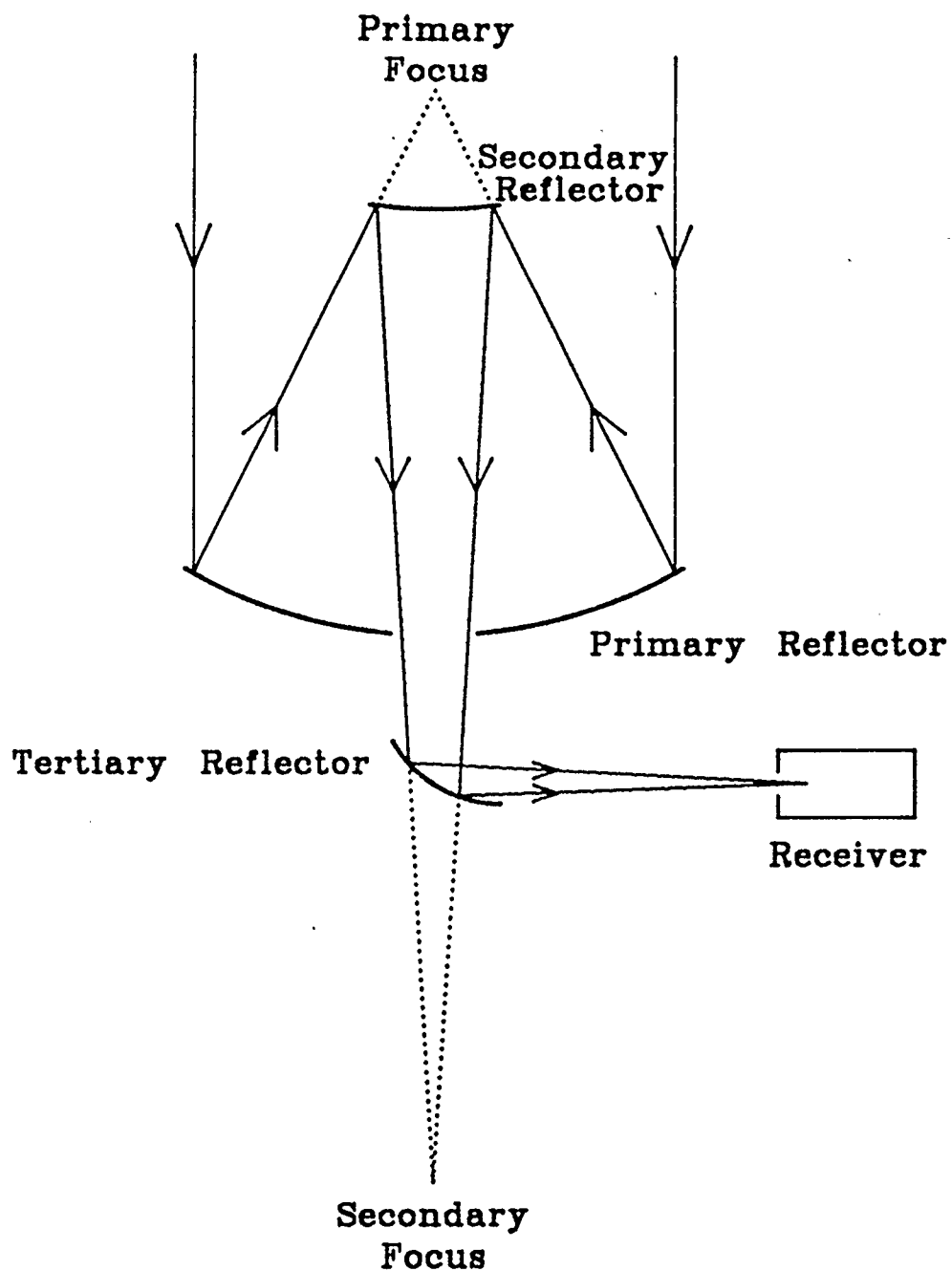


Figure 3.1: Schematic of the JCMT Cassegrain reflector system. The primary reflector is 15m in diameter, with 276 aluminum panels arranged in seven rings. The 75cm hyperboloid secondary reflector is supported by an eight-legged, four-footed structure.

The location of the antenna, with Hawaiian Standard as the local time, is:

Longitude:  $155^{\circ} 28' 47''$

Latitude:  $19^{\circ} 49' 33''$

Altitude: 4074m.

Important operational limits of the telescope are such that the upper observable elevation limit is  $87^{\circ}$ , while the lower limit is  $5^{\circ}$ , (Matthews, 1988).

### The Receivers

At time of writing, there are three front end receivers and two back end receivers in the JCMT.

The UKT 14, which was the front end receiver used in the observations obtained for this thesis, is a millimetre/submillimetre continuum photometre. Originally built for the UK Infrared Telescope, it is now permanently on the JCMT. The UKT 14 uses a single-pixel bolometric detector which is cooled to  $0.36K$  by liquid helium three ( $^3\text{He}$ ) as the primary coolant, ( $^4\text{He}$  and nitrogen are secondary coolants). Input radiation from the optical system of the antenna is linked to the bolometre by means of the hyperbolic tertiary (third) mirror, a cooled Fabry lens, and a parabolic horn. The Fabry lens is 65mm in diameter, and this sets the maximum aperture size. This maximum aperture size of 65mm corresponds to a beamwidth of approximately 20 arcseconds ( $20''$ ), (table 3.1). The UKT 14 is used for continuum photometry and mapping at wavelengths between 2mm and  $350\mu\text{m}$ , (frequencies of 150 to 870 GHz).

Two other front end receivers are available at the JCMT: the heterodyne A1 receiver, for  $\lambda \approx 1.3\text{mm}$  (frequency region 320 - 270 GHz); the heterodyne B1

Table 3.1: Beamwidths for Filters.

Beamwidths as known at time of observation, February 1988. This is for a fixed aperture size of 65mm.

Filter ( $\mu m$ )	Beamwidths $\Theta_A$ (arcseconds)	Center Frequency (GHz)	Bandwidth (GHz)
1100	19	264	75
800	$\sim 20$	394	103
450	$\sim 20$	685	84

receiver, for  $\lambda \approx 0.9\text{mm}$  (frequency region 320 - 356 GHz). These two receivers are used primarily for spectral line observations, (Matthews, 1988). The two back end receivers, which take care of frequency resolution, consist of a digital auto-correlation spectrometre (built by the University of Kent), and an acousto-optical spectrometre (AOS) (built by the University of Utrecht). Further details of the JCMT specifications are found in the JCMT Users Guide, released in July, 1988, by H.E. Matthews.

### 3.2.2 Observing Procedures

The observations were done by observing the desired object to obtain a *scan*. A scan consists of observing an object through a specified filter, for a specific integration (scanning) time, at a specified chop frequency and chop throw, and for a fixed aperture size. The observing procedures consisted of three main tasks: calibration and atmospheric extinction observations, pointing checks, source observations.

In order to be able to later calibrate the data, calibration observations must be made. The best calibration source is Mars, although Venus, Jupiter, Saturn, Neptune and Uranus are also usable, (Matthews, 1988). If no planets are readily

observable, compact H II regions or planetary nebulae are appropriate for use. The night of February 7th, the calibration source used was Jupiter. The following night (February 8th), the calibration source used was Mars. These planets were both observed using *each* of the  $1100\mu m$ ,  $800\mu m$ , and  $450\mu m$  filters.

Atmospheric extinction factors must be taken into account, thus throughout the observing runs of each night scans were made of a particular source at each of the wavebands. At least three different scans (for *each* waveband) are needed at different airmasses in order to properly calculate the atmospheric extinction coefficient. For February 7th, the object 3C84 was used; it was scanned at four different airmasses for each of the 450, 800, and  $1100\mu m$  filters. For February 8th, the object CW Leo (IRC +10216) was used. CW Leo was scanned at four different airmasses at each of the 800 and  $1100\mu m$  filters. Unfortunately, time did not allow for a sufficient number of scans of CW Leo at the  $450\mu m$  filter for extinction calculation purposes, thus Mars was used in later calculations of the extinction coefficient at  $450\mu m$ .

A crucial step in the observing run is to verify the pointing of the telescope frequently. For each new source to be observed, it is a good idea to check the accuracy of the pointing first by doing a *five-point check*. The beam profiles have a roughly Gaussian shape, and the five-point check assumes a gaussian curve can be fitted to the results of the check. The five-point check routine automatically performs a five point grid (*North South Centre West East*) and fits a gaussian beam shape to the results, (UKT 14 Description and Operating Manual). Because this gaussian is assumed, large disc-like objects such as the Moon or Jupiter do not give correct results. Good pointing results require a bright compact source.

Many five-point checks were made throughout the observing runs of February 7th and 8th, and took up much of the observing time allotted to us. By the end of the final observing run (on February 8th), a total of 120 scans, which included the pointing checks, and the extinction and calibration scans, were obtained. Scans 001 through 049 were obtained on the night of the 7th, while the remaining scans numbered 050 to 120 were obtained on the night of the 8th.

### 3.2.3 Data Reduction

#### Extinction

In order to calibrate the observed submillimeter data, atmospheric extinction had to be accounted for. In order to determine the extinction coefficients and their errors for each filter wavelength, a linear least-squares fit was applied to the slope of the log of observed flux (in millivolts) versus the airmass.

The observed data were obtained over two successive nights - the evening of February 7th, 1988, and the evening of February 8th, 1988. A total of 120 scans of data sources, including calibrators, were made. To obtain the extinction for the night of February 7th, the observed source 3C84 was used. 3C84 was observed at various times throughout the night with each filter for just this purpose. The extinction coefficients for this night were subsequently determined to be

$$\begin{aligned}
 |\alpha_{1100\mu m}| &= 0.26 \pm 0.01 \\
 |\alpha_{800\mu m}| &= 0.62 \pm 0.02 \\
 |\alpha_{450\mu m}| &= 1.13 \pm 0.54.
 \end{aligned}$$

For the evening of February 8th, two objects had to be used in order to de-

determine extinction. CW Leo was used to determine the extinction coefficients for  $1100\mu m$  and  $800\mu m$ , while Mars was used to determine the extinction coefficient at  $450\mu m$ . The extinction coefficients for this night were subsequently determined to be

$$|\alpha_{1100\mu m}| = 0.11 \pm 0.01$$

$$|\alpha_{800\mu m}| = 0.39 \pm 0.06$$

$$|\alpha_{450\mu m}| = 1.74 \pm 0.06.$$

### Calibration

In order to calibrate the observed fluxes, the correction factor  $K$  had to be determined. The detector observes only  $\frac{1}{K}$  of the true flux, so the known flux of the calibration planet  $F_\lambda$  is divided by  $K$  to obtain the expected flux in Janskys. The correction factor  $K$  was determined using the relation

$$K = \frac{z^2}{1 - e^{-z^2}}$$

where

$$z = \frac{SD}{0.6 \Theta_A}$$

where  $SD \equiv$  the semi-diameter of the object, and  $\Theta_A \equiv$  the beamwidth. The resulting flux is then corrected for extinction. We then compare this flux in Jansky units to the observed flux in millivolt units to obtain the flux conversion factor  $F_{Jy/mV}$  in  $\frac{Jy}{mV}$ . The relation is

$$F_{Jy/mV} = \frac{F_\lambda}{K} \frac{e^{-\alpha x_{cal}}}{f_{cal}}, \quad (3.1)$$

where  $f_{cal}$  is the flux of the calibration planet as observed in millivolts, and  $x_{cal}$  is the airmass of the planet at the time of observation.

## Chopping and Nodding

Infrared and submillimetre photometry uses a procedure known as *chopping*. The detector is focused alternately on two neighboring patches of the sky, which are called *beams*, and the difference between them is recorded electronically. The chopping frequency between the two beams depends on the response time of the detector; the JCMT default chopping frequency was 7.8125 Hz. Chopping provides a detected signal which is the difference between the signal from the sky containing the source of interest and the signal from the sky at the reference beam. If the background is identical in the two beams, it (background) cancels out, so that only the signal from the source located in one or the other beams is recorded (Allen, 1975). If there is a gradient of the sky brightness, then the two beams will not have identical background, and the resulting signal would be false. To eliminate this possibility of a false signal, the process of *nodding*, also called *beam-switching*, is used. In this procedure, two reference beams are used, one on either side of the source beam. Nodding is the process of driving the telescope back and forth between the two reference beams. The separation between these two reference beams must be larger than the diameter of the beam itself, but must be small enough to make sure the background signals in the two beams are closely related (Allen, 1975). For typical scanning (integration) times, the telescope must move every 20 to 30 seconds. Typical total integration times per star while observing at the JCMT were 200 to 400 seconds.

Some examples of the raw signals for various objects are presented in figures 3.2 to 3.7. These traces are from the chart recorder as used at the JCMT at the time of the observing runs.



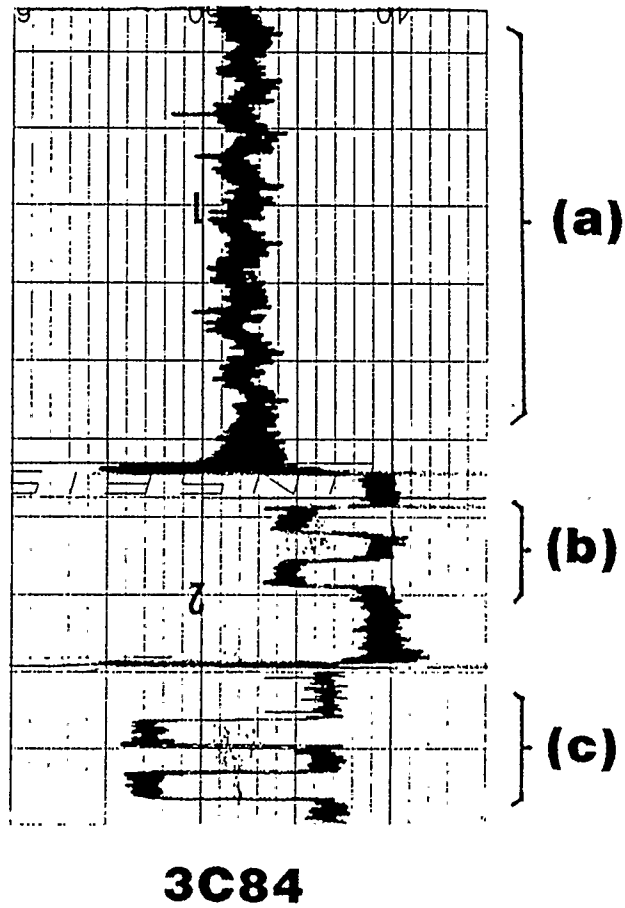
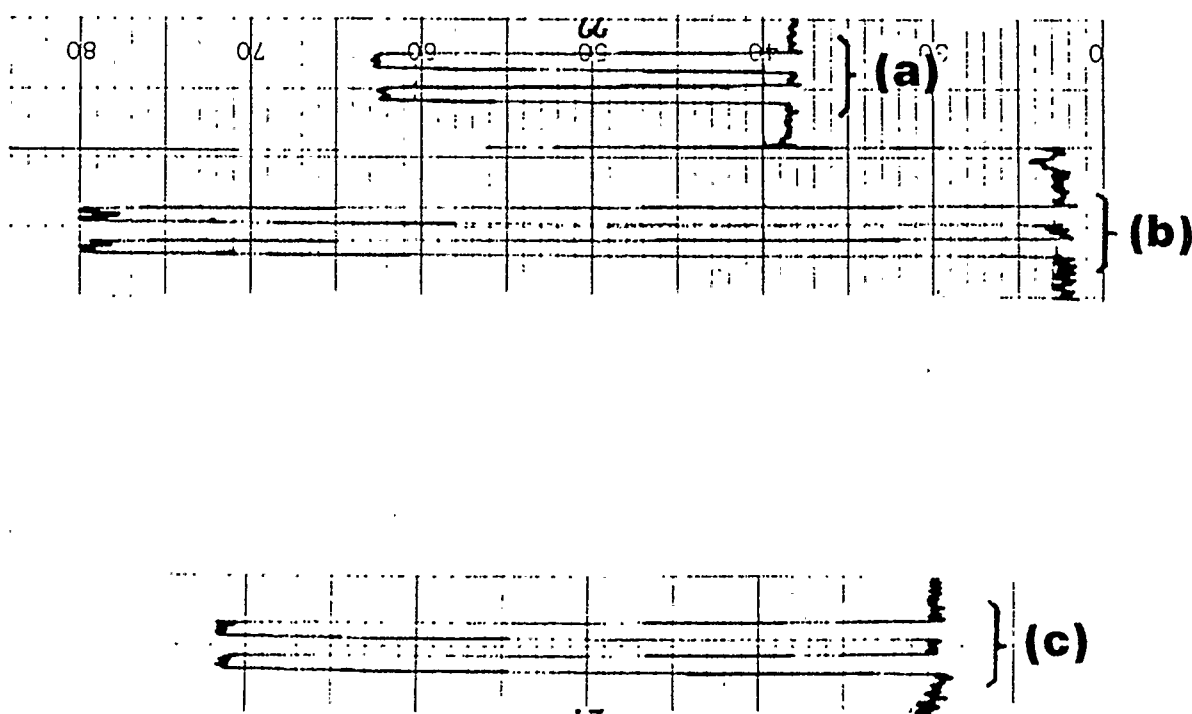
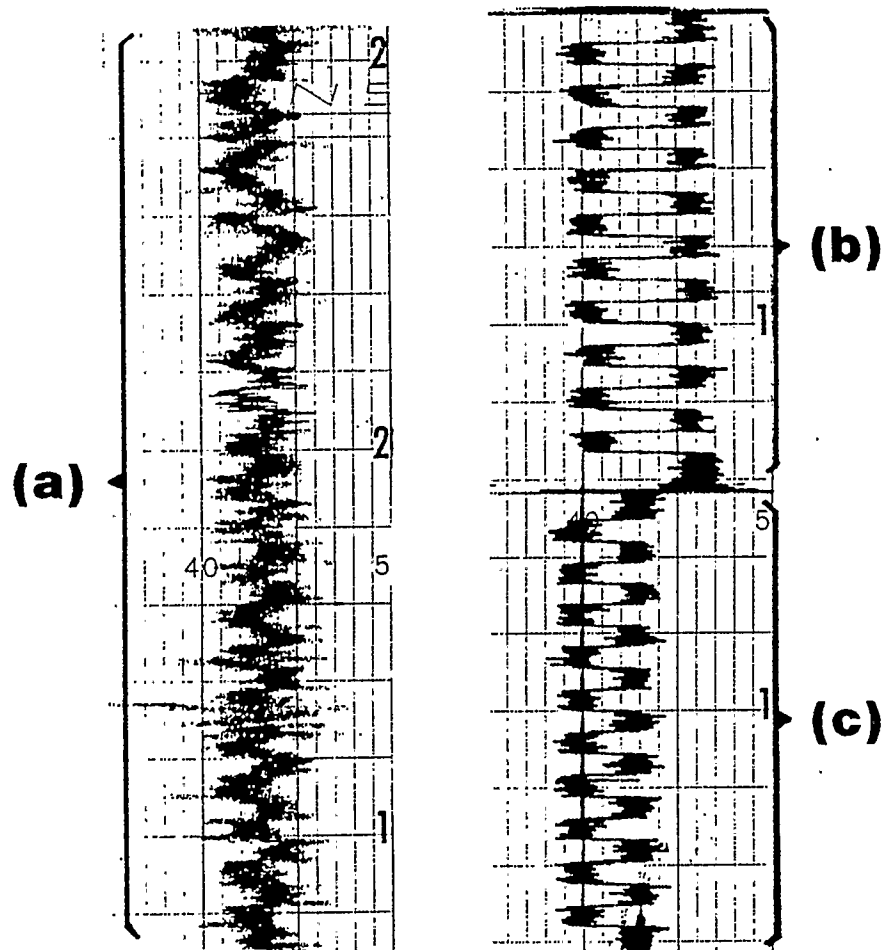


Figure 3.2: Chart recorder trace for 3C84 at 450, 800, and 1100 $\mu m$ : (a) Trace at 450 $\mu m$  (SCAN031); 1mV scale; (b) Trace at 800 $\mu m$  (SCAN030); 1mV scale; (c) Trace at 1100 $\mu m$  (SCAN029); 1mV scale.



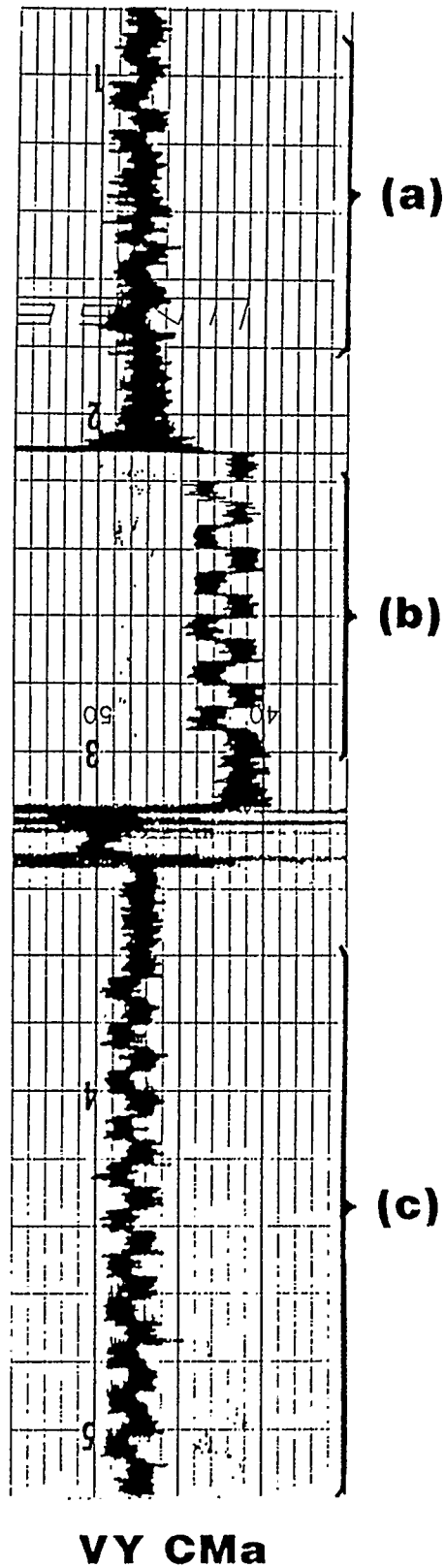
## Jupiter

Figure 3.3: Chart recorder traces for Jupiter at 450, 800, and 1100 $\mu m$ : (a) Trace at 450 $\mu m$  (SCAN001); 100mV scale; (b) Trace at 800 $\mu m$  (SCAN003); 100mV scale; (c) Trace at 1100 $\mu m$  (SCAN004); 100mV scale.



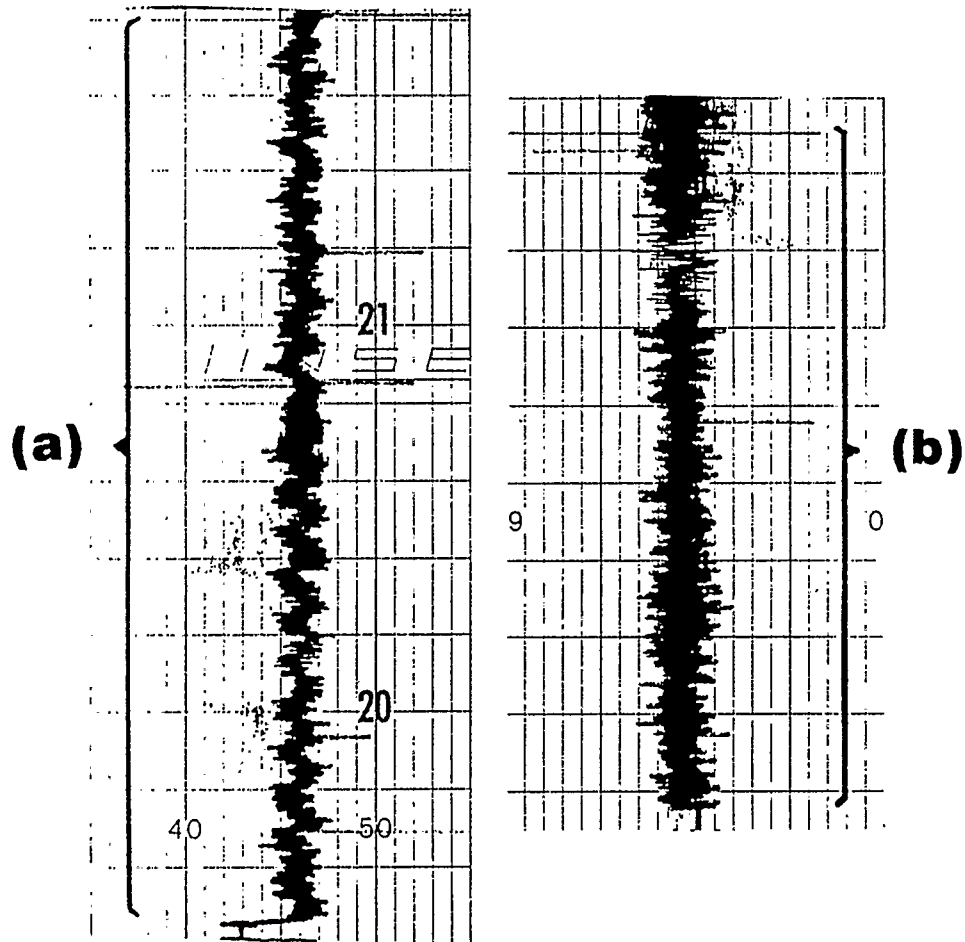
### CW Leo

Figure 3.4: Chart recorder traces for CW Leo at 450, 800, and 1100 $\mu\text{m}$ : (a) Trace at 450 $\mu\text{m}$  (SCAN068); 1mV scale; (b) Trace at 800 $\mu\text{m}$  (SCAN079); 1mV scale; (c) Trace at 1100 $\mu\text{m}$  (SCAN078); 1mV scale.



### VY CMa

Figure 3.5: Chart recorder traces for VY CMa at 450, 800 and 1100 $\mu m$ : (a) Trace at 450 $\mu m$  (SCAN041); 1mV scale; (b) Trace at 800 $\mu m$  (SCAN040); 1mV scale; (c) Trace at 1100 $\mu m$  (SCAN039); 1mV scale.



## RW LMi

Figure 3.6: Chart recorder traces for RW LMi at 800 and 1100 $\mu\text{m}$ : (a) Trace at 800 $\mu\text{m}$  (SCAN096); 1mV scale; (b) Trace at 1100 $\mu\text{m}$  (SCAN047); 1mV scale.

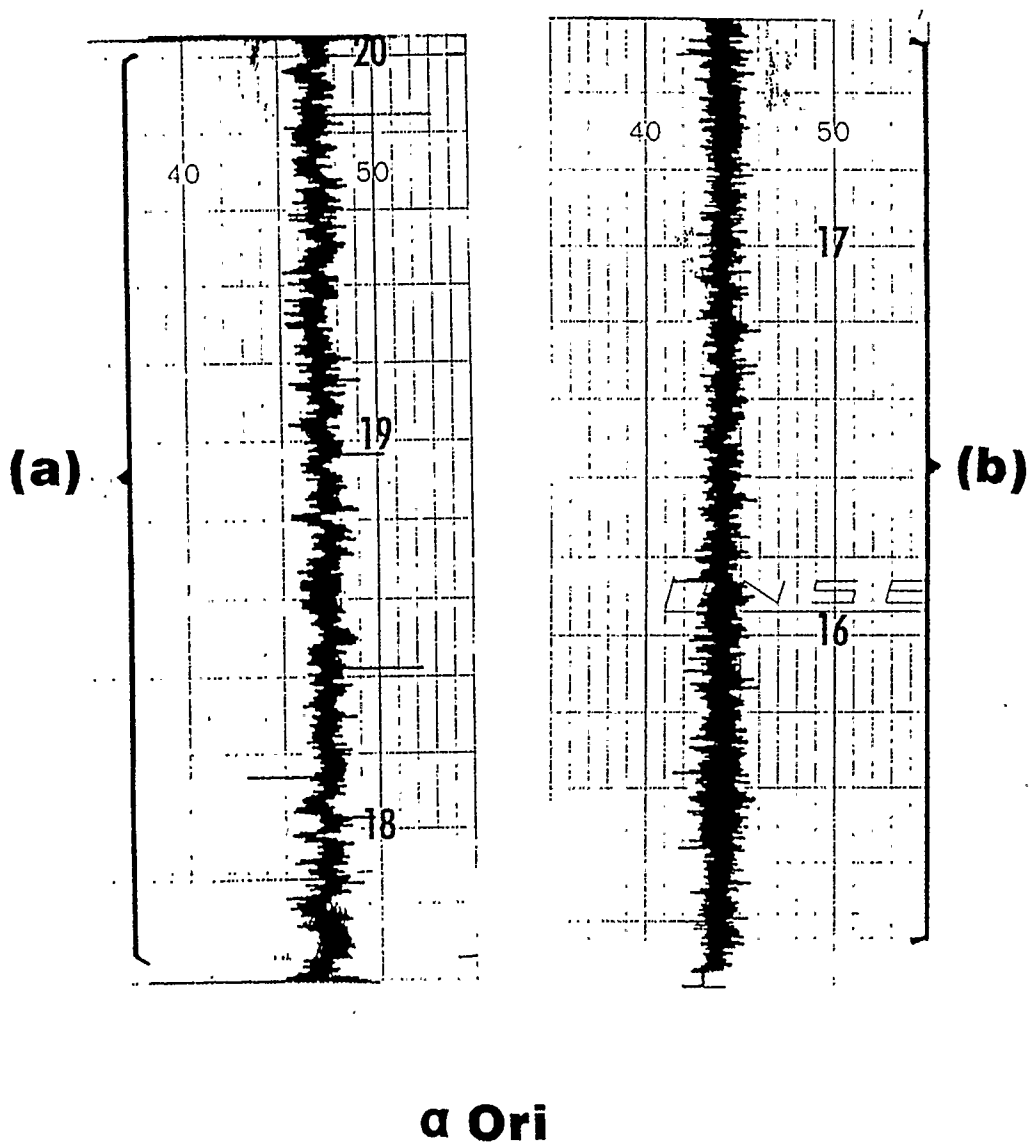


Figure 3.7: Chart recorder traces for  $\alpha$  Ori at 800 and  $1100\mu m$ : (a) Trace at  $800\mu m$  (SCAN081); 1mV scale; (b) Trace at  $1100\mu m$  (SCAN080); 1mV scale.

Table 3.2: Flux Conversion Factors.

Filter ( $\mu m$ )		February 7th	February 8th
	planet	Jupiter	Mars
	semi-diameter	18.07"	2.57"
1100	true flux $F_\lambda$ (Jy)	7772.09	193.62
800		16923.41	447.23
450		46089.35	1375.02
1100	$K$	3.157	1.025
800		2.527	1.023
450		2.527	1.023
1100	$f_{cal}$ (mV)	$84.5 \pm 0.2$	$5.02 \pm 0.02$
800		$113.2 \pm 0.5$	$5.51 \pm 0.01$
450		$48.3 \pm 0.4$	$0.42 \pm 0.01$
1100	airmass $x_{cal}$	1.081	2.713
800		1.085	1.862
450		1.089	1.817
1100	$F_{Jy/mV}$ ( $\frac{Jy}{mV}$ )	$22.1 \pm 0.8$	$28.2 \pm 5.3$
800		$30.1 \pm 3.9$	$36.5 \pm 2.3$
450		$113.1 \pm 39.5$	$137.6 \pm 23.4$

Two planets were used as calibrators in order to calibrate the observed fluxes. For the night of February 7th, Jupiter was used as the calibrator. Jupiter was observed to have a semi-diameter of 18.07". For the night of February 8th, Mars was used as the calibrator, with a semi-diameter of 2.57". The subsequent results can be seen in table 3.2.

The results of the calibrated fluxes per scan per object are shown in tables 3.3 to 3.11, where  $F_{s,i}$  is the flux for the scan  $i$ ,  $\sigma_{s,i}$  is the statistical error for scan  $i$ ,  $e_{c,i}$  is the systematic error for scan  $i$ , and  $x_i$  is the airmass for scan  $i$ . Scans 001 to 049 were done on February 7th, 1988, and scans 050 to 120 were done on February 8th, 1988. The flux of each object per scan was converted to Janskys using the

Table 3.3: Individual Scan Results for IK Tau.

	$\lambda$ ( $\mu m$ )	$F_{s,i}$ (Jy)	$\sigma_{s,i}$ (Jy)	$e_{c,i}$ (Jy)	$x_i$
SCAN019	1100	0.054	0.029	$1.279 \times 10^{-4}$	1.060
SCAN020	800	0.245	0.049	$1.035 \times 10^{-3}$	1.085
SCAN025	450	1.118	0.507	0.105	1.172
SCAN027	450	1.301	0.510	0.185	1.222
SCAN060	1100	0.110	0.209	$1.197 \times 10^{-2}$	1.133
SCAN061	800	0.245	0.111	$1.238 \times 10^{-2}$	1.172
SCAN063*	450	-0.367	4.265	0.214	1.255

Table 3.4: Individual Scan Results for TX Cam.

	$\lambda$ ( $\mu m$ )	$F_{s,i}$ (Jy)	$\sigma_{s,i}$ (Jy)	$e_{c,i}$ (Jy)	$x_i$
SCAN035	1100	0.029	0.019	$1.365 \times 10^{-3}$	1.363
SCAN036	800	0.141	0.099	$1.031 \times 10^{-2}$	1.398

relation

$$F_{s,i} = f_{mV,i} F_{(Jy/mV),j} e^{\alpha_j x_i} \quad (3.2)$$

where  $f_{mV,i}$  is the observed flux in millivolts for scan  $i$ ,  $F_{(Jy/mV),j}$  is the flux conversion factor for night  $j$ , where  $j = 7$  or  $8$ ,  $\alpha_j$  is the extinction coefficient for night  $j$ , and  $x_i$  is the airmass for scan  $i$ . The term  $e^{\alpha_j x_i}$  corrects for extinction at above-atmosphere. Scans with a star (\*) beside them indicate scans which were not used in the summing of the scans per waveband. This will be discussed further in the following chapter.



Table 3.5: Individual Scan Results for  $\alpha$  Ori.

	$\lambda$ ( $\mu m$ )	$F_{s,i}$ (Jy)	$\sigma_{s,i}$ (Jy)	$e_{c,i}$ (Jy)	$x_i$
SCAN080	1100	0.071	0.021	$5.130 \times 10^{-3}$	1.661
SCAN081	800	0.172	0.131	$7.939 \times 10^{-4}$	1.807

Table 3.6: Individual Scan Results for VY CMa.

	$\lambda$ ( $\mu m$ )	$F_{s,i}$ (Jy)	$\sigma_{s,i}$ (Jy)	$e_{c,i}$ (Jy)	$x_i$
SCAN039	1100	0.782	0.018	$1.420 \times 10^{-2}$	1.492
SCAN040	800	3.315	0.070	0.336	1.518
SCAN041	450	9.719	1.120	4.630	1.534
SCAN073	1100	0.869	0.026	$7.463 \times 10^{-2}$	1.471
SCAN074	800	2.311	0.276	$6.138 \times 10^{-2}$	1.501

Table 3.7: Individual Scan Results for CW Leo.

	$\lambda$ ( $\mu m$ )	$F_{s,i}$ (Jy)	$\sigma_{s,i}$ (Jy)	$e_{c,i}$ (Jy)	$x_i$
SCAN045	1100	1.604	0.127	$5.851 \times 10^{-3}$	1.015
SCAN066	1100	1.916	0.025	0.178	1.366
SCAN067	800	5.283	0.083	0.220	1.293
SCAN068	450	30.110	1.935	1.821	1.230
SCAN078	1100	1.912	0.025	0.223	1.023
SCAN079	800	5.934	0.073	0.368	1.016
SCAN100	1100	1.883	0.034	0.160	1.483
SCAN101	800	5.496	0.123	0.129	1.542
SCAN102	450	36.241	3.885	1.173	1.616
SCAN111	1100	1.912	0.038	$3.740 \times 10^{-2}$	2.437
SCAN112	800	5.938	0.215	0.317	2.592

Table 3.8: Individual Scan Results for RW LMi.

	$\lambda$ ( $\mu m$ )	$F_{s,i}$ (Jy)	$\sigma_{s,i}$ (Jy)	$e_{c,i}$ (Jy)	$x_i$
SCAN047	1100	0.157	0.032	$4.736 \times 10^{-4}$	1.034
SCAN048	800	0.797	0.107	$1.169 \times 10^{-2}$	1.025
SCAN085*	800	0.411	0.075	$2.537 \times 10^{-2}$	1.019
SCAN086*	1100	-0.044	0.047	$5.106 \times 10^{-3}$	1.023
SCAN096	800	0.767	0.051	$4.012 \times 10^{-2}$	1.148
SCAN097	450	4.157	1.939	0.266	1.188

Table 3.9: Individual Scan Results for W Hya.

	$\lambda$ ( $\mu m$ )	$F_{s,i}$ (Jy)	$\sigma_{s,i}$ (Jy)	$e_{c,i}$ (Jy)	$x_i$
SCAN108	1100	-0.004	0.035	$3.426 \times 10^{-4}$	1.504

### Error Analysis per Scan

Since the observing runs ran over two nights, there are two separate extinction coefficients  $\alpha_j$  for each waveband, where  $j = 7$  or  $8$  corresponding to the night of February 7th or 8th, respectively. There are two separate calibration planets, resulting in two separate calibration fluxes  $f_{cal,j}$  in millivolts and the corresponding calibration airmasses  $x_{cal,j}$ . The total error  $\Delta F_{s,i}$  per scan  $i$  is then determined using the relation

$$\begin{aligned} (\Delta F_{s,i})^2 = & \left( \frac{\partial F_{s,i}}{\partial f_{mV,i}} \Delta f_{mV,i} \right)^2 + \left( \frac{\partial F_{s,i}}{\partial \alpha_7} \Delta \alpha_7 \right)^2 + \left( \frac{\partial F_{s,i}}{\partial f_{cal,7}} \Delta f_{cal,7} \right)^2 \\ & + \left( \frac{\partial F_{s,i}}{\partial \alpha_8} \Delta \alpha_8 \right)^2 + \left( \frac{\partial F_{s,i}}{\partial f_{cal,8}} \Delta f_{cal,8} \right)^2 \end{aligned}$$

where

$$\begin{aligned} \frac{\partial F_{s,i}}{\partial f_{mV,i}} &= F_{(Jy/mV),j} e^{\alpha_j x_i} & j = 7 \text{ or } j = 8 \\ \frac{\partial F_{s,i}}{\partial \alpha_j} &= f_{mV,i} f_{DL,j} \frac{1}{f_{cal,j}} (x_i - x_{cal,j}) e^{\alpha_j (x_i - x_{cal,j})} \\ \frac{\partial F_{s,i}}{\partial f_{cal,j}} &= f_{mV,i} f_{DL,j} \left( \frac{-1}{f_{cal,j}^2} \right) e^{\alpha_j (x_i - x_{cal,j})}. \end{aligned}$$

The term  $f_{DL,j}$  is simply  $F_\lambda/K$  for the night of February 7th or 8th.

The statistical error per scan is the first term of the equation such that

$$\sigma_{s,i}^2 = \left( \frac{\partial F_{s,i}}{\partial f_{mV,i}} \Delta f_{mV,i} \right)^2.$$

The systematic error per scan corresponds to the sum of the squares of the error due to  $\alpha_j$  and  $f_{cal,j}$  such that

$$e_{c,i}^2 = \left( \frac{\partial F_{s,i}}{\partial \alpha_j} \Delta \alpha_j \right)^2 + \left( \frac{\partial F_{s,i}}{\partial f_{cal,j}} \Delta f_{cal,j} \right)^2,$$

Table 3.10: Individual Scan Results for M82.

	$\lambda$ ( $\mu m$ )	$F_{s,i}$ (Jy)	$\sigma_{s,i}$ (Jy)	$e_{c,i}$ (Jy)	$x_i$
SCAN049	800	2.203	0.917	0.241	1.553

Table 3.11: Individual Scan Results for Hb 12.

	$\lambda$ ( $\mu m$ )	$F_{s,i}$ (Jy)	$\sigma_{s,i}$ (Jy)	$e_{c,i}$ (Jy)	$x_i$
SCAN011	1100	0.072	0.028	$3.506 \times 10^{-3}$	2.186

where again  $j = 7$  or  $j = 8$  depending on the night of the scan observation.

### 3.3 Criteria for Source Selection

The data sources finally observed were chosen from a list of brightest *IRAS* sources in the  $12\mu m$  waveband. From this list, a sub-list of observable objects was made, given the location of the JCMT observatory and the dates and times of the observing nights. This final sub-list consisted of the objects with the julian dates of the observing nights, the hour angles (HA) of the objects, and the airmass at each hour of the observing run. Those objects whose airmasses indicated the object had set were crossed off the list of observable objects. The airmass  $x$  was found using the well-known relation,

$$\begin{aligned}
 x &= [\sin \beta]^{-1} \\
 &= [\sin(\delta) \sin(\phi) + \cos(\delta) \cos(\phi) \cos(HA)]^{-1},
 \end{aligned}$$

where  $\beta$  is the elevation of the object,  $\delta$  is the declination of the object,  $\phi$  is the latitude of the observatory (JCMT). From this final list, which indicated which stars were set or up, a tentative observing schedule was made. The closer the airmass was to a value of 1, the closer it was to the highest elevation in the sky. While at JCMT, the telescope limitations and the amount of observing time required per object further limited observations to the handful of objects presented in this thesis.

## Chapter 4

### Data Analysis and Modeling

#### 4.1 Star Descriptions

Most of the objects observed are late-type cool giants or supergiants. Five of the objects are M-type variable stars, and two are carbon stars. Table 4.1 gives a listing of the objects and some characteristics. The references for table 4.1 are as follows:

1. Chan and Kwok, 1988.
2. Rowan-Robinson *et al.* 1986.
3. Fazio *et al.* 1980.
4. Dyck *et al.* 1984.
5. Skinner and Whitmore, 1987.
6. Keady *et al.* 1988.
7. Werner, 1985.
8. Wehrse, 1987.
9. Pégourié, 1987.
10. Orofino *et al.* 1987.
11. Szymczak, 1987.
12. de Jager, 1980.
13. Rowan-Robinson and Harris, 1983a.
14. Hirschfeld and Simon (Eds. ), 1985.

Table 4.1: Characteristics of Observed Objects.

IRAS	$\alpha$ (1950), $\delta$ (1950)	Spectral Type	$T_{eff}$ (K)	Dist. (kpc)	Refs.
03507+1115	$\alpha = 03^h 50^m 43^s.5$ $\delta = 11^\circ 15' 29''$	M6e-10e	2560	0.27?	1, 4, 9, 13
04566+5606	$04^h 56 40.6,$ $56^\circ 06 28$	M8-9.5	2660	0.50?	1,9,13
05524+0723	$05^h 52 27.8,$ $07^\circ 23 58$	M2Iab	3600	0.18	2, 5, 9
07209-2540	$07^h 20 55.6,$ $-25^\circ 40 17$	M3-M5e I	2740	1.5?	1, 4, 7, 8, 12, 13
09452+1330	$09^h 45 14.2,$ $13^\circ 30 40$	C9,5	2300	0.29?	3, 4, 6, 10
09517+6954	$09^h 51 42.4$ $69^\circ 54 59$			3250	15
10131+3049	$10^h 13 10.7,$ $30^\circ 49 18$	C4,3	2700	0.19?	1, 4, 10
13462-2807	$13^h 46 12.5,$ $-28^\circ 07 11$	M7.5e-M9pe	3000	0.095	1, 11, 13, 14
23239+5754	$23^h 23 57.3$ $57^\circ 54 25$				

15. Jaffe *et al.* 1984.

The values with question marks (?) beside them indicate a discrepancy in values as recorded in differing references; these will be discussed in the descriptions of the individual objects. Table 4.2 lists the IRC and RAFGL associations as well as other associations for the objects.



Table 4.2: Object Associations.

<b>IRAS</b>	<b>RAFGL</b>	<b>IRC</b>	<b>Other Associations</b>
03507+1115	529	+10050	<b>IK Tau, NML Tau, JP11 5529</b>
04566+5606	664	+60150	<b>TX Cam</b>
05524+0723	836	+10100	<b><math>\alpha</math> Ori, EIC 108, Betelgeuse, HR 2061, FIRSSE 117, HD 39801, JP11 1282</b>
07209-2540	1111	-30087	<b>VY CMa, FIRSSE 204, HD 58061</b>
09452+1330	1381	+10216	<b>CW Leo, PK 221 +45.1</b>
09517+6954	1388		<b>M82, NGC 3034</b>
10131+3049	1403	+30219	<b>RW LMi, Cit 6</b>
13462-2807	1650	-30207	<b>W Hya, HD 120285, JP11 2429</b>
23239+5754			<b>Hb 12, PK 111 -2.1, VV 286</b>

### 4.1.1 M-Type Stars

#### $\alpha$ Ori

This late-type cool supergiant is better known as Betelgeuse. It is an oxygen-rich ( $\frac{O}{C} > 1$ ) star of spectral classification M2 Iab, (Rowan-Robinson *et al.* 1986).  $\alpha$  Ori is an extensively observed star, and its effective temperature, as determined by various sources, ranges between 3500 to 3900K. The *Sky Catalogue* 2000.0 (1985) classifies  $\alpha$  Ori as a semi-regular variable with a period of about 2110 days. The distance to the star has been estimated to be 0.18 kpc, (Pégourié, 1987). Betelgeuse has been modelled previously, most models suggesting there is an optically thin shell of silicate composition. The mass loss rate has been estimated to be  $\sim 5 \times 10^{-7} M_{\odot} yr^{-1}$ , with an outflow velocity of approximately  $15 \text{ km s}^{-1}$ , (Skinner and Whitmore, 1987). The radius of the star has been estimated at about  $6.5 \times 10^{13} \text{ cm}$ , (Pégourié, 1987). It has been suggested that  $\alpha$  Ori has a dust shell which begins fairly far from the star due to it being an early-M star, (Volk, 1986). Its luminosity has been estimated to be  $2.79 \times 10^{38} \text{ erg s}^{-1}$ , with an estimated star mass of  $\approx 20 M_{\odot}$ , (Strohmeier, 1972).

#### VY CMa

VY Canis Majoris, a strong emitter in the infrared and radio range, is a nebulous late-type cool red supergiant surrounded by circumstellar dust. VY CMa has a spectral classification of M3-M5e I, (de Jager, 1980). De Jager (1980) has described VY CMa as an irregular variable with an optically thick circumstellar shell; it may be surrounded by a small reflection nebula or extended dust clouds. (A reflection nebula has a continuous spectrum with the nebula generally being bluer than the

star.) Its effective temperature has been determined to be 2740K, (de Jager, 1980), with an estimated stellar luminosity of approximately  $3.5 \times 10^5 L_{\odot}$ , though Rowan-Robinson and Harris (1983a) estimate a luminosity of about  $6 \times 10^6 L_{\odot}$ . The approximate distance to VY CMa has been determined to be 1.5 kpc (de Jager, 1980; Bujarrabal *et al.* 1987), though Netzer *et al.* (1987) quotes a distance of 1.9 kpc. An estimated stellar mass of  $20 M_{\odot}$  was determined by de Jager (1980). Estimates of stellar mass loss rates range from  $1.2 \times 10^{-4} M_{\odot} yr^{-1}$  (Netzer *et al.* , 1987) to  $2.3 \times 10^{-4} M_{\odot} yr^{-1}$  (Dyck *et al.* , 1984), with outflow velocities of about 37 to 39  $km s^{-1}$ .

### IK Tau

IK Tauri is a late-type cool supergiant with an oxygen-rich envelope. Considered to be a Mira variable with a period of  $\sim 460$  days (Bujarrabal *et al.* 1987), its spectral classification is M6e-10e (Pegourie, 1987). The effective temperature, as quoted by Rowan-Robinson and Harris (1983a), is approximately 2560K. The distance to the star has been determined by various sources, and seems to differ from source to source: Szymczak (1987) quotes a distance of 0.24kpc; Netzer and Knapp (1987) quote a distance of 0.27kpc; Bujarrabal *et al.* (1987) quotes a distance of 0.4kpc; and, Pegourie (1987) quotes a distance of 0.52kpc. Pégourié (1987) also estimates the star's radius to be approximately  $13 \times 10^{13} cm$ . IK Tauri's mass loss rate has been estimated to be approximately  $4.2 \times 10^{-6} M_{\odot} yr^{-1}$ , with an outflow velocity of about  $18 km s^{-1}$  (Bedijn, 1987), although Netzer *et al.* quotes a velocity of  $\sim 16.7 km s^{-1}$ .

### TX Cam

TX Camelopardalis is a late-type cool giant of spectral classification M8-9.5 (Rowan-Robinson and Harris, 1983a). It is considered to be a Mira variable star rich in oxygen with a period of approximately 557 days (Bujarrabal *et al.* 1987). Pégourié (1987) suggested an effective temperature of approximately 2660K. He also quoted a distance to the star of about 0.5kpc, and a radius of about  $7.3 \times 10^{13}$  cm. Rowan-Robinson and Harris (1983) quote a distance to the star of 0.22kpc, while Bujarrabal *et al.* (1987) quote distances ranging from  $\sim 0.860$  kpc (from literature) to 1.158kpc (from calculation), so there seems to be some discrepancy.

### W Hya

W Hydrae is an oxygen-rich late-type cool giant. The *Sky Catalogue* 2000.0 (1985) classifies this star as a semi-regular variable with a period of about 397 days, and a spectral classification of M7.5e-M9pe. Rowan-Robinson and Harris (1983a) quote a distance to the star of 0.095kpc, while Szymczak (1987) quotes a distance of 0.10kpc. Bujarrabal *et al.* (1987) quote a distance to W Hya of approximately 0.285kpc. Treffers and Cohen (1973) suggested that silicate particles may possibly *not* be found extensively in the circumstellar envelope of W Hydrae.

## 4.1.2 Carbon Stars

### CW Leo

CW Leonis is a very extensively studied bright star. At  $5\mu m$ , CW Leo is the brightest object in the sky outside our solar system. Also known widely as IRC+10216, it is a carbon-rich Mira-type variable. The flux from CW Leo exhibits regular

variations in the infrared with a period of about 640 days, (Ridgeway *et al.*, 1987), similar to the long period variations of Miras. CW Leo is a late-type star with a spectral classification of C9,5 (Dyck *et al.* 1984). The total luminosity, as determined by Werner (1985), is about  $5 \times 10^4 L_{\odot}$ , with an approximate distance to the star of 290pc, (although Leahy *et al.* (1987) suggest that CW Leo may be as close as 150pc). In support of this, Keady *et al.* (1988) found a distance of 200pc to CW Leo. Mass loss rate estimates range from about  $2 \times 10^{-5} M_{\odot} \text{ yr}^{-1}$  (Keady *et al.* 1988) to  $4.9 \times 10^{-5} M_{\odot} \text{ yr}^{-1}$  (Wannier and Sahai, 1987). The effective temperature of CW Leo has been determined by various sources, and seems to range from 1500K (Bowers and Knapp, 1987) to approximately 2300K (Keady *et al.* 1988). An outflow velocity of  $\sim 14 \text{ km s}^{-1}$  has been determined (Keady *et al.* 1988).

CW Leo seems to fit the pattern of a central carbon star surrounded by an optically thick (opaque) envelope or shell. According to Keady *et al.* (1988), it is suggested that there are at least two different types of dust species in the envelope: (i) possibly a type of carbon soot, responsible for continuous emission and absorption from the ultraviolet to the infrared, (ii) silicon carbide (SiC), responsible for the  $11\mu\text{m}$  emission feature. The envelope is visible optically as an extended elliptical patch (Cohen, 1979). Ridgeway (1988) assumes amorphous carbon to be the main constituent, and SiC to be a minor constituent of the envelope composition. Treffers and Cohen (1974) determined a dust mass of the envelope to be  $\sim 4 \times 10^{-9} M_{\odot}$ . It was also previously suggested that the shell of CW Leo consists of two components: a hotter optically thick envelope of colour temperature  $\sim 600\text{K}$ , and an outer optically thin envelope of colour temperature  $\sim 375\text{K}$  (Cohen, 1978; McCarthy *et al.*, 1977). Cohen suggested that this outer cooler dust shell has a

radius of  $\sim 2 \times 10^{15}$  cm.

### RW LMi

Aside from CW Leo, cool giant RW Leonis Minoris is one of the most luminous optically-thick sources in the infrared. It is a carbon-rich semi-regular variable, with a spectral classification of C4,3 (Dyck *et al.*, 1984). (The *Sky Catalogue* 2000.0 (1985) classifies RW LMi as a Mira variable, while the General Catalogue of Variable Stars (GCVS) classifies it as a semi-regular variable.) The distance to the star is estimated at 190pc, (Dyck *et al.* 1984), though Rowan-Robinson and Harris (1983b) quote a distance of 400pc. Carbon stars of spectral class C4 are estimated to have effective temperatures of typically  $\sim 2700$ K, (de Jager, 1980). The mass loss rate has been estimated to be  $3.2 \times 10^{-6} M_{\odot} \text{ yr}^{-1}$ , with an outflow velocity of  $17 \text{ km s}^{-1}$ , (Dyck *et al.*, 1984).

### 4.1.3 Other Objects

#### M82

M82 is an irregular II galaxy,  $\sim 3.3$ Mpc away (Rodriguez *et al.* 1980; Jaffe *et al.* 1984). According to Simon *et al.* (1979) the nuclear region contains late-type stars, dusty H II regions, clusters of early-type stars, and compact non-thermal radio sources. In the infrared, the nucleus contains an extended  $10\mu\text{m}$  continuum source, thought to be thermal radiation from dust grains heated by stellar UV radiation (Simon *et al.* 1979). There has been observed a deep absorption band centred at  $9.7\mu\text{m}$ . A broad peak in the spectrum around  $11.3\mu\text{m}$  and a weaker peak around  $8.7\mu\text{m}$  have been observed (Gillet *et al.* 1975). The  $10\mu\text{m}$  feature

may be due to silicate dust (Gillet *et al.* 1975). According to Rieke *et al.* (1980), most of the luminosity of M82 emerges in the far-infrared, where they quote a total luminosity of  $3 \times 10^{10} L_{\odot}$ .

## Hb 12

Hb 12 is a compact planetary nebula with circumstellar dust emission, (Allen, 1974). Aitken *et al.*(1979) classify Hb 12 as an oxygen-rich planetary nebula, of  $\sim 2$  arcsec optical diameter, which exhibits features similar to those in the circumstellar shells of late-type oxygen-rich stars. The radio spectrum is observed to be optically thick below a wavelength of 1cm (Bignell, 1983).

## 4.2 Spectral Data

### 4.2.1 IRAS Observations

The Infrared Astronomical Satellite (IRAS) was launched in January of 1983. By November of 1983, it had successfully surveyed more than 96% of the sky in four wavelengths centered at 12, 25, 60 and  $100\mu m$ , (IRAS Explanatory Supplement, 1985). Results of the IRAS survey which are of interest in this thesis are found in the *IRAS* Point Source Catalogue (PSC) and the *IRAS* Low Resolution Spectra Catalogue (LRSC). The point source catalog (PSC) contains about 250 000 known point sources, including positions, flux densities and uncertainties. The Low Resolution Spectra Catalogue (LRSC) contains about 5400 point sources, bright in the  $8-22\mu m$  wavelength range, as detected by the low resolution spectrometer. Some of the point sources in the point source catalogue find their associated low-resolution spectra in the LRSC. The *IRAS* PSC observations used are presented in table 4.3.

Table 4.3: IRAS Flux Densities and LRS Classification

IRAS	Name	$F_\nu$ (Jy)				LRS
		$12\mu$	$25\mu$	$60\mu$	$100\mu$	
03507+1115	IK Tau	4630	2380	337	101	26
04566+5606	TX Cam	1640	635	136	37	27
05524+0723	$\alpha$ Ori	4680	1740	303	94	02
07209-2540	VY CMa	9920	6650	1470	327	24
09452+1330	CW Leo	47500	23100	5730	915	43
09517+6954	M82	53.2	274	1180	1140	81
10131+3049	RW LMi	3320	1220	277	84	04
13462-2807	W Hya	4200	1190	197	71	02
23239+6954	Hb 12	20.9	71.2	35.8	13	67



### 4.2.2 Submillimeter Observations

Submillimeter observations were obtained at the James Clerk Maxwell Telescope (JCMT) on the 4200m summit of Mauna Kea in Hawaii using the UKT 14 photometer. The UKT 14 is a millimeter/submillimeter continuum photometer. Using the 450micron matched band (450MB) filter, the 800MB filter, and the 1100MB filter wavebands, submillimeter observations were obtained for the objects described previously.

There were 120 scans done in total of the observed objects, including the calibrators. (A scan consisted of observing an object with one specified filter.) Using the flux conversion factors previously determined, the flux values observed for each scan was converted from millivolts to Janskys. These converted fluxes then were averaged for each filter for each object. For the sum of the scans, the mean flux per wavelength was found using the relation

$$\begin{aligned}\bar{F}_s &= \frac{1}{n} \sum_{i=1}^n F_{s,i} \\ &= \frac{1}{n} \sum_{i=1}^n f_{mV,i} f_{DL,j} \frac{1}{f_{cal,j}} e^{\alpha_j(x_i - x_{cal,j})}\end{aligned}\quad (4.1)$$

where  $j = 7$  or  $8$  corresponding to the nights of February 7th or 8th, respectively,  $n$  is the number of scans per wavelength specified,  $f_{DL,j} \equiv (F_\lambda/K)_j$ ,  $f_{mV,i}$  is the scan flux observation in millivolts for scan  $i$ ,  $\alpha_j$  is the extinction coefficient,  $f_{cal,j}$  is the calibration flux in millivolts,  $x_i$  is the observed airmass for scan  $i$ , and  $x_{cal,j}$  is the calibration airmass. Thus resulted, for most of the objects, a single value for observed flux at each of the 1100, 800, and 450 $\mu m$  filters, the results of which are given in table 4.4. Not all the scans were included in the summing procedure per object; scans which had converted flux values (in Janskys) which were  $3\sigma_{s,i}$  or

Table 4.4: Calibrated Submillimetre Flux Densities.

Object	IRAS	$F_{1100}(\text{Jy})$	$F_{800}(\text{Jy})$	$F_{450}(\text{Jy})$
IK Tau	03507+1115	$0.082 \pm 0.018$	$0.245 \pm 0.068$	$1.239 \pm 1.374$
TX Cam	04566+5606	$\leq 0.058$	$\leq 0.296$	—
$\alpha$ Ori	05524+0723	$0.071 \pm 0.022$	$\leq 0.392$	—
VY CMa	07209-2540	$0.826 \pm 0.038$	$2.813 \pm 0.422$	$9.719 \pm 4.763$
CW Leo	09452+1330	$1.845 \pm 0.110$	$5.662 \pm 0.420$	$33.180 \pm 3.775$
M82	09517+6954	—	$\leq 2.752$	—
RW LMi	10131+3049	$0.157 \pm 0.032$	$0.782 \pm 0.114$	$\leq 5.817$
W Hya	13462-2807	$\leq 0.105$	—	—
Hb 12	23239+5754	$\leq 0.084$	—	—

more away from the mean or had negative flux values which were approximately  $1\sigma_{s,i}$  in size were not included in the sum for the particular waveband in question. Not all objects had scans made at all wavebands. Upperlimits (designated in the table by  $\leq$ ) were set at  $3\bar{\sigma}_s$ , where  $\bar{\sigma}_s$  is the statistical error of the sum of the scans, as explained in the following section.

## Error Analysis

Statistical and systematic errors were calculated for the submillimetre observations.

The total error in  $\bar{F}_s$  was found using the relation

$$\begin{aligned}
 (\Delta \bar{F}_s)^2 &= \sum_{i=1}^n \left( \frac{\partial \bar{F}_s}{\partial f_{mV,i}} \Delta f_{mV,i} \right)^2 + \left( \frac{\partial \bar{F}_s}{\partial \alpha_7} \Delta \alpha_7 \right)^2 \\
 &+ \left( \frac{\partial \bar{F}_s}{\partial f_{cal,7}} \Delta f_{cal,7} \right)^2 + \left( \frac{\partial \bar{F}_s}{\partial \alpha_8} \Delta \alpha_8 \right)^2 + \left( \frac{\partial \bar{F}_s}{\partial f_{cal,8}} \Delta f_{cal,8} \right)^2 \quad (4.2)
 \end{aligned}$$

where

$$\begin{aligned}
 \frac{\partial \bar{F}_s}{\partial f_{mV,i}} &= \frac{1}{n} f_{DL,j} \frac{1}{f_{cal,j}} e^{\alpha_j(x_i - x_{cal,j})} = \frac{1}{n} \left( \frac{F_{s,i}}{f_{mV,i}} \right) \\
 \frac{\partial \bar{F}_s}{\partial \alpha_j} &= \frac{1}{n} f_{DL,j} \frac{1}{f_{cal,j}} \sum_{i=1}^n f_{mV,i} (x_i - x_{cal,j}) e^{\alpha_j(x_i - x_{cal,j})} \\
 \frac{\partial \bar{F}_s}{\partial f_{cal,j}} &= \frac{1}{n} f_{DL,j} \left( \frac{-1}{f_{cal,j}^2} \right) \sum_{i=1}^n f_{mV,i} e^{\alpha_j(x_i - x_{cal,j})},
 \end{aligned}$$

where again  $j = 7$  or  $j = 8$ . The statistical error term,  $\bar{\sigma}_s$ , which is used to calculate the upper limits such that an upper limit  $= 3\bar{\sigma}_s$ , is the first term of equation 4.2

$$\bar{\sigma}_s^2 = \frac{1}{n^2} \sum_{i=1}^n \left( \frac{F_{s,i}}{f_{mV,i}} \Delta f_{mV,i} \right)^2.$$

The remaining four terms in equation 4.2 are the systematic error components such that

$$\begin{aligned}
 e_{sys}^2 &= \left( \frac{\partial \bar{F}_s}{\partial \alpha_7} \Delta \alpha_7 \right)^2 + \left( \frac{\partial \bar{F}_s}{\partial f_{cal,7}} \Delta f_{cal,7} \right)^2 \\
 &+ \left( \frac{\partial \bar{F}_s}{\partial \alpha_8} \Delta \alpha_8 \right)^2 + \left( \frac{\partial \bar{F}_s}{\partial f_{cal,8}} \Delta f_{cal,8} \right)^2.
 \end{aligned}$$

The statistical and systematic errors are presented in table 4.5. The signal-to-noise ratio  $S/N$  is simply the flux  $\bar{F}_s$  divided by the statistical error  $\bar{\sigma}_s$ . A signal-to-noise ratio of less than 3 determined the criteria for an upper limit.

Table 4.5: The Statistical and Systematic Errors.

Name	$\lambda(\mu m)$	$\bar{F}_s$ (Jy)	$\bar{\sigma}_s$ (Jy)	$e_{syst}$ (Jy)	$\frac{S}{N}$	Scans
IK Tau	1100	0.082	0.018	$3.98 \times 10^{-3}$	4.55	2
	800	0.245	0.061	$3.01 \times 10^{-2}$	4.04	2
	450	1.2339	0.360	1.362	3.44	2
TX Cam	1100	0.029	0.019	$3.70 \times 10^{-4}$	1.52	1
	800	0.141	0.099	$1.03 \times 10^{-2}$	1.43	1
$\alpha$ Ori	1100	0.071	0.021	$5.13 \times 10^{-3}$	3.31	1
	800	0.172	0.131	$7.94 \times 10^{-4}$	1.32	1
VY CMa	1100	0.826	0.016	0.035	51.95	2
	800	2.813	0.142	0.398	19.77	2
	450	9.719	1.120	4.630	8.68	1
CW Leo	1100	1.845	0.028	0.106	65.47	5
	800	5.662	0.068	0.415	83.44	4
	450	33.180	2.170	3.089	15.29	2
RW LMi	1100	0.157	0.032	$4.74 \times 10^{-4}$	4.84	1
	800	0.782	0.059	$9.75 \times 10^{-2}$	13.20	2
	450	4.157	1.939	0.266	2.14	1
W Hya	1100	-0.004	0.035	$3.43 \times 10^{-4}$	-0.12	1
M82	800	2.203	0.917	0.241	2.40	1
Hb 12	1100	0.072	0.028	$3.43 \times 10^{-4}$	2.59	1

### 4.2.3 Cross-Referenced Observations

Using the NASA Reference Publications 1196 (December 1987) and the Nasa Reference Publications 1182 (April 1987), other observations for the stars at various wavelengths were found. In table 4.6 to table 4.9 are listed the data observed in magnitudes at specific well-known wavelength bands. In tables 4.10 to 4.15 are listed the various wavelengths and corresponding observed fluxes measured for each specific object, though not every object had usable observations. The reference numbers as quoted can be found in the bibliography at the end of this thesis.

Table 4.6: Magnitude Observations.

Observations at wavelength bands J, H, K, L, M, N, Q. (References are: [1]-[800213]; [2]-[760302]; [3]-[830610]; [4]-[730002]; [5]-[831123]; [6]-[831007]; [7]-[850808]; [8]-[691201]; [9]-[841213]; [10]-[721103]; [11]-[721002]; [12]-[670402]; [13]-[700302]; [14]-[790101]; [15]-[710403]; [16]-[821005]; [17]-[740708]; [18]-[741009]; [19]-[760901]; [20]-[680902]; [21]-[790306]; [22]-[721203]; [32]-[690001].)

Star	J (1.25 $\mu$ )	H (1.65 $\mu$ )	K (2.2 $\mu$ )	L (3.4 $\mu$ )	M (5.0 $\mu$ )	N (10.2 $\mu$ )	Q (20 $\mu$ )
IK Tau	1.00 [1]	-0.2 [1]	-1.24 [2]	-2.20 [1]	-2.90 [1]	-5.2 [1]	-5.5 [3]
TK Cam	1.7 [1]	0.6 [1]	-0.3 [1]	-1.3 [1]	-1.7 [1]	-3.8 [1]	-5.0 [3]
$\alpha$ Ori	-3.55 [4]	-4.07 [4]	-4.17 [4]	-4.45 [4]	-4.17 [4]	-5.05 [4]	-5.7 [5]
VY CMa	1.8 [1]	0.5 [1]	-0.8 [1]	-2.52 [6]	-3.6 [1]	-6.2 [1]	-7.50 [7]
CW Leo	6.55 [8]	2.94 [8]	-0.6 [8]	-3.44 [8]	-5.0 [8]	-7.3 [10]	-9.1 [8]
M82	-	9.5 [20]	6.5 [21]	-	-4.4 [10]	-	-8.03 [11]
RW LMi	5.25 [12]	3.9 [1]	-1.8 [10]	-2.1 [9]	-4.59 [15]	-4.5 [13]	-5.4 [3]
W Hya	-1.6 [14]	-2.6 [14]	-3.1 [14]	-3.8 [14]	-4.29 [15]	-5.0 [14]	-5.76 [16]
Hb 12	-	9.9 [17]	8.8 [17]	6.4 [17]	3.1 [17]	0.7 [18]	-2.0 [19]

Table 4.7: Magnitude Observations

Magnitude observations at other well-known wavelengths. (References are as in the previous table, with the following additions: [23]-[850511]; [24]-[770608]; [25]-[801206]; [26]-[780509]; [27]-[740906]; [28]-[730304]; [29]-[761006]; [30]-[730303]; [31]-[840106]; [33]-[800103]; [34]-[700803]; [35]-[700402]. )

Star	1.04 $\mu$	8.7 $\mu$	11.6 $\mu$	12.5 $\mu$	18 $\mu$	30 $\mu$
IK Tau	1.80 [23]	-4.50 [1]	-5.0 [24]	-5.2 [1]	-5.9 [1]	-
TX Cam	2.44 [23]	-2.9 [1]	-4.1 [3]	-3.7 [1]	-4.6 [1]	-4.7 [3]
$\alpha$ Ori	-2.68 [25]	-4.7 [4]	-5.5 [22]	-5.40 [5]	-5.6 [30]	-5.9 [5]
VY CMa	2.96 [26]	5.3 [1]	-6.15 [6]	-6.3 [1]	-6.1 [1]	-7.25 [7]
CW Leo	8.04 [23]	-7.5 [24]	-7.52 [31]	-8.0 [33]	-8.7 [1]	-8.9 [3]
	10.08 [34]	-6.60 [10]		-7.6 [10]		
M82	-	-	-0.80 [3]	-	-	-4.2 [3]
RW LMi	6.41 [35]	-4.18 [31]	-5.4 [22]	-4.5 [10]	-5.3 [1]	-
	7.46 [27]		-4.85 [31]		-4.6 [10]	
W Hya	-1.12 [28]	-4.20 [29]	-5.08 [29]	-	-	$\sim$ 6.0 [16]
Hb 12	-	1.2 [18]	0.35 [18]	0.45 [18]	-1.5 [18]	-

Table 4.8: UBVRI Observations for  $\alpha$  Ori.

Magnitude observations in the UBVRI wavebands as obtained from the *Bright Star Catalogue*. The wavebands are as follows: U=  $0.365\mu\text{m}$ , B=  $0.44\mu\text{m}$ , V=  $0.55\mu\text{m}$ , R=  $0.70\mu\text{m}$ , I=  $0.90\mu\text{m}$ .

$\alpha$ Ori	V	B-V	U-B	R-I
	0.50	+1.85	+2.06	+1.28

Table 4.9: GCVS Observations.

Observations as recorded in the General Catalogue of Variable Stars (GCVS). The wavebands as quoted are V=  $0.55\mu\text{m}$ , B=  $0.44\mu\text{m}$ , P=  $0.43\mu\text{m}$ , and R=  $0.70\mu\text{m}$ .

Name	Variable Type	Waveband	Magnitude		Galactic Coord.	
			Max.	Min.	L	B
IK Tau	M	V	10.8	16.5	177.96	-31.41
TX Cam	M	B	11.6	17.7	152.84	+8.57
$\alpha$ Ori	SRc	V	0.0	1.3	199.79	-8.96
VY CMa	-	V	6.5	9.6	239.35	-5.06
CW Leo	M	R	10.96	14.8	221.45	+45.66
RW LMi	SRa	V	12.8	16.5	197.71	+55.97
W Hya	SRa	P	7.7	11.6	318.02	+32.81



Table 4.10: CW Leo Observations.

Wavelength ( $\mu m$ )	Flux (Jy)	Reference
21	23500	850209
34	12600	730805
36	9772	850209
42	6400	850209
53	5040	760906
61	3700	Fazio <i>et al.</i> 1980
73	2400	850209
135	600	850209
175	880	760609
350	107	760609
377	35.2	821215
400	32	Sahai <i>et al.</i> 1988
450	28.8	850209
811	9.77	850209
900	8.91	850209
1000	4.0	760906
1136	3.5	821215
1400	0.5	Sahai <i>et al.</i> 1988
3300	0.145	Sahai <i>et al.</i> 1988

Table 4.11: TX Cam Observations.

Wavelength ( $\mu m$ )	Flux (Jy)	Reference
20	1060	830201
27	608	830201
93	19	830201

Table 4.12:  $\alpha$  Ori Observations.

Wavelength ( $\mu m$ )	Flux (Jy)	Reference
7.46	5838	860422
20	2722	830201
27	1141	830201
33	734	780101
34	650	750701
40	444	830201
93	243	830201
400	4.0	Skinner <i>et al.</i> 1987

Table 4.13: VY CMa Observations.

Wavelength ( $\mu m$ )	Flux (Jy)	Reference
20	9393	830201
27	7260	830201
40	6650	830201
93	1406	830201
400	10	Sahai <i>et al.</i> 1988

Table 4.14: Hb 12 Observations.

Wavelength ( $\mu m$ )	Flux (Jy)	Reference
1.65	0.200	730606
2.2	0.310	730606
3.5	0.830	730606

Table 4.15: M82 Observations.

Wavelength ( $\mu m$ )	Flux (Jy)	Reference
1.25	0.056	800504
1.6	0.252	800504
2.2	0.350	800504
3.6	0.330	800504
5.0	8.4	720901
10.4	1.43	800504
10.6	6.4	800504
17.7	12	800504
19	17	800504
21	24	800504
22	29	800504
26	52	800504
40	625	850913
41	625	800108
47	920	850913
50	997.0	841001
58	1066	800108
65	1060	850913
78	1255	800108
95	990	850913
130	670	850913
141	630	800108
160	380	850913
400	30	841016

### 4.3 Expectations for the Circumstellar Dust Envelope in the Submillimetre Range

The main assumption we have made in the submillimetre wavelength range of the circumstellar dust shell is that the circumstellar shell is optically thin. The dust temperature profile is determined by radiative processes, since we are assuming collisional processes to be negligible. The equilibrium dust temperature is determined from the balance of radiative heating from the star and thermal emission from the grain. For stars embedded in circumstellar dust envelopes, the energy equation for thermal balance is based on the assumption that the dust envelope is heated by a star of temperature  $T_*$ ,

$$\begin{aligned} \text{Heating} &= \text{Cooling} \\ \frac{1}{4} \left( \frac{R_*}{r} \right)^2 \int_0^\infty \pi a^2 Q_\nu B_\nu(T_*) d\nu &= \int_0^\infty \pi a^2 Q_\nu B_\nu(T_D(r)) d\nu \end{aligned} \quad (4.3)$$

where  $\pi a^2 Q_\nu$  is the dust absorption cross-section, and

$$\begin{aligned} B_\nu(T_*) &= \frac{2h\nu^3}{c^2} \frac{1}{e^{h\nu/kT_*} - 1} \\ B_\nu(T_D(r)) &= \frac{2h\nu^3}{c^2} \frac{1}{e^{h\nu/kT_D} - 1} \end{aligned}$$

The dilution factor  $W = \frac{1}{4} \left( \frac{R_*}{r} \right)^2$  is equal to the solid angle subtended by the star to the total solid angle,  $4\pi$ , and  $T_D(r)$  is the dust temperature at  $r$ . From Mie theory, the efficiency factor  $Q_\nu$  can be determined. For stellar photons, where generally  $\lambda \ll a$ , the grain radius, the opacity efficiency factor is of the form  $Q_\nu \sim 1$ . In the far IR/submillimetre region of the spectrum, where  $\lambda \gg a$ , the efficiency factor has the form  $Q_\nu \propto \nu^\gamma$ .

Integrating the energy equation, we then have

$$\begin{aligned} \frac{1}{4} \left( \frac{R_*}{r} \right)^2 \int_0^\infty \pi a^2 \left( \frac{2h\nu^3}{c^2} \frac{1}{e^{h\nu/kT_*} - 1} \right) d\nu &\propto \int_0^\infty \pi a^2 \nu^\gamma \left( \frac{2h\nu^3}{c^2} \frac{1}{e^{h\nu/kT_D(r)} - 1} \right) d\nu \\ \left( \frac{R_*}{r} \right)^2 T_*^4 \int_0^\infty \frac{y^3}{e^y - 1} dy &\propto T_D(r)^{4+\gamma} \int_0^\infty \frac{x^{3+\gamma}}{e^x - 1} dx \end{aligned}$$

where we have dropped the irrelevant constants and made the variable transformations of  $x = \frac{h\nu}{kT_D(r)}$  and  $y = \frac{h\nu}{kT_*}$ . The integrals can be found in integral tables such that

$$\int_0^\infty \frac{x^{n-1}}{e^x - 1} dx = \Gamma(n) \left( \frac{1}{1^n} + \frac{1}{2^n} + \frac{1}{3^n} + \dots \right)$$

Thus, we have the following relation for the optically thin dust envelope,

$$\begin{aligned} \left( \frac{R_*}{r} \right)^2 T_*^4 &\propto T_D(r)^{4+\gamma} \\ T_D(r) &\propto r^{-\frac{2}{4+\gamma}}. \end{aligned} \quad (4.4)$$

At large wavelengths, such as in the submillimetre range, the optically thin assumption means that the dust grains become inefficient radiators, meaning that a dust grain is essentially being heated by the star and not by surrounding dust grains. The emergent flux then follows from the relation

$$dF_\nu = \frac{\epsilon_\nu \rho dV}{4\pi D^2}$$

where the volume emissivity is  $j_\nu = \frac{\epsilon_\nu \rho}{4\pi}$ , and  $D$  is the distance to the star. Thus, for optically thin media,

$$F_\nu = \frac{1}{D^2} \int j_\nu dV.$$

Since the volume element  $dV = dA dr = r^2 d\Omega dr$  and we are assuming the flux to be symmetric about  $\phi$  and  $\theta$  (isotropic), then  $\int_{sphere} d\Omega = 4\pi$ . The relation for

emergent flux becomes

$$F_\nu = \frac{1}{D^2} \int j_\nu 4\pi r^2 dr.$$

The emission coefficient, following Kirchoff's law for thermal emission, is simply

$$\begin{aligned} j_\nu &= \kappa_\nu B_\nu(T) \\ &= n_d(r) \pi a^2 Q_\nu B_\nu(T_D(r)), \end{aligned}$$

where  $n_d(r)$  is the number density on the grains, which is assumed to have an inverse square dependence on  $r$  such that  $n_d(r) \propto r^{-n}$  with  $n = 2$ . Thus, the emergent flux is

$$\begin{aligned} F_\nu &= \frac{1}{D^2} \int_{r_{in}}^{\infty} \pi a^2 Q_\nu B_\nu(T_D(r)) n_d(r) 4\pi r^2 dr \\ &\propto \frac{1}{D^2} \int_{r_{in}}^{\infty} \pi a^2 Q_\nu \left( \frac{2h\nu^3}{c^2} \frac{1}{e^{h\nu/kT_D(r)} - 1} \right) r^{-n} 4\pi r^2 dr \end{aligned} \quad (4.5)$$

where  $r_{in}$  is the inner radius (dust condensation radius) of the shell.

Since we found  $T_D(r) \propto r^{-\frac{2}{4+\gamma}}$ , we can write this in the form

$$T_D(r) = T_o \left( \frac{r}{r_o} \right)^{-\frac{2}{4+\gamma}}$$

where  $T_o$  and  $r_o$  are constants. Substituting this into equation 4.5 and defining a dummy variable  $x = \frac{h\nu}{kT_o} \left( \frac{r}{r_o} \right)^{\frac{2}{4+\gamma}}$ , we find

$$F_\nu \propto \nu^{\frac{2+\gamma}{2} + \frac{(n-2)(4+\gamma)}{2}} \int_{x_o}^{\infty} \frac{x^{\frac{2+\gamma}{2} - \frac{(n-2)(4+\gamma)}{2}}}{e^x - 1} dx. \quad (4.6)$$

Thus the emergent flux of the optically thin shell, in the limit as  $x_o \rightarrow 0$ , follows the relation

$$F_\nu \propto \nu^{\frac{2+\gamma}{2} + \frac{(n-2)(4+\gamma)}{2}}.$$

For a number density profile of  $n_d \propto r^{-2}$ , this translates to an expected emergent spectrum of

$$\begin{aligned} \nu F_\nu &\propto \nu^{\frac{2+\gamma}{2}+1} \\ \text{or} \\ \lambda F_\lambda &\propto \lambda^{-\left(\frac{2+\gamma}{2}+1\right)}. \end{aligned}$$

For a constant mass loss rate  $\dot{M}$  and stellar wind velocity  $v$  (assumed here to be of the order of  $\sim 10 \text{ km s}^{-1}$ ), the density profile  $\rho(r)$  of the circumstellar envelope can be obtained from the continuity equation such that

$$\dot{M} = 4\pi r^2 v \rho(r).$$

The dust and gas in the shell are assumed to be uniformly mixed, so that the dust mass loss rate is given by

$$\dot{M}_d = \frac{A y f}{\mu} \dot{M} = \chi \dot{M} \quad (4.7)$$

where here  $\mu$  is the mean atomic weight of the gas per hydrogen atom,  $A$  is the molecular weight of the grain material,  $y$  is the cosmic abundance of the least abundant element in the grain, and  $f$  is the fraction of that element in solid form. For both the silicate dust shell and the silicon carbide dust shell,  $\mu = 1.3$  and  $f = 1$  (complete condensation) is assumed. The remaining values are as quoted in chapter 2, section 2.1.2. For silicate dust, the computed ratio is  $\chi_{\text{silicate}} \simeq 4.31 \times 10^{-3}$ ; for silicon carbide dust,  $\chi_{\text{SiC}} \simeq 1.23 \times 10^{-3}$ .

The optical depth  $\tau$  of the circumstellar envelope at some reference wavelength  $\lambda_o$  is

$$\tau_{\lambda_o} = \int_{r_i}^{\infty} \kappa_{\lambda_o} dr$$

$$= \int_{r_i}^{\infty} \pi a^2 Q_{\lambda_o} n_d(r) dr \quad (4.8)$$

where, as before,  $n_d(r)$  is the number density of the dust grains. Assuming a constant mass loss rate, we find that

$$\begin{aligned} n_d(r) &= \frac{\dot{M}_d}{4\pi r^2 v m_d} \\ &= \frac{\chi \dot{M}}{4\pi r^2 v (\frac{4}{3}\pi a^3 \rho_s)} = \frac{\chi \dot{M}}{\frac{16\pi^2}{3} \rho_s a^3 v r^2} \end{aligned} \quad (4.9)$$

where  $\rho_s$  is the specific density of a single grain. For both silicate and silicon carbide,  $\rho_s \sim 3 \text{ g cm}^{-3}$ .

Substituting equation 4.9 into equation 4.8, and solving for  $\dot{M}$ , we find the mass loss rate of the CSE has the form

$$\dot{M} = C v r_i \tau_{\lambda_o} \quad (4.10)$$

where

$$C = \left(\frac{16\pi}{3}\right) \left(\frac{\rho_s}{\chi}\right) \left(\frac{a}{Q_{\lambda_o}}\right).$$

For astronomical silicate dust, the parameter  $\frac{Q_{\lambda_o}}{a}$  is  $\sim 1.3 \mu\text{m}^{-1}$  at the reference wavelength of  $\lambda_o = 9.7 \mu\text{m}$  (Draine, 1985). For silicon carbide dust,  $\frac{Q_{\lambda_o}}{a}$  is  $\sim 3.32 \mu\text{m}^{-1}$  at  $\lambda_o = 11.3 \mu\text{m}$  (Borghesi *et al.* 1985). Using equation 4.10 along with the results of the models, we can estimate the mass loss rates for our stars. These will be presented in the following section.

For silicate dust in the submillimetre range we have assumed an opacity dependence of  $\nu^{1.5}$  or  $\lambda^{-1.5}$ , thus  $\gamma = 1.5$ . Thus for silicate dust the expected dust temperature profile is  $T_D(r) \propto r^{-0.36}$ , while the expected emergent flux spectrum is  $\nu F_\nu \propto \nu^{2.75}$  or  $\lambda F_\lambda \propto \lambda^{-2.75}$ .



Table 4.16: Expected Versus Observed Submillimetre Fluxes.

The extrapolated fluxes at  $1100\mu m$ , based on the IRAS  $100\mu m$  fluxes, as compared to the observed fluxes at  $1100\mu m$ .

Name	$F_{100\mu m}$ (Jy)	Expected $F_{1100\mu m}$ (Jy)	Observed $F_{1100\mu m}$ (Jy)
IK Tau	101	0.46	$0.082 \pm 0.018$
TX Cam	37	0.17	$\leq 0.058$
$\alpha$ Ori	94	0.43	$0.071 \pm 0.022$
VY CMa	327	1.48	$0.826 \pm 0.038$
CW Leo	915	7.56	$1.845 \pm 0.110$
RW LMi	84	0.69	$0.157 \pm 0.032$
W Hya	71	0.32	$\leq 0.105$

For silicon carbide dust (SiC) in the submillimetre range we have assumed an opacity dependence of  $\nu^1$  or  $\lambda^{-1}$ , thus  $\gamma = 1$ . So, for silicon carbide dust, the expected dust temperature profile is  $T_D(r) \propto r^{-0.4}$ , while the expected emergent flux spectrum is  $\nu F_\nu \propto \nu^{2.5}$  or  $\lambda F_\lambda \propto \lambda^{-2.5}$ .

Based on the *IRAS* flux densities as recorded in table 4.3, the expected submillimetre flux densities at the  $1100\mu m$  waveband, using the  $\lambda F_\lambda \propto \lambda^{-(\frac{2+\gamma}{2}+1)}$  relation, were extrapolated. These are presented in table 4.16. The observed flux densities are consistently less than the expected flux densities.

#### 4.4 Fitting Procedures - Model Parameters and Results

The fitting procedures consisted of fitting model spectra generated by the DUSTCD code developed by Leung (1975, 1976), as discussed in chapter 3, to the spectral observations. The DUSTCD models were generated on the University of Calgary Cyber 205 supercomputer with the Cyber 860 *NOS/VE* system as the front end. Depending on the number of iterations needed, a typical model could be generated in approximately 60 to 300 CPU seconds. The model spectra were then fitted to the actual observations of the objects. The input parameters which differed from object to object, being dependent on the object itself, were the effective stellar temperature  $T_*$  (K), and the stellar luminosity  $L_*$  ( $L_\odot$ ). Most of these parameters were found through literary references for each star. In cases where certain parameters could not be found in literature, estimates based on spectral type were made. The adjustable input parameters were the optical depth  $\tau_{\lambda_o}$ , the effective temperature  $T_*$ (K), the effective luminosity  $L_*(L_\odot)$ , and the outer radius of the shell  $R_{out}$  (pc), which in effect was the adjustment for inner shell radius  $R_{in}$  since  $R_{in} = 4 \times 10^{-3} R_{out}$ . The dust condensation radius of the shell is the inner radius  $R_{in}$  of the shell, since there is dust from  $R_{in}$  to  $R_{out}$ . The condensation temperature of the dust was assumed to be  $\sim 1500K$ . Thus at  $R_{in}$ , which is the first radial grid point of the shell, the dust temperature  $T_D$ (K) was assumed to be the condensation temperature  $T_c$ (K) of the dust. The condensation temperature  $T_c$  (K) was kept to values of  $\sim 1500K$  for both the carbon-rich and oxygen-rich stars. The dust temperature distribution was expected to be  $T_D \propto r^{-\frac{2}{4+\tau}}$ ; sample plots of the dust temperature  $T_D$  against the relative shell radius from the models is shown in

figures 4.1 and 4.2. In the outer edges of the shell toward  $R_{out}$ , where we expect there to be less dust, the slope from the oxygen star is  $T_D \propto r^{-0.36}$ , while for the carbon star  $T_D \propto r^{-0.4}$ . This is consistent with our expectations for an optically thin region.

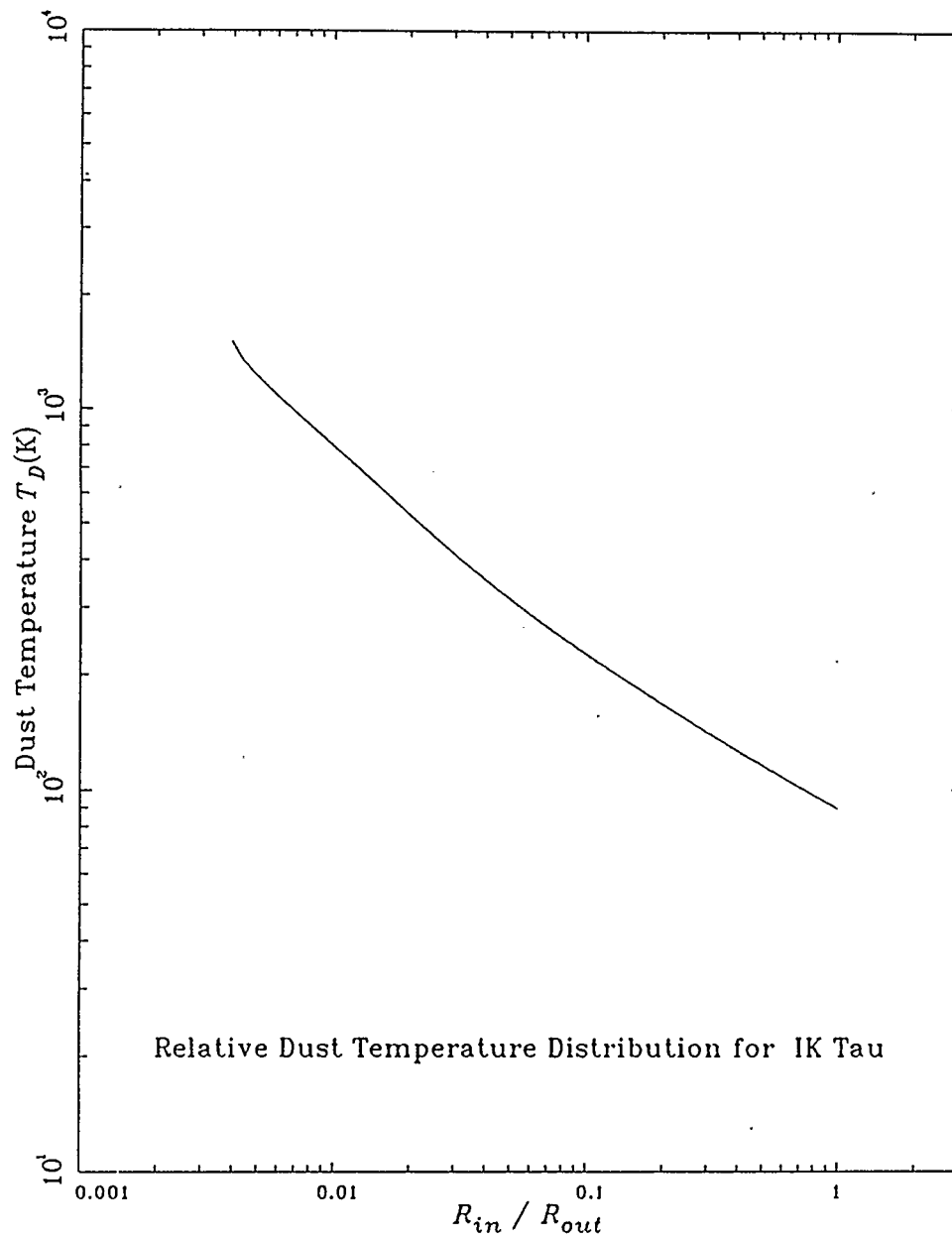


Figure 4.1: Dust temperature distribution as a function of relative shell radius for silicate dust with an opacity function dependence of  $\lambda^{-1.5}$ .

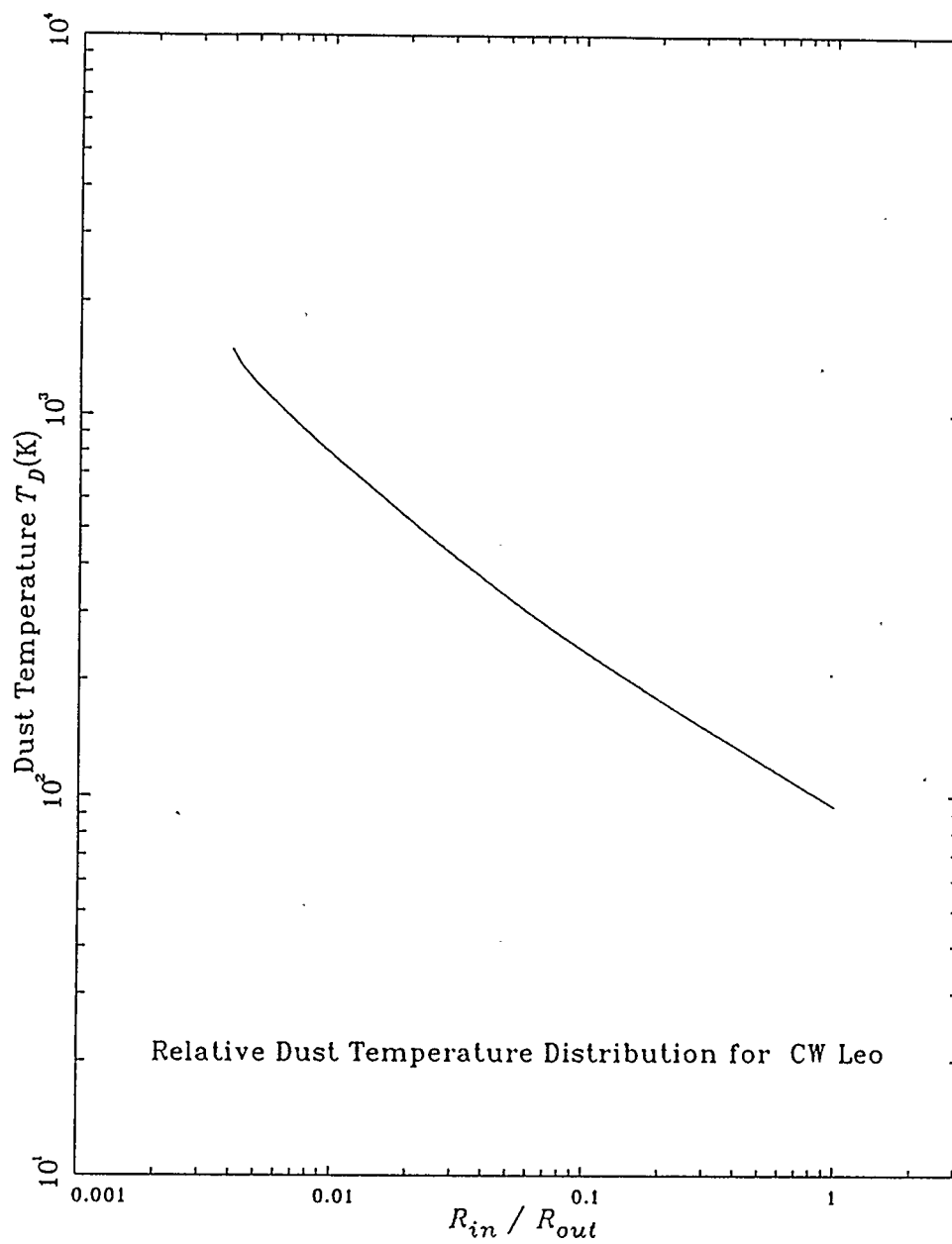


Figure 4.2: Dust temperature distribution as a function of relative shell radius for silicon carbide (SiC) dust with an opacity function dependence of  $\lambda^{-1}$ .

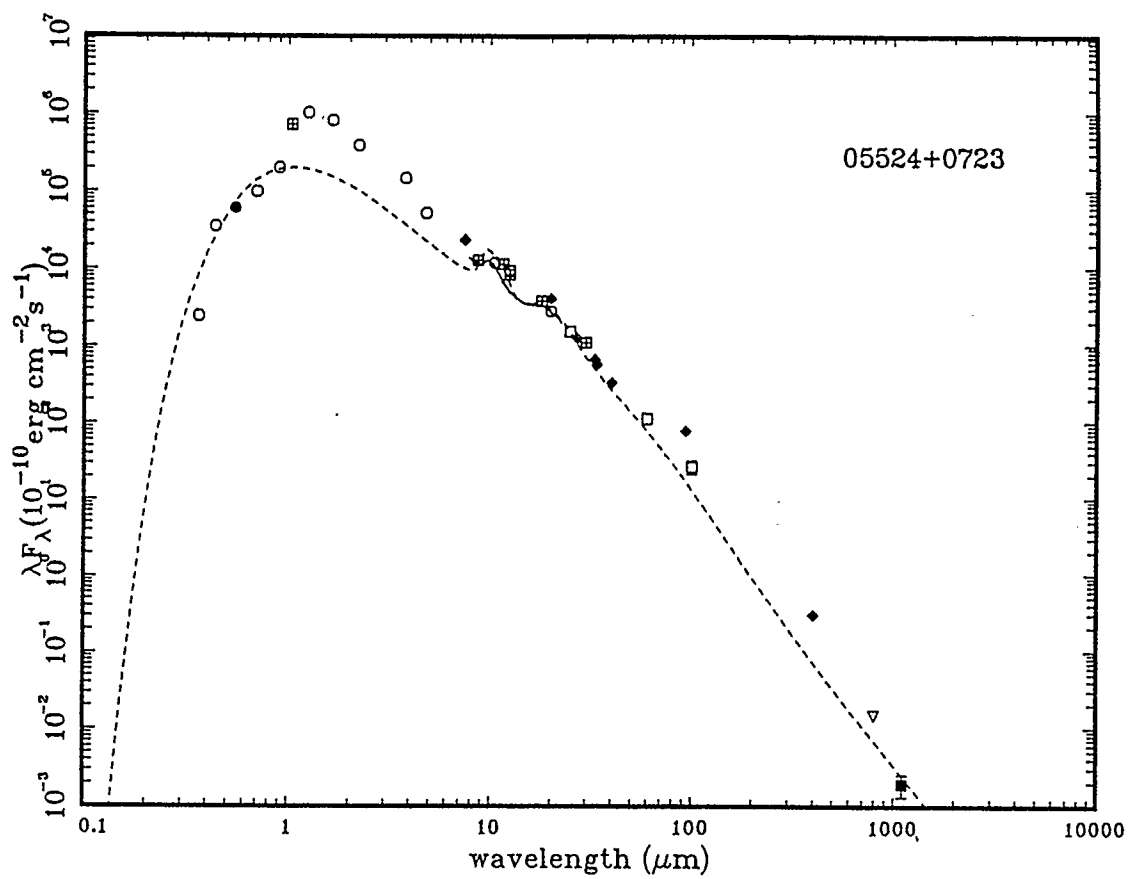
The outer shell radius  $R_{out}$  was the parameter used to maintain the condensation temperature at the desired result. In order to estimate  $R_{out}$  to maintain the assumed condensation temperature of  $T_c \sim 1500K$ , the relation  $R_{out}^2 T_D^4 = R_{out,1500K}^2 T_{D,1500K}^4$  was used, where  $R_{out}$  and  $T_D$  are the output results of the most recent model,  $T_{D,1500K}$  is the assumed dust condensation temperature of  $1500K$ , and  $R_{out,1500K}$  is the resultant input radius for the next model run. The flux models were then plotted along with observed data, where a distance  $D$  (kpc) to the object was estimated. The distance to the star was estimated using the total flux derived in the model and the input effective luminosity parameter in the relation

$$D = \left( \frac{L_*}{4\pi F_{total}} \right)^{\frac{1}{2}}.$$

In the subsequent plotted results, the open circles designate the *UBVRI* and *JHKLMNQ* magnitude data with the filled circles generally designating the minimum (or lower) magnitudes at these wavebands; the crossed boxes designate the magnitude observations at each of  $1.04, 8.7, 11.6, 12.5, 18$  and  $30\mu m$ ; the crossed diamonds designate the remaining cross referenced observations in Janskys (Jy). The *IRAS* infrared observations are designated by the open boxes, while the JCMT submillimetre observations are designated by the filled boxes. Upper limits are denoted by the inverted triangles. The solid line represents the LRS spectra. The dashed line represents the modeled flux curve. Results of the final model fitting parameters are presented in tables 4.17 and 4.18. Discussions of the results will be presented in chapter 5.

Table 4.17: Model Results for the Oxygen-Rich Stars.  
 Final model fitting parameters of the oxygen-rich M-type stars.

Name	IK Tau	TX Cam	$\alpha$ Ori	VY CMa	W Hya
$\tau_{9.7\mu m}$	0.79	0.82	0.04	1.60	0.04
$T_*$ ( $10^3 K$ )	2.56	2.76	3.60	2.74	3.00
$L_*$ ( $10^3 L_\odot$ )	6.2	6.2	30	350	8.2
$R_{in}$ ( $10^{14} cm$ )	0.85	0.92	2.31	7.17	1.06
$F_{tot}$ ( $10^{-10} erg s^{-1} cm^{-2}$ )	5.5	1.6	29.6	9.1	26.2
$D$ (kpc)	0.19	0.35	0.18	1.11	0.10
$\dot{M}$ ( $10^{-6} M_\odot yr^{-1}$ )	1.63	1.07	0.20	62.2	0.06

Figure 4.3: The model fit for  $\alpha$  Orionis.



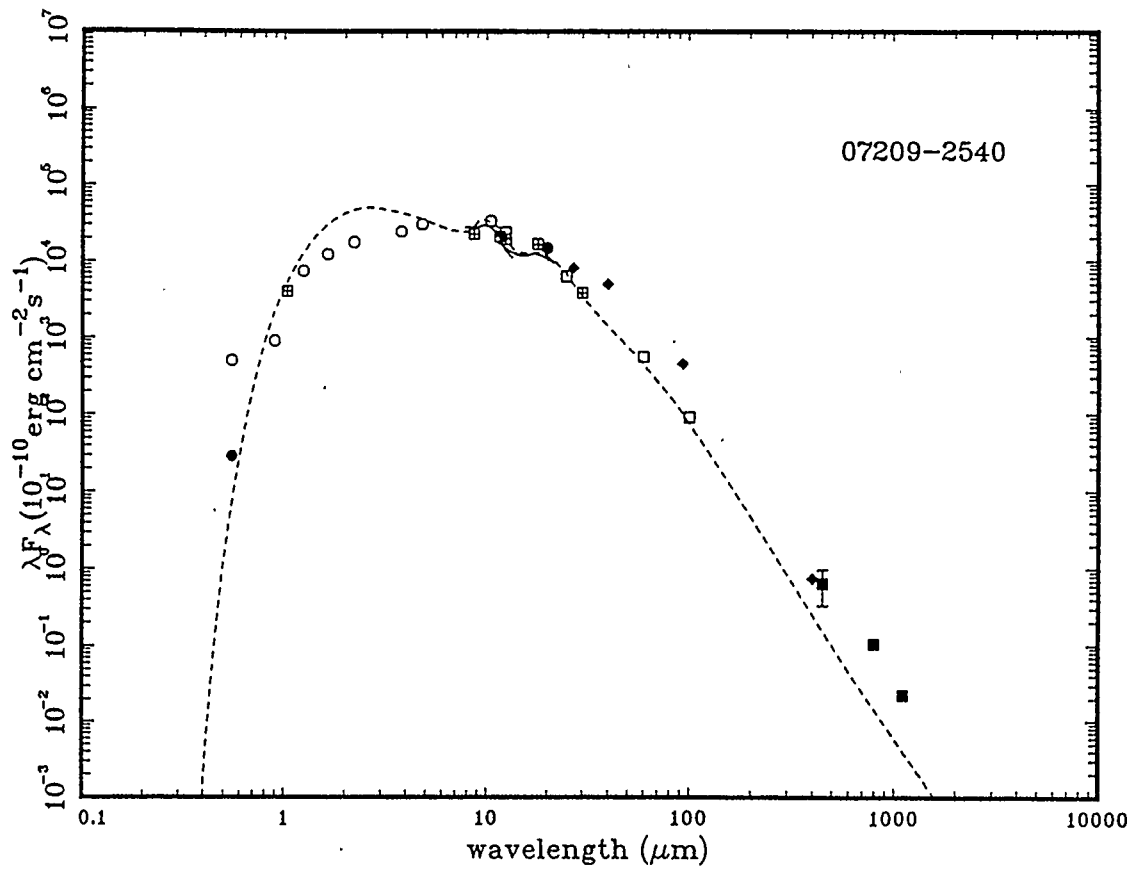


Figure 4.4: The model fit for VY Canis Majoris.

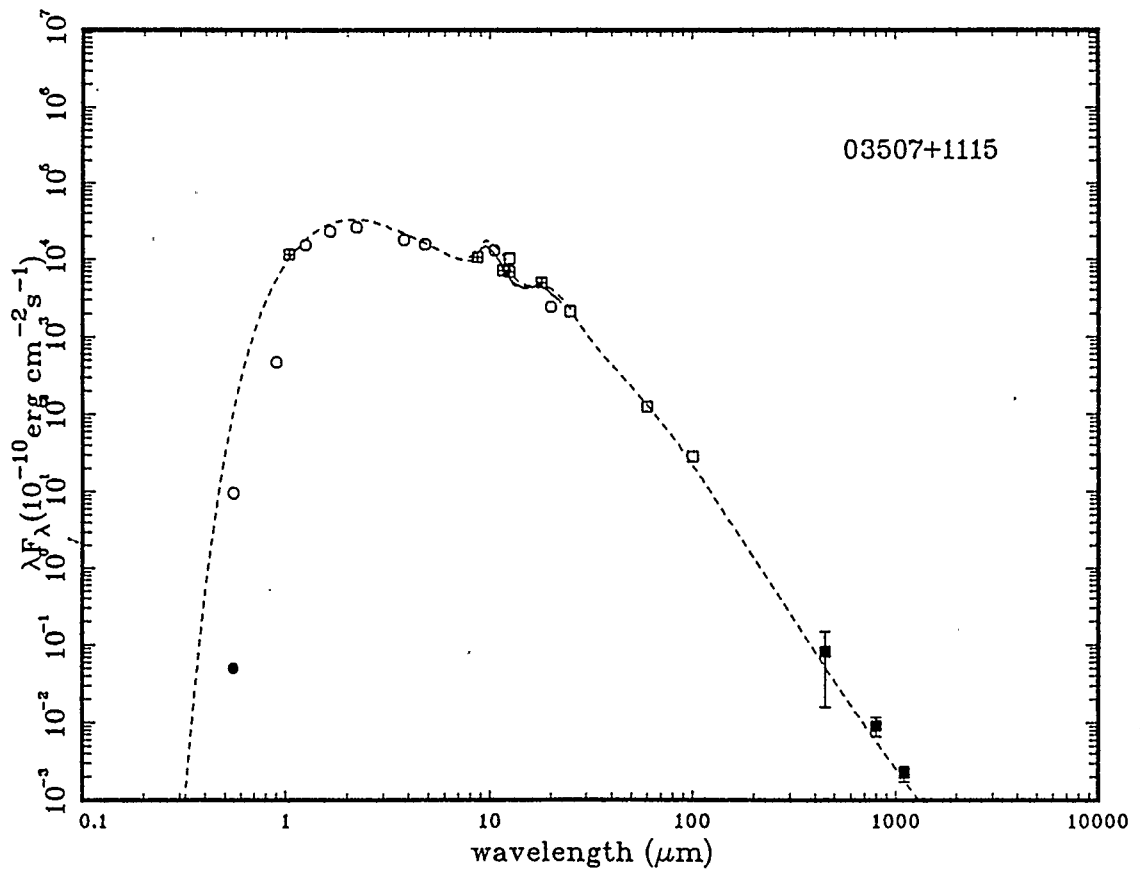


Figure 4.5: The model fit for IK Tauri.

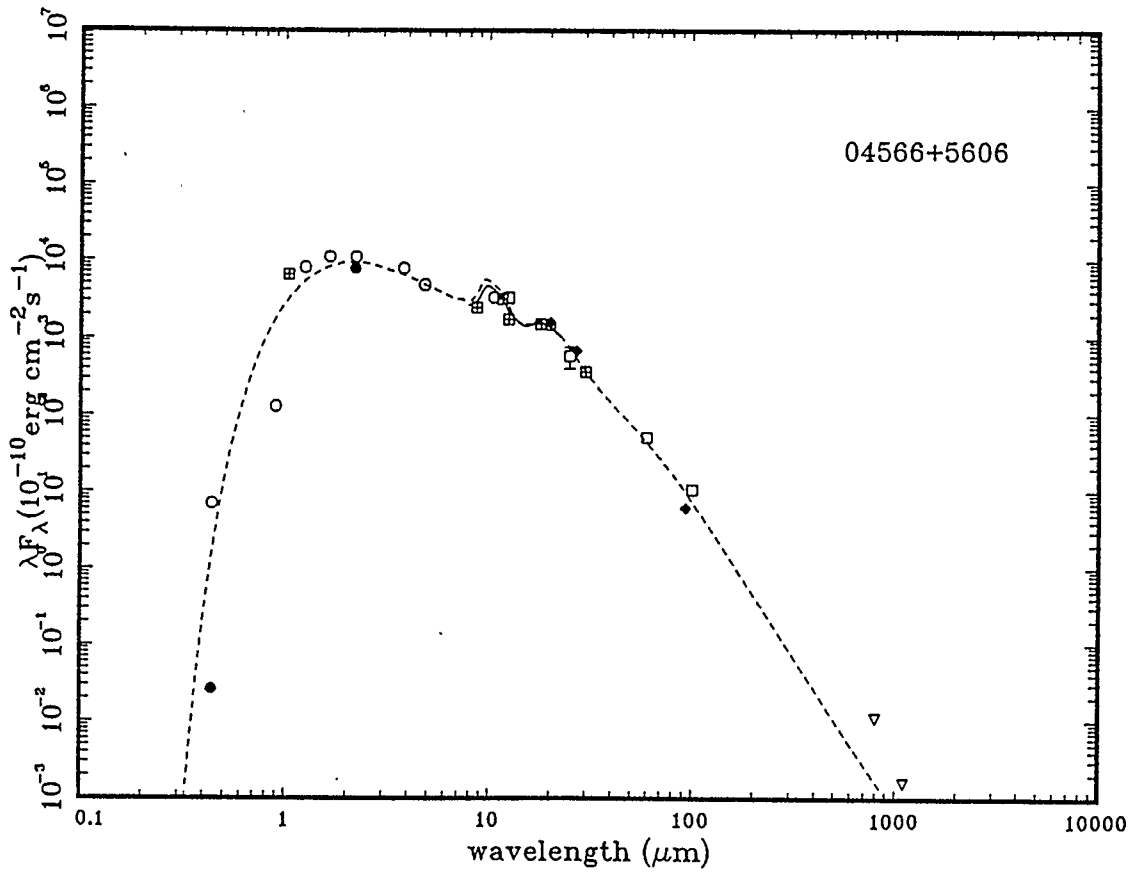


Figure 4.6: The model fit for TX Camelopardalis.

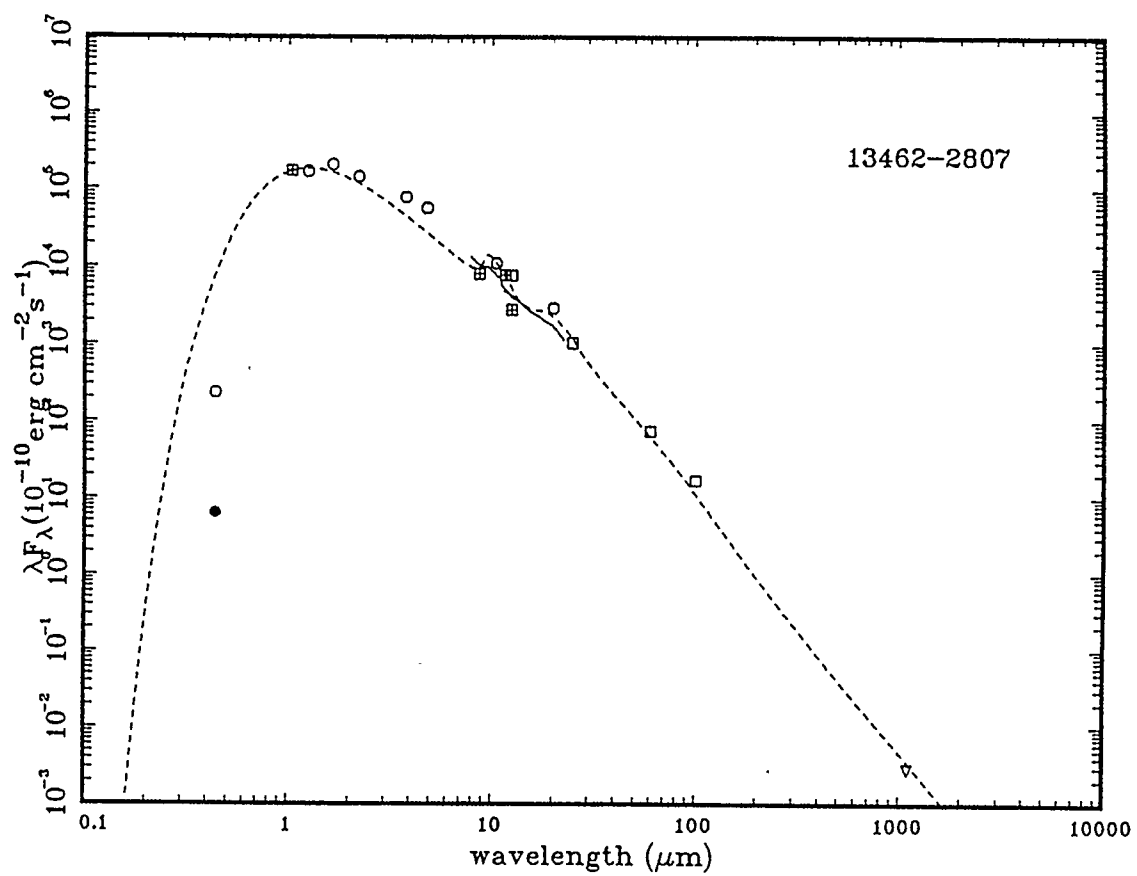


Figure 4.7: The model fit for W Hydrae.

Table 4.18: Model Results for the Carbon Stars.  
The final model fitting parameters for the carbon stars.

Name	CW Leo	RW LMi
$\tau_{11.3\mu m}$	3.0	0.1
$T_*$ ( $10^3 K$ )	2.3	2.5
$L_*$ ( $10^3 L_\odot$ )	50	8.5
$R_{in}$ ( $10^{14} cm$ )	2.71	0.89
$F_{tot}$ ( $10^{-10} erg s^{-1} cm^{-2}$ )	27.8	12.1
$D$ (kpc)	0.24	0.15
$\dot{M}$ ( $10^{-6} M_\odot yr^{-1}$ )	22.2	0.3

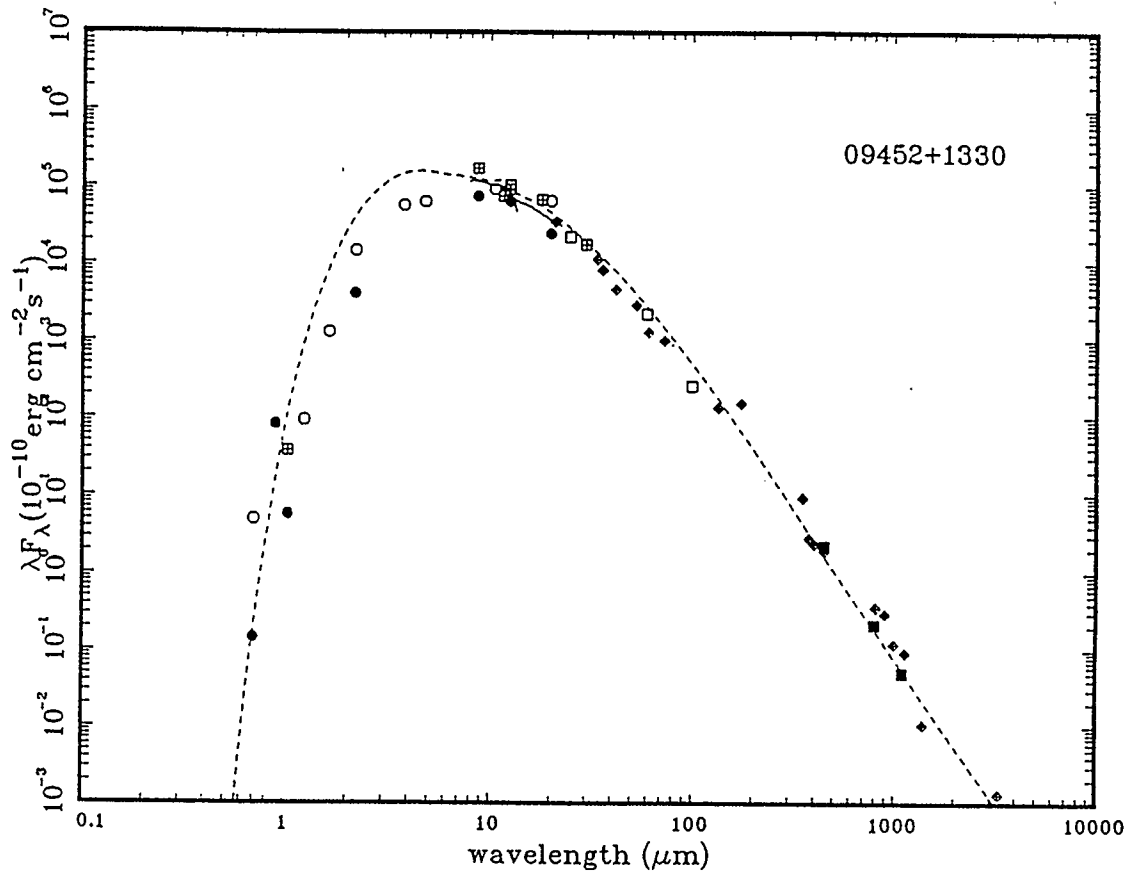


Figure 4.8: The model fit for CW Leonis.

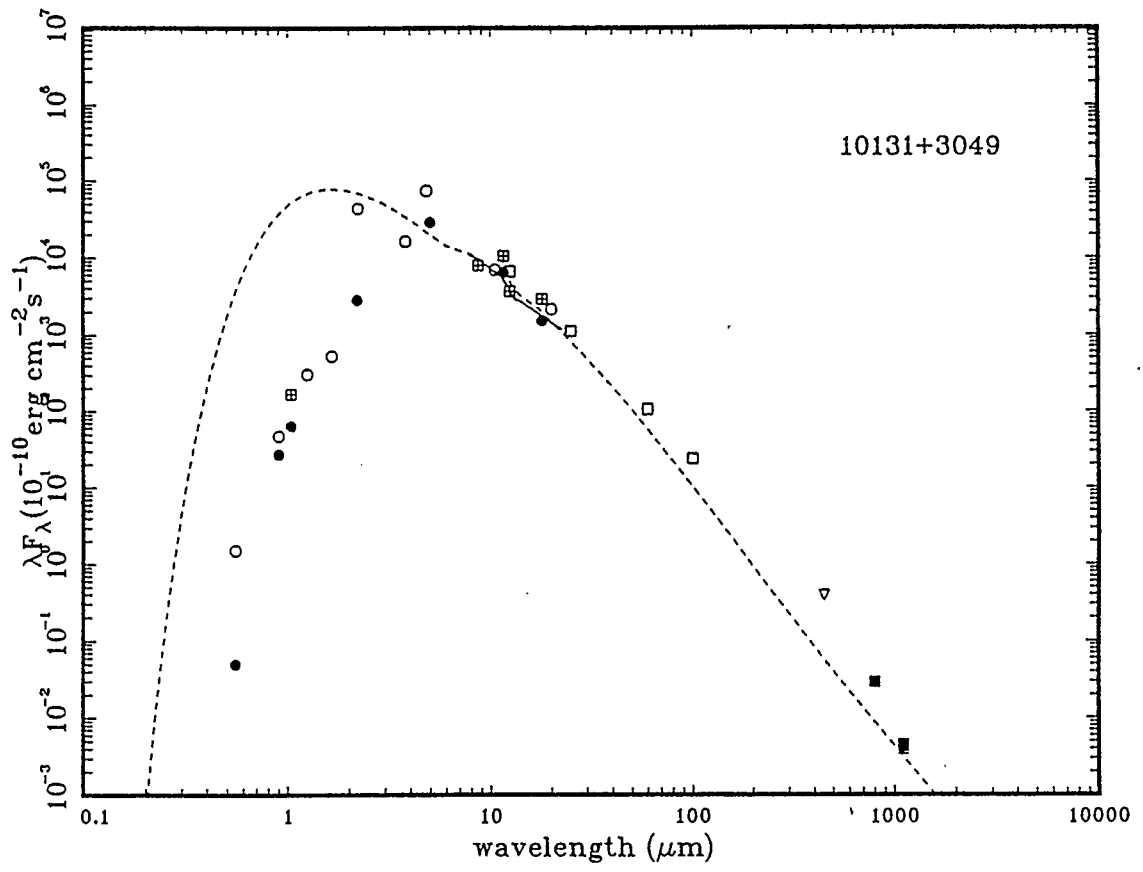


Figure 4.9: The model fit for RW Leonis Minoris.

## 4.5 Observational Spectra Plots of Other Objects

The graphical results for M82 and Hb 12 are presented in figures 4.10 and 4.11, respectively. Models were not generated to fit these objects since extensive modifications would have to be made to the modeling code to allow for more than one central heating source of the dust envelope. Since the JCMT observations only resulted in single upper limit values for each object, it was determined that no conclusive results about the opacity in the submillimetre region could be obtained from model fits to these objects.



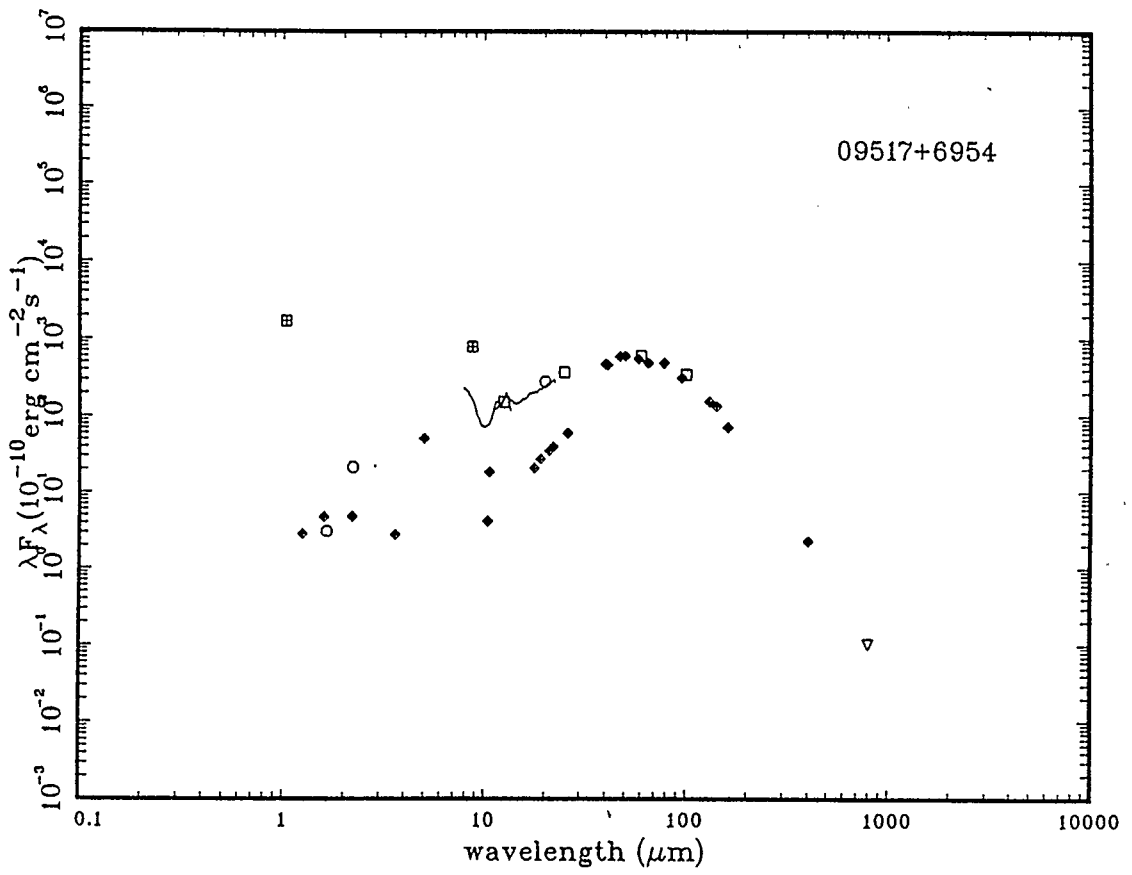


Figure 4.10: The plot of M82 observational data.

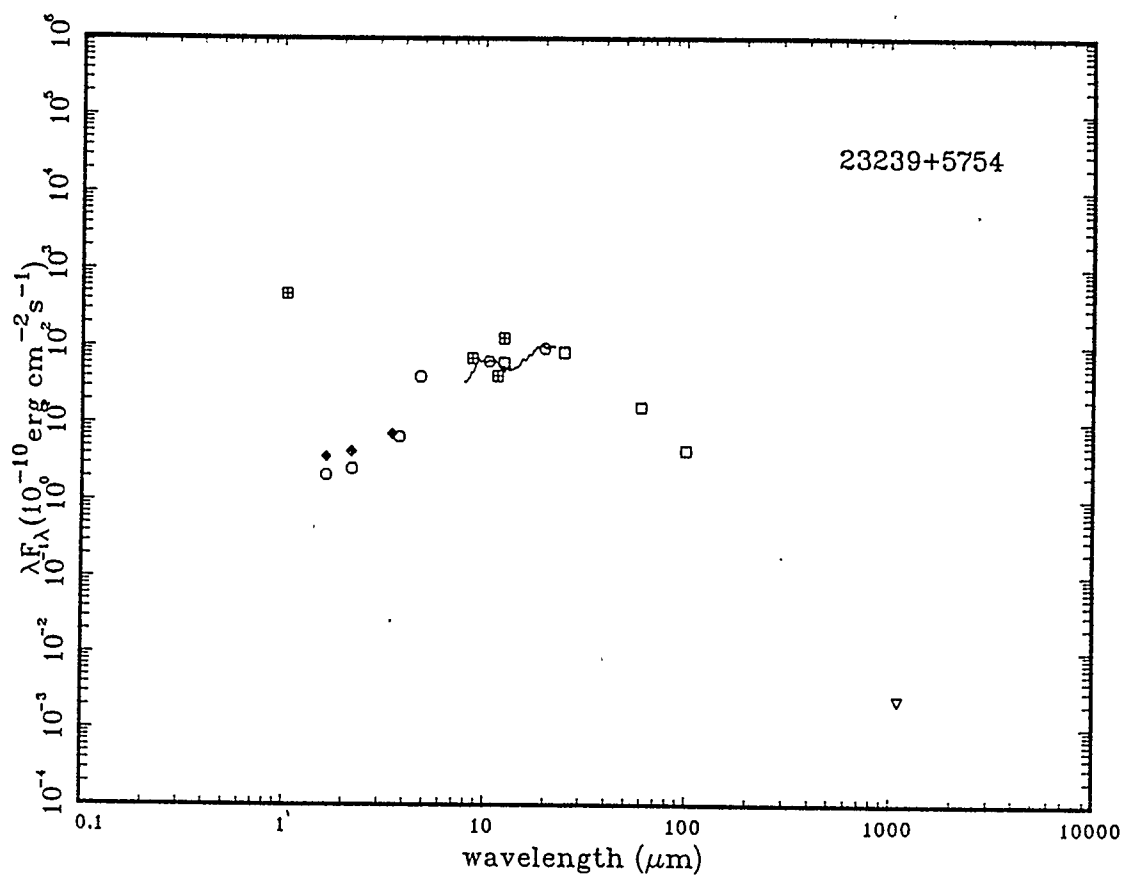


Figure 4.11: The plot of Hb 12 observational data.

## Chapter 5

### Discussion and Conclusions

The model results for the photosphere do not compare well for the most part with the data in the 0.1 to  $10\mu m$  range; this is especially true in the results for the carbon stars, CW Leo and RW LMi. A likely factor which may contribute to this is that the model does not take interstellar extinction into account. The interstellar medium is known to contain various types of dust. Interstellar extinction is considered one of the most important factors in the reduction of the apparent brightness of stars. The degree of extinction,  $A$ , is measured by the number of stellar magnitudes by which the star has been dimmed for each parsec along the line of sight (Kitchin, 1987), and is strongly wavelength dependent. The interstellar extinction has the form  $A_\lambda [\text{mag pc}^{-1}] = 0.0008\lambda^{-4}$  for wavelengths measured in microns (Kitchin, 1987). Radiation absorbed by the interstellar medium is generally re-radiated at infrared and microwave wavelengths. For CW Leo, whose distance was estimated at  $\sim 240\text{pc}$ , the extinction in the visual (V band) is  $A_V \simeq 0.42 \text{ mag}$ , while at  $\lambda = 100\mu m$  the extinction  $A_{100\mu m} \simeq 0.00041 \text{ mag}$ . Thus extinction is a factor to be considered at shorter wavelengths, while at longer wavelengths the extinction effects can be ignored. Thus the model results longward of approximately  $8\mu m$  are more accurate due to the negligible effects of interstellar extinction at longer wavelengths.

As can be seen in figure 5.1, the model spectrum is presented by the dashed line, while an input photospheric spectrum is presented by the dotted line. Where

the two lines separate in the longer wavelengths is indicative of the circumstellar envelope emission.

## 5.1 M-Type Stars

In the previous chapter, the results of the model spectra as plotted with the observed spectra were shown. The silicate dust opacity had a  $\lambda^{-1}$  dependence out to  $84\mu m$  and a  $\lambda^{-1.5}$  dependence thereafter. The results of the model fit to IK Tau showed a good fit to the data in the submillimetre range. This indicates that an opacity dependence of  $\lambda^{-1.5}$  is a good estimation of the actual opacity dependence in the submillimetre wavelength range for this particular object. The results of the model fit to VY CMa did not show a good fit in the submillimetre range, though the fit was fairly good in the  $10\mu m$  to  $100\mu m$  range. For VY CMa, the slope of the model spectrum was too steep in the submillimetre range, indicating the a value of  $\gamma < 1.5$  would give better results for this object; an opacity dependence closer to  $\lambda^{-1}$  would possibly give a better fit in the submillimetre range. The results of the model fit to TX Cam do not lend themselves to any conclusions about the opacity dependence in the submillimetre wavelength range since upper limit values only were obtained at  $800\mu m$  and  $1100\mu m$ . We can surmise that the opacity dependence of  $\lambda^{-1.5}$  where  $\gamma = 1.5$  gives a spectra which falls below the upper limits, so that  $\gamma = 1.5$  is not too low as a power dependence for opacity in this case. The results of the model fit to W Hya showed the model spectrum in the submillimetre range to lie just on the upper limit observed data value at  $1100\mu m$ ; no valid conclusion can be drawn from this other than to say that the opacity dependence for this

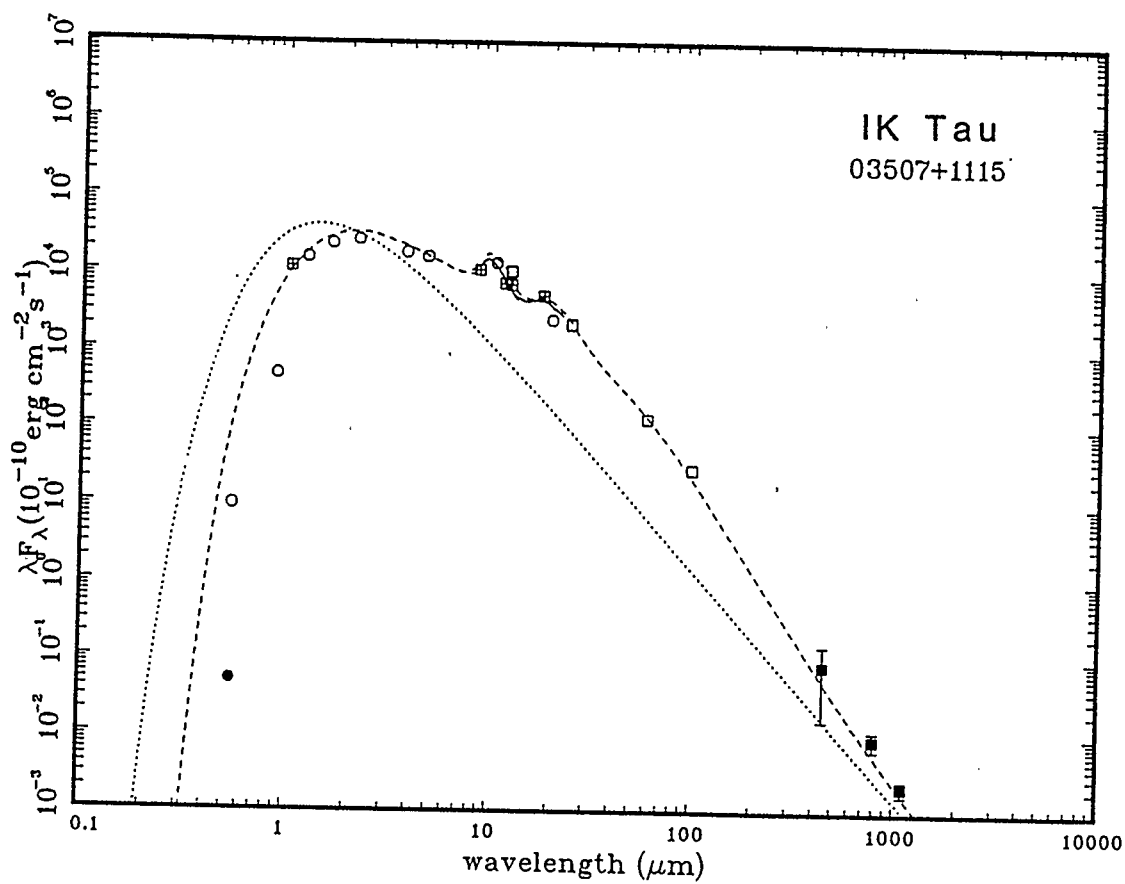


Figure 5.1: An example of the model spectrum (dashed line) as opposed to a photospheric spectrum (dotted line). The region where the model spectrum strays from the black body spectrum is indicative of the circumstellar envelope.

particular object is  $\lambda^{-1.5}$  or steeper. The model results fit to  $\alpha$  Ori gave no good fit, thus no valid conclusion may be drawn for this object.

From these collective results, the trend indicates that there is no particular single opacity wavelength dependence (for a single power index value) that will fit all of the oxygen-rich stars out in the submillimetre wavelength range.

## 5.2 Carbon Stars

The silicon carbide opacity taken from Chan (1988) had a  $\sim \lambda^{-1}$  longward of approximately  $12\mu m$ . From the model spectra results for CW Leo, this opacity function would seem appropriate for this particular star. The model spectrum fits the data for CW Leo quite well longward of approximately  $10\mu m$ . This indicates that an opacity dependence of  $\lambda^{-1}$  is appropriate for this object out in the submillimetre wavelength range. The results of the model fit to RW LMi were poor. The fit was somewhat too steep out in the submillimetre wavelength range, indicating that an opacity dependence of  $\lambda^{-\gamma}$  where  $\gamma < 1$  may be more appropriate for this star.

The model spectra for the carbon stars tend to be too broad: shortward of  $\sim 10\mu m$ , the fit to the data for RW LMi is not very good, though it is not too bad for CW Leo. Though interstellar extinction can account for a small part of this ill fit, it cannot account for the magnitude of the discrepancy between the model spectra and the data in the case of RW LMi. Many attempts were made to obtain a better fit to the data in this region ( $\lambda < 10\mu m$ ). One such attempt was to determine the effects of scattering versus no scattering; the scattering effects are

due to Rayleigh scattering of photons off atoms or molecules in which the scattering cross-section ( $Q_{sca}\pi a^2$ ) varies as  $\lambda^{-4}$ . As can be seen in figure 5.2, the effects of scattering on the model spectra are small enough to be considered negligible for our purposes, and as such cannot account for the discrepancy between the model spectra and the data.

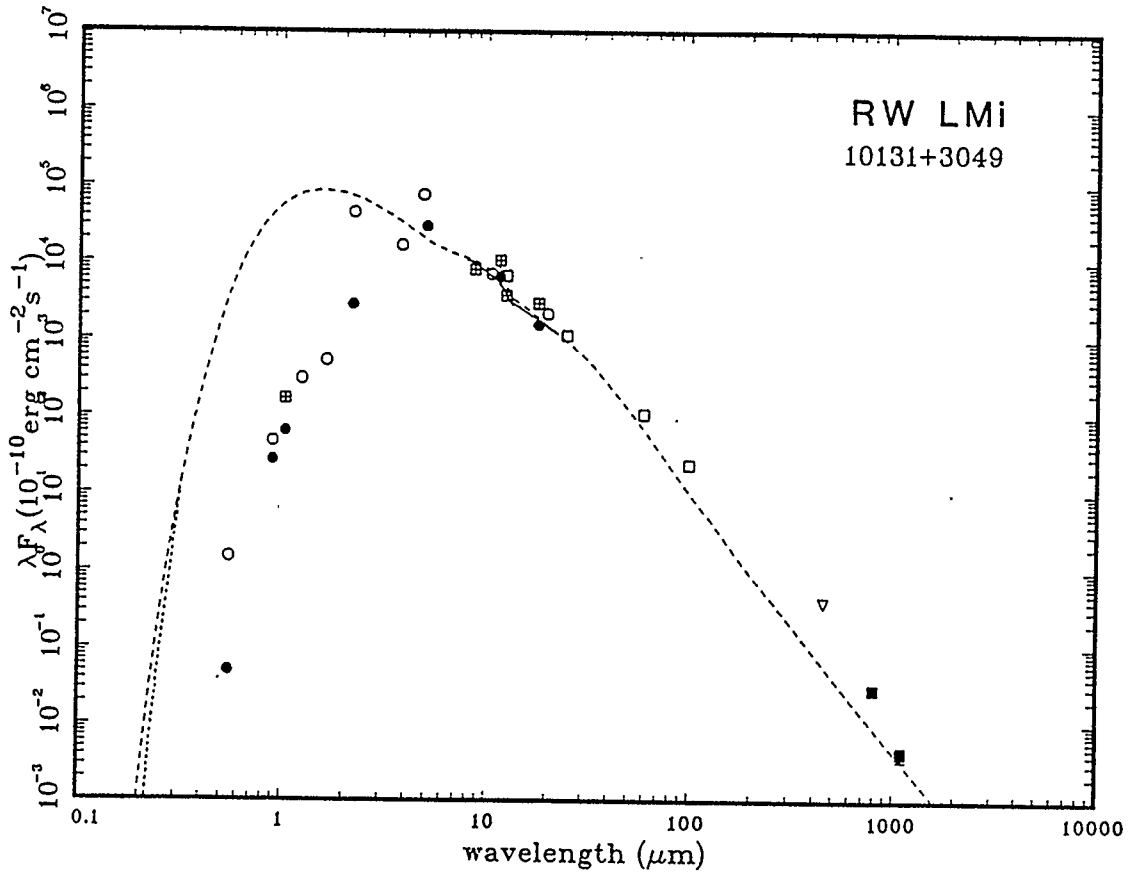


Figure 5.2: The Effects of Scattering versus No Scattering. The dashed line represents the model spectra with no scattering, while the dotted line represents the model spectra with isotropic scattering.



Other attempts to obtain better fits which were made were the lowering of the effective temperature  $T_*$  of the star, which shifts the peak of the spectrum down and to the right towards the longer wavelengths. Lowering the temperature of the star, even by  $800K$ , had little effect in altering the model spectra: the largest change was a shift to the right of  $\sim 0.08\mu m$ . Similar results occurred in lowering the effective luminosity  $L_*$ . When attempting to fit the shortward spectra by adjusting the optical depth  $\tau$ , care had to be taken to maintain the fit to the data longward of  $10\mu m$ , particularly the LRS data. The model spectral peak lowers and shifts to the right as  $\tau_{\lambda_0}$  is increased, but at the same time, the fit longward of  $\sim 10\mu m$  is also shifted to the right, thus no longer fitting the LRS data. As such, adjusting the optical depth had little effect on the spectra shortward of  $10\mu m$  if the fit to the LRS spectra was to be maintained. An example of this is shown in figure 5.3 in which the optical depth  $\tau_{11.3\mu m}$  was increased, and though the fit is somewhat better on the shortward side of  $10\mu m$ , the LRS data is no longer fitted well at all. If we were to seriously consider this particular model, we would have to surmise that silicon carbide dust may not be the primary constituent of the dust surrounding this star since the LRS signature does not conform to the SiC model signature. The conclusion about the fit shortward of  $10\mu m$  is that changes must be made to the opacity function of the dust in this region of the spectrum. Possibly changes in the dust composition may need to be made. This can be a suggestion for future work.

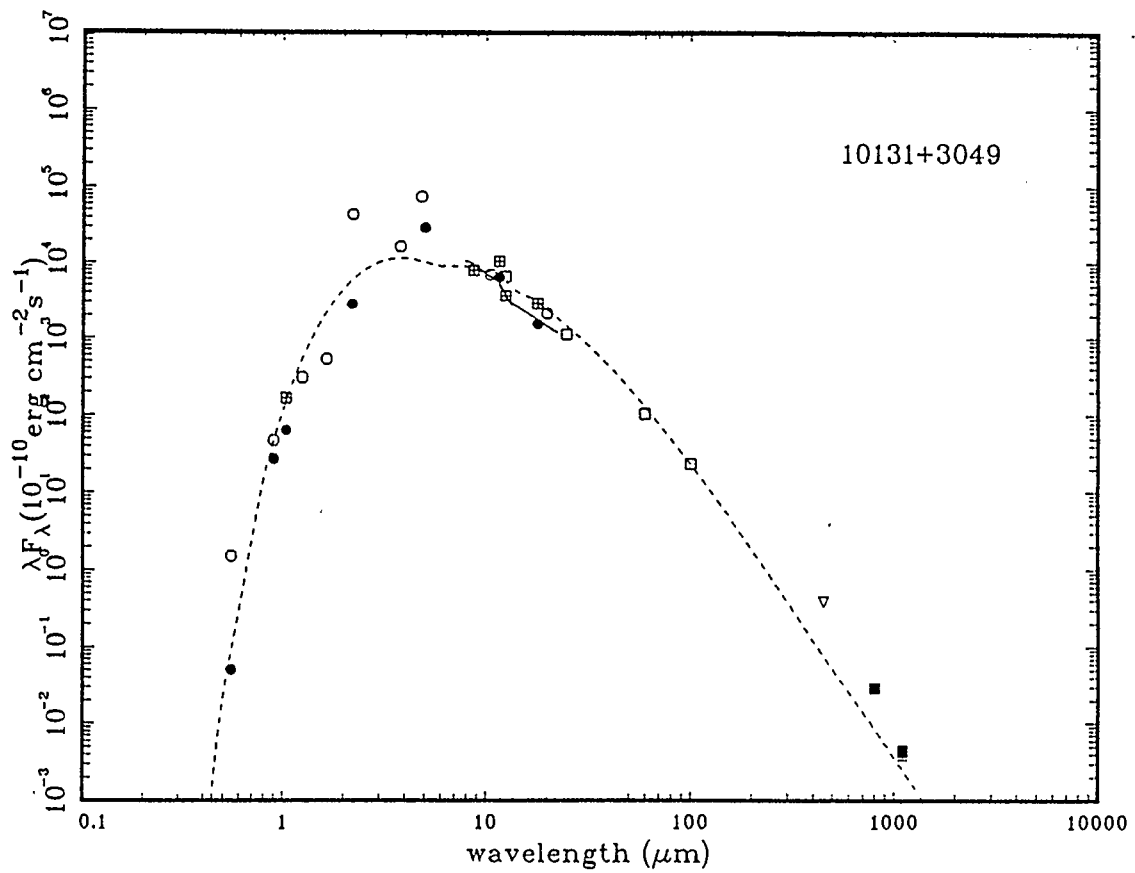


Figure 5.3: The Model Fit to RW LMi with a higher  $\tau$ . The final parameters for this model are  $\tau = 1.8$ ,  $T_* = 2700K$ ,  $R_{in} = 1.1 \times 10^{14}cm$ ,  $L_* = 8500L_\odot$ ,  $D = 0.37kpc$ , and  $\dot{M} = 6.7 \times 10^{-6}M_\odot yr^{-1}$ .

### 5.3 Suggestions for Future Work

Future work could consist of adjusting the present opacity functions for the dust types to better fit the stellar data. Better results could possibly be obtained by assuming more than one type of dust per star, if the spectra exhibits definite features of another dust type as well as that of the primary dust type.

In the cases of the objects M82 and Hb 12, expanding the DUSTCD code to allow for more than one central heating source would possibly be a good start to modeling M82. Modifying the DUSTCD code to model planetary nebulae could give us some more knowledge about the submillimetre spectrum of Hb 12. Of course, more observations of these two objects in the submillimetre wavelength range would need to be made before any good conclusions could be made about their respective emergent spectra.

#### 5.3.1 Modifications to the Opacity Functions

##### SiC Opacity Function

The model spectra tended to fit the *IRAS* data and the longer wavelength data fairly well, but did not seem to fit the data shortward of  $\sim 8\mu m$  very well. The opacity function in this wavelength region was assumed similar to that of silicate dust due to the difficulty of finding large enough samples of data (Chan, 1988). Preliminary data of LRS class 40 objects has since become available, and determining a better SiC opacity function could be carried out in the future to produce better model spectra to fit the available data.

### Silicate Opacity Function

The model spectra tended to fit the *IRAS* and submillimetre data fairly well in some cases and too steeply in others. Future work could consist of obtaining submillimetre data for more oxygen-rich giants in order to better define the opacity wavelength dependence longward of  $\sim 100\mu m$  and to look for trends which could give some sort of indication as to why the various objects had various opacity wavelength dependences.

## Bibliography

- Abell, G.O. *Exploration of the Universe, 4th Ed.*, (New York: Saunders CBS College Publishing) (1982)
- Abolins, J.A., Adams, D.J., Jameson, R.F., Hough, J.H., Axon, D.J. *Mon. Not. R. astr. Soc.* **186**, 23 (1979) [790306]
- Ade, P.A.R., Rowan-Robinson, M., Clegg, P.E. *Astron. Astrophys.* **53**, 403 (1976) [761201]
- Aitken, D.K. in C.G. Wynn-Williams and D.P. Cruikshank (Eds.), *Infrared Astronomy*, pp.207-221, *IAU No. 96* (Dordrecht: D. Reidel Publishing) (1981)
- Aitken, D.K., Roche, P.F., Spencer, P.M., Jones, B. *Astrophys. J.* **233**, 925 (1979)
- Allen, D.A. *Mon. Not. R. astr. Soc.* **168**, 1 (1974) [740708]
- Allen, D.A. *Infrared: The New Astronomy*, (New York: John Wiley and Sons) (1975)
- Becklin, E.E., Frogel, J.A., Hyland, A.R., Kristian, J., Neugebauer, G. *Astrophys. J. (Letters)* **158**, L133 (1969) [691201]
- Bedijn, P.J. *Astron. Astrophys.* **186**, 136 (1987)
- Beichman, C.A., Dyck, H.M., Simon, T. *Astron. Astrophys.* **62**, 261 (1978) [780101]
- Bensammar, S., Friedjung, M., Letourneur, N., Perrier, F. *Astron. Astrophys.* **149**, L1 (1985) [850808]
- Bevington, P.R., *Data Reduction and Error Analysis for the Physical Sciences*, (New York: McGraw-Hill Books) (1969)
- Bignell, R.C. in D.R. Flower (Ed.) *Planetary Nebulae*, IAU Symposium No. 103, pp.69-78, (Dordrecht:D. Reidel Publishing) (1983)
- Bland, J. and Tully, R.B. *Nature* **334**, 43 (1988)
- Borghesi, A., Bussoletti, E., Colangeli, L., De Blasi, C. *Astron. Astrophys.* **153**, 1 (1985)
- Bowers, P.F., Knapp, G.R. in S. Kwok and S.R. Pottasch (Eds.) *Late Stages of Stellar Evolution*, pp.143-144, (Dordrecht: D.Reidel Publishing) (1987)

- Bright Star Catalogue*(4th edition), by D.Hoffleit and C.Jaschek (Connecticut: Yale University Observatory) (1982)
- Bujarrabal, V., Planesas, P., del Romero, A. *Astron. Astrophys.* **175**, 164 (1987)
- Campbell, M.F., Elias, J.H., Gezari, D.Y., Harvey, P.M., Hoffman, W.F., Hudson, H.S., Neugebauer, G., Soifer, B.T., Werner, M.W., Westbrook, W.E. *Astrophys. J.* **208**, 396 (1976) [760609]
- Chan, S.J. University of Calgary Master's thesis (1988)
- Chan, S.J. and Kwok, S., *Publication of the Rothney Astrophys. Observatory* (Ap. J. in press) (1988)
- Chandrasekhar, S. *Radiative Transfer*, (New York: Dover Publications) (1960)
- Clegg, P.E., Rowan-Robinson, M., Ade, P.A.R. *Astron. J.* **81**, 339 (1976) [760601]
- Cohen, M. *Mon. Not. R. astr. Soc.* **186**, 837 (1979)
- Cohen, M. *Mon. Not. R. astr. Soc.* **206**,137 (1984) [840106]
- Cohen, M. and Barlow, M.J. *Astrophys. J.* **193**, 401 (1974) [741009]
- Cohen, M., Harvey, P.M., Schwartz, R.D. *Astrophys. J.* **296**, 663 (1985) [850913]
- Cox, G.G. and Parker, E.A. *Mon. Not. R. astr. Soc.* **186**, 197 (1979) [790101]
- De Jager, C. *The Brightest Stars* (Geophysics and Astrophysics, Monographs, Volume 19), (Dordrecht: D.Reidel Publishing Company) (1980)
- Dickinson, D.F. *Astrophys. J. Suppl.* **30**, 259 (1976) [760302]
- Draine, B.T. *Astrophys. J. Suppl.* **57**,587 (1985)
- Draine, B.T. and Lee, H.M. *Astrophys. J.* **285**, 89 (1984)
- Drake, S.A., Linsky, J.L, Elitzur, M. *Astron. J.* **94**, 1280 (1987)
- Dyck, H.M., Zuckerman, B., Leinert, Ch., Beckwith, S. *Astrophys. J.* **287**, 801 (1984) [841213]
- Elias, J.H., Ennis, D.J., Gezardi, D.Y., Houser, M.G., Houck, J.R., Lo, K.Y., Matthews, K., Nadeau, D., Neugebauer, G., Werner, M., Westbrook, W.E. *Astrophys. J.* **220** , 25 (1978) [780210]

- Fay Jr., T.D. *Astrophys. J.* **188**, 553 (1974)
- Fazio, G.G., McBreen, B., Stier, M.T., Wright, E.L. *Astrophys J. (Letters)* **237**, L39 (1980)
- Feast, M.W. and Whitelock, P.A. in S. Kwok and S.R. Pottasch (Eds.) *Late Stages of Stellar Evolution*, pp.33-46, (Dordrecht: D.Reidel Publishing) (1987)
- Gehrz, R.D. *Astrophys. J.* **178**, 715 (1972) [721203]
- Gerhz, R.D. and Woolf, N.J. *Astrophys. J.* **165**, 285 (1971) [710403]
- General Catalogue of Variable Stars*(4th edition), editor P.N. Kholopov (Moscow: NAUKA Publishing House) (1985)
- Gezari, D.Y., Schmitz, M., Mead, J.M., *Catalog of Infrared Observations, Part I - Data, Part II - Appendices*, 2nd ed., Nasa Reference Publication 1196 (December 1987)
- Gillet, F.C., Kleinmann, D.E., Wright, E.L., Capps, R.W. *Astrophys. J. (Letters)* **198**, L65 (1975)
- Gilman, R. *Astrophys. J. (Letters)* **155**, L185 (1969)
- Gilman, R.C. *Astrophys. J. Suppl. Ser.* **28**, 397 (1974)
- Grasdalen, G.L., Gehrz, R.D., Hackwell, J.A., Castelaz, M., Gullixson, C. *Astrophys. J. Suppl.* **53**, 413 (1983) [831007]
- Habing, H.J. in R.D. Wolstencroft and W.B. Burton (Eds.) *Millimetre and Submillimetre Astronomy* (Astrophysics and Space Science Library [ASSL] Volume 147), pp.207-222, (Edinburgh: Kluwer Academic Publishers) (1988)
- Hackwell, J.A. *Astron. Astrophys.* **21**, 239 (1972) [721103]
- Hagen, W. *P.A.S.P.* **94**, 835 (1982) [821005]
- Herman, J. *Astron. Astrophys. Suppl. Ser.* **74**, 133 (1988)
- Hirschfeld, A. and Simon, R.W. (Eds.) *Sky Catalogue 2000.0 Volume 2*, Cambridge University Press and Sky Publishing Corporation (1985)
- IRAS Explanatory Supplement**, Beichman, C.A., Neugebauer, G., Habing, H.J., Clegg, P.E., Chester, T.J. (Eds.), (Washington D.C.: US Government Printing Office) (1985)

- Jaffe, D.T., Becklin, E.E., Hildebrand, R.H. *Astrophys. J. (Letters)* **285**, L31 (1984) [841016]
- Jura, M. in R.D. Wolstencroft and W.B. Burton (eds.) *Millimetre and Submillimetre Astronomy*, pp.189-206 (Dordrecht: Kluwer Academic Publishers) (1988)
- Keady, J.J., Hall, D.N.B., Ridgway, S.T. *Astrophys. J.* **326**, 832 (1988)
- Kitchin, C.R. *Stars, Nebulae and the Interstellar Medium*, (Bristol: IOP Publishing Ltd.) (1987)
- Kwok, S. *Physics Reports* **156**, 111 (1987)
- Kwok, S., Invited Review for the 2nd Torino Workshop *Mass Outflows from Stars at Galactic Nuclei* to be published by Reidel, L. Bianchi and R. Gilmozzi (Eds.) (1988)
- Kwok, S. and Pottasch, S.R. (eds.) *Late Stages of Stellar Evolution* (Astrophysics and Space Science Library [ASSL] Volume 132), (Dordrecht: D.Reidel Publishing) (1987)
- Kwok, S. and Volk, M., preprint to be published in *From Comets to Cosmology*, A. Lawrence (Ed.), Springer Verlag (1988)
- Kwok, S., Volk, K., Chan, S.J. preprint to appear in *Evolution of Peculiar Red Giant Stars* (1988)
- Leahy, D.A., Kwok, S., Arquilla, R.A. *Astrophys. J.* **320**, 825 (1987)
- Lee, T.J., Beattie, D.H., Geballe, T.R., Pickup, D.A. *Astron. Astrophys.* **127**, 417 (1983) [831123]
- Leung, C.M. *Astrophys. J.* **199**, 340 (I) (1975)
- Leung, C.M. *Astrophys. J.* **209**, 75 (II) (1976a)
- Leung, C.M. *J. Quant. Spectrosc. Radiat. Transfer* **16**, 559 (1976b)
- Lockwood, G.W. *Astrophys. J. (Letters)* **160**, L47 (1970) [700402]
- Lockwood, G.W. *Astrophys. J.* **180**, 845 (1973) [730304]
- Lockwood, G.W. *Astrophys. J.* **192**, 113 (1974) [740806]
- Lockwood, G.W. *Astrophys. J. Suppl.* **58**, 167 (1985) [850511]



- Low, F.J. *Sky Survey AFCRL - 70 - 0179* (1970) [700302]
- Low, F.J., Reike, G.H., Armstrong, K.R. *Astrophys. J. (Letters)* **183**, L105 (1973) [730805]
- Mamon, G.A., Glassgold, A.E., Omont, A. *Astrophys. J.* **323**, 306 (1987)
- Matthews, H.E., in JCMT publication *The James Clerk Maxwell Telescope: A Guide for the Prospective User*, Royal Observatory Edinburgh, (July, 1988)
- McCabe, E.M. *Mon. Not. R. astr. Soc.* **200**, 71 (1982)
- McCarthy, D.W., Howell, R., Low, F.J. *Astrophys. J. (Letters)* **235**, L27 (1980) [800103]
- McCarthy, D.W., Low, F.J., Howell, R. *Astrophys. J. (Letters)* **214**, L85 (1977) [770608]
- Millar, T.J., Eilddér, J., Hjalmarson, Å., Olofsson, H. *Astron. Astrophys.* **182**, 143 (1987)
- Miller, J.S. *Astrophys. J. (Letters)* **161**, L95 (1970) [700803]
- Moroz, V.I. and Dibai, E.A. *Sov. Astr.* **12**, 184 (1968) [680902]
- Natta, A., Beckwith, S., Evans II, N.J., Beck, S.C., Moorwood, A.F.M., Oliva, E. *Astron. Astrophys.* **158**, 143 (1986) [860422]
- Netzer, N. and Knapp, G.R. *Astrophys. J.* **323**, 734 (1987)
- Neugebauer, G., Leighton, R.B. *NASA SP-3047* (1969) [690001]
- Ney, E.P. and Merrill, K.M. *AFGL-TR-80-0050* (1980) [800213]
- Ney, E.P., Strecker, D.W., Gehrz, R.D. *Astrophys. J.* **180**, 809 (1973) [730303]
- Novotny, E. *Introduction to Stellar Atmospheres and Interiors*, (New York:Oxford University Press) (1973)
- Orofino, V., Colangeli, L., Bussoletti, E., Strafella, F. *Ap. Sp. Sci.* **138**, 127 (1987)
- Pégourié, B. *Ap. Sp. Sci.* **136**, 133 (1987)
- Persson, S.E. and Frogel, J.A. *Astrophys. J.* **182**, 503 (1973) [730606]

- Phillips, J.P., White, G.J., Ade, P.A.R., Cunningham, C.T., Richardson, K.J., Robson, E.I., Watt, G.D. *Astron. Astrophys.* **116**, 130 (1982) [821215]
- Price, S.D., Murdock, T.L. AFGL-TR-83-0161 (1983) [830610]
- Price, S.D., Murdock, T.L., Shirandan, K. AFGL-TR-83-0055 (1983) [830201]
- Rengarajan, T.N., Fazio, G.G., Maxson, C.W., McBreen, B., Serio, S., Sciortino, S. *Astrophys. J.* **289**, 630 (1985) [850209]
- Rickard, L.J. and Harvey, P.M. *Astron. J.* **89**, 1520 (1984) [841001]
- Ridgway, S.T. and Keady, J.J. *Astrophys. J.* **326**, 843 (1988)
- Rieke, G.H., Lebofsky, M.J., Thompson, R.I., Low, F.J., Tokunaga, A.T. *Astrophys. J.* **238**, 24 (1980) [800504]
- Rieke, G.H. and Low, F.J. *Astrophys. J. (Letters)* **176**, L95 (1972) [720901]
- Rieke, G.H. and Low, F.J. *Astrophys. J. (Letters)* **199**, L13 (1975) [750701]
- Rowan-Robinson, M. and Harris, S. *Mon. Not. R. astr. Soc.* **200**, 197 (II) (1982)
- Rowan-Robinson, M. and Harris, S. *Mon. Not. R. astr. Soc.* **202**, 767 (III) (1983a)
- Rowan-Robinson, M. and Harris, S. *Mon. Not. R. astr. Soc.* **202**, 797 (IV) (1983b)
- Rowan-Robinson, M., Lock, T.D., Walker, S.W., Harris, S. *Mon. Not. R. astr. Soc.* **222**, 273 (1986)
- Rybicki, G.B. and Lightman, A.P. *Radiative Processes in Astrophysics*, (new York: John Wiley and Sons) (1979)
- Sahai, R., Claussen, M.J., Masson, C.R. *Astron. Astrophys.* (preprint) (1988)
- Schmitz, M., Mead, J.M., Gezari, D.Y., *Infrared Source Cross-Index*, 1st ed. , Nasa Reference Publication 1182 (April 1987)
- Simon, M., Simon, T., Joyce, R.R. *Astrophys. J.* **227**, 64 (1979)
- Simon, T. *Astron. J.* **81**, 764 (1976) [760901]
- Simon, T., Morrison, D., Cruikshank, D.P. *Astrophys. J. (Letters)* **177**, L17 (1972) [721002]

- Shu, F.H. *The Physics of the Universe: An Introduction to Astronomy* (Mill Valley, California: University Science Books) (1982)
- Skinner, C.J. and Whitmore, B. *Mon. Not. R. astr. Soc.* **224**, 335 (1987)
- Spagna Jr., G.F. and Leung, C.M. *Comp. Phys. Comm.* **28**, 337 (1983)
- Spitzer Jr., L. *Physical Processes in the Interstellar Medium*, (New York: John Wiley and Sons) (1978)
- Stencel, R.E., Pesce, J.E., Bauer, W.H., *Astron. J.* **95**, 141 (1988)
- Strohmeier, W. *Variable Stars*, (New York: Pergamon Press) (1972)
- Szymczak, M., *Ap. Sp. Sci.* **139**, 63 (1987)
- Telesco, C.M. and Harper, D.A. *Astrophys. J.* **235**, 392 (1980) [800108]
- Thomas, J.A., Hyland, A.R., Robinson, G. *Mon. Not. R. astr. Soc.* **165**, 201 (1973) [730002]
- Treffers, R. and Cohen, M. *Astrophys. J.* **188**, 545 (1974)
- Van de Hulst, H.C. *Light Scattering by Small Particles* (New York: John Wiley and Sons) (1957)
- Volk, K.M. University of Calgary **Ph. D. thesis** (1986)
- Volk, K. and Kwok, S. *Astrophys. J.* **315**, 654 (1987)
- Volk, K. and Kwok, S. *Astrophys. J.* **331**, 435 (1988)
- Wannier, P.G. and Sahai, R. *Astrophys. J.* **319**, 367 (1987)
- Wehrse, R. in I. Appenzeller and C. Jordan (Eds.) *IAU Symposium No. 122 Circumstellar Matter*, pp.255-266, D. Reidel Publishing Company (1987)
- Werner, M.W. in M. Morris and B. Zuckerman (Eds.), *Mass Loss from Red Giants*, pp.117-128, (New York: D. Reidel Publishing Company) (1985)
- White, N.M. *Astrophys. J.* **242**, 646 (1980) [801206]
- White, N.M. and Wing, R.F. *Astrophys. J.* **222**, 209 (1978) [780508]
- Wickramasinghe, N.C. *Light Scattering Functions for Small Particles*, (New York: John Wiley and Sons) (1973)

- Williams, P.M., Beattie, D.H., Stewart, J.M. *Oservatory* **96**, 184 (1976) [761006]
- Wisniewski, W.Z., Wing, R.F., Spinrad, H., Johnson, H.L., *Astrophys. J. (Letters)* **148**, L29 (1967) [670402]
- Wolstencroft, R.D. and Burton, W.B. (Eds.) *Millimetre and Submillimetre Astronomy* (Astrophysics and Space Science Library [ASSL], Volume 147), appendix, (Dordrecht: Kluwer Academic Publishers) (1988)
- Woolf, N.J. in G.B. Field and A.G.W. Cameron (Eds.) *The Dusty Universe*, pp.59-88, (New York: Neale Watson Academic Publications) (1973)
- Wylie Jr., C.R. *Advanced Engineering Mathematics, 2nd Ed.* (New York: McGraw Hill Books) (1960)
- Zuckerman, B. *Ann. Rev. Astron. Astrophys.* **18**, 263 (1980)
- Zuckerman, B. and Dyck, H.M. *Astrophys. J.* **311**, 345 (1986)